An Investigation of High-Order Polygonal Wheel Wear in High-speed Rail Vehicles

Xingwen Wu

A Thesis

in

The Department

of

Mechanical, Industrial and Aerospace Engineering

Presented in Partial Fulfillment of the Requirements

For the Degree of

Doctor of Philosophy (Mechanical Engineering) at

Concordia University

Montreal, Quebec, Canada

February 2018

© Xingwen WU, 2018

CONCORDIA UNIVERSITY
SCHOOL OF GRADUATE STUDIES

This is to certify that the thesis prepared

By: **Xingwen Wu**

Entitled: **An Investigation of High-Order Polygonal Wheel Wear in High-speed**

                Rail Vehicles

and submitted in partial fulfillment of the requirements for the degree of

       Doctor Of Philosophy   (Mechanical Engineering)

complies with the regulations of the University and meets the accepted standards with respect to originality and quality.

Signed by the final examining committee:

                                       Chair
Dr. Alex De Visscher

                                       External Examiner
Dr. Dan Zhang

                                       External to Program
Dr. Ashutosh Bagchi

                                       Examiner
Dr. Ashok Kaushal

                                       Examiner
Dr. Javad Dargahi

                                       Thesis Supervisor (s)
Dr. Subhash Rakheja

Dr. A.K.W. Ahmed

Approved by _____
         Dr. Ali Dolatabadi   Chair of Department or Graduate Program Director

 March 9, 2018
Date of Defense

                         _____
       Dr. Amir Asif   Dean, Faculty of Engineering and Computer Science

ABSTRACT

An Investigation of High-Order Polygonal Wheel Wear in High-speed Rail Vehicles

Xingwen WU, Ph.D.
Concordia University, 2018

The wheel polygonalization, regarded as a periodic radial defect on the wheel circumference, has been observed in high-speed rail vehicles during the recent year. Such periodic defects of the wheel tread, especially the high-order wheel polygonalization, cause high magnitude and high-frequency variation in the wheel/rail contact forces, considerable axle box vibration, and stresses in the vehicle and track components, and thus in-service fatigue failures. The mechanism leading to high-order polygonal wear of the wheels, however, is not yet fully understood, although its adverse effects on dynamic responses of the vehicle have been reported in a few studies. This dissertation research focuses on the mechanisms leading to evolution of wheel tread polygonalization and its effects on dynamic responses of the coupled vehicle/track system.

A coupled vehicle/track dynamic model was initially developed to investigate the influences of discrete wheel defects as well as wheel polygonalization. Owing to the high-frequency nature of the wheel-rail impact force, the wheelset and slab track were modeled as flexible bodies, which were integrated into the vehicle model using the modal superposition method. The multi-body dynamic model was formulated for a typical high-speed train rail car while the track was modeled considering the rail as a Timoshenko beam discretely supported on a flexible track slab. The validity of the proposed coupled model was demonstrated by comparing the simulation model results with those available from the reported studies and acquired from a long-term field test program. The results obtained under excitations arising from a wheel flat or a polygonal wheel revealed substantial effects of wheelset flexibility on the peak wheel/rail creepage, axle box acceleration and stress in the wheelset axle shaft. The high order polygonal wheel wear also resulted in substantially higher frequency variations in the wheel-rail contact forces, which could excite vibration modes of the wheelset and the axle box.

A long-term field test campaign, involving measurements of changes in the wheel surface irregularities and the axle box acceleration responses, was undertaken on a high-speed rail vehicle to characterize wheel polygonalization and its growth rate. The wheel re-profiling process was found to be the main casual factor of initial wheel irregularities, which could be characterized by the third harmonic order. The measured data revealed that initial wear can rapidly propagate into

polygonal wear of order 18, likely due to high-frequency wheel-rail impact loads. The results also revealed strong positive correlation between the axle box acceleration and roughness level of the wheel polygonalization. The simulation results showed that high-frequency wheel-rail impacts excite bending deformation modes of the wheelset axle shaft and the track at speeds exceeding 210 *km/h*.

A long-term wear iteration scheme integrating the coupled vehicle/track dynamic model and an Archard wear model, was subsequently formulated to identify main contributors of formation of wheel polygonalization. The simulation results were analyzed to establish a better understanding of evolution of wheel polygonalization over a relatively long period. The three half wavelength rail bending vibration mode within the wheelbase length (near 650 *Hz*) was identified as the primary contributor to high magnitude wheel/rail contact forces in the 500 ~ 700 *Hz* frequency range, and the high order wheel polygonalization. The wheelset flexibility was judged as the likely contributor to the lower order wheel polygonalization. Increasing rail pad support stiffness intensified the wheel/rail coupled vibration leading to lower order wheel polygonalization. The results further showed that a higher rail pad damping could suppress the formation of high order wheel polygonalization. In addition, eliminating the initial wheel irregularities and frequent variations in the operating speed could mitigate the formation of wheel polygonalization.

ACKNOWLEDGEMENTS

CONTRIBUTION OF AUTHORS

This thesis involves the analytical and experimental investigations on the high-order wheel polygonalization in China's high-speed rail vehicles. The thesis research involved a long-term field study of a high-speed train operating in China and thorough studies of the defects encountered in wheels of the high-speed trains. The thesis research was conducted through extensive collaborations from researchers as well as industrial partners in China, which facilitated the long-term field test program and provided essential designs and data for formulated the vehicle as well as long-term wear models. The resulting research publications acknowledged the contributions of the collaborators through co-authorship. All aspects of the dissertation research, however, were under direct supervisions of Prof. Subhash Rakheja and Prof. A.K.Waizuddin Ahmed.

TABLE OF CONTENTS

LIST OF FIGURES

LIST OF TABLES

NOMENCLATURE

d	Displacement response at a point in the wheelset
c	Position vector of the same point in the undeformed state
u	Time-varying dynamic displacement vector
t	Time
$\mathbf{q}_w(t)$	Generalized coordinate vector
Φ	Modal matrix of the wheelset
σ	Stress vector
D	Elasticity matrix
L	Linear operator
ε	Strain
u	Displacement
$\mathbf{F}_{wri}$	Contact forces at each wheel/rail interface ($i=1,\ldots,4$)
$\mathbf{F}_{syi}$	Lateral forces due to discrete supports ($i=1,\ldots,N_s$)
$\mathbf{F}_{szi}$	Vertical forces due to discrete supports ($i=1,\ldots,N_s$)
N_s	Number of supports
$\mathbf{M}_{Gi}$	Moments caused by wheel/rail contact forces ($i=1,\ldots,4$)
$\mathbf{M}_{si}$	Moments caused by support forces ($i=1,\ldots,N_s$)
x_{wi}	Position of each wheel along the rail ($i=1,\ldots,4$)
x_{si}	Position of ith discrete support along the rail
z	Vertical deflections of the rail
ψ_y	Bending deflections of the rail
m	Mass of the rail per unit length
ρ	Mass density
A	Rail cross section area
G	Shear modulus
E	Young's modulus
I_y	Second moment of area of the rail cross section about the y-axis
κ_z	Vertical shear coefficient
$\delta(x)$	Dirac delta function
N_w	Number of wheelsets

y	Lateral displacement of rail
ψ_z	Yaw displacement of rail
F_{wryj}	Lateral forces due to wheel/rail contact
I_z	Second moment of area of the rail cross-section about the z-axis
κ_y	Lateral shear coefficient
I_0	Polar moment of inertia of the rail cross-section
κ_x	Torsional stiffness coefficient
$q_{zk}(t)$	Generalized modal coordinates for vertical deflection
$\omega_{yk}(t)$	Generalized modal coordinates for bending deflection
$q_{yk}(t)$	Generalized modal coordinates for lateral deflection
$\omega_{zk}(t)$	Generalized modal coordinates for yaw deflection
$q_{Tk}(t)$	Generalized modal coordinates for torsional deflection
$Z_k(x)$	Rail mode shape function for vertical deflection
$\Psi_{yk}(x)$	Rail mode shape function for bending deflection
$Y_k(x)$	Rail mode shape function for lateral deflection
$\Psi_{zk}(x)$	Rail mode shape function for yaw deflection
$\Phi_k(x)$	Rail mode shape function for torsional deflection
N	Number of modes considered for each coordinate
F_{szi}	Vertical forces due to discrete supports between the rails and the track slab
F_{pi}	Vertical forces arising at the CAM-slab interface
z_s	Vertical deflection responses of the slab
$[M]$	Global mass matrices of FE model of the track slab
$[C]$	Global damping matrices of FE model of the track slab
$[K]$	Global stiffness matrices of FE model of the track slab
Z_i	Generalized modal coordinates vector corresponding to the ith mode
$\{\phi\}_i$	ith mode shape function of the track slab
N_m	Total number of vibration modes considered in the slab model
$\Delta z_i(t)$	Wheel/rail overlap in the vertical direction
C_H	Hertzian contact coefficient
z_{wi}	Vertical motion of the wheel

$z(x_{wi},t)$	Vertical motion of the rail at the contact point
$r_i(t)$	Geometry of the wheel defect
D_{fi}	Flat of depth
L_{fi}	Length of wheel flat
R	Wheel nominal radius
(x, y)	Coordinates of a point on the wheel circumference
A	Amplitude of the polygonal wear
ΔR	Variation in the wheel radius of the polygonal wheel at the wheel/rail contact
A_i	i^{th} Fourier expansion
B_i	i^{th} Fourier expansion
$\tilde{r}_\theta$	Rms value of the wheel surface roughness corresponding to the order θ
L_θ	Roughness in dB
V_{wear}	Wear volume within the slip region of the contact patch
H	Material hardness of wheel tread
k_w	Wear coefficient
d	Sliding distance
$p_z(x,y)$	Contact pressure at a point within the contact patch with coordinates (x,y)
(x_{ij}, y_{ij})	Coordinate of the center point of i_{th} element within the j_{th} strip
$\Delta z(x_{ij}, y_{ij})$	Wear depth for each element
$s(x_{ij}, y_{ij})$	Slip velocities in the x and y directions for each element
Δt	Time increment
Δx_j	Element length of the j_{th} strip
Δz_j	Total wheel wear within a strip j
RM	Roughness magnitude of wheel
α	Regression constant
β	Regression constant

ACRONYMS

TEI	Thermo-Elastic Instability
OOR	Out-Of-Round
ICE	Inter-City Express
CAM	Cement Asphalt Mortar
DOF	Degree of Freedom
FE	Finite Element
FEMBS	Finite Element Multi-Body Systems
SIMAT	SIMPACK-MATLAB
FFT	Fast Fourier Transform
DFT	Discrete Fourier Transform
PSD	Power Spectral Density

CHAPTER 1: LITERATURE REVIEW AND SCOPE OF THE DISSERTATION

1.1 Introduction

The wheels of a rail vehicle commonly develop defects over time, which may be classified as either local defect, such as a wheel flat, wheel spalling and wheel shelling, or periodic defects, such as wheel corrugation and wheel polygonalization. The effects of local defects on dynamic responses of railway systems have been widely investigated considering the wheel-rail interaction at relatively low speeds [1,7,39,49]. These have invariably shown that local wheel defects cause high magnitude impact forces at the wheel-rail interface, which can lead to fatigue failures of the track system and vehicle components. In high-speed operation, the local wheel defects lead to substantially higher frequency contact forces at the wheel/rail interface, which excite high-frequency vibration modes of the vehicle subsystems and track subsystems. These may contribute to the developments in periodic defects on the wheel circumference [1,25,30]. The definite mechanisms leading to periodic wheel defects in high-speed trains, however, are not yet fully understood, although the effects of such defects on dynamic responses of high-speed railway have been reported in a few studies.

The track system used for the high-speed railway is generally supported on the slab since the slab yield relatively lower magnitudes of track irregularity compared to the ballast track. The high stiffness of the slab support system, however, contributes considerably to high magnitudes of impact loads in the presence of a wheel defect, when compared to those encountered with the ballast track. Such impacts can lead to growth in the wheel surface irregularities, which have been characterized by high-order periodic defects on the wheel circumference, referred as wheel polygonalization [30,31,33]. Polygonal wheel wear of order as high as 24 has been reported in a recent study on high-speed railway wheels [34]. Such polygonal wear can cause high magnitude wheel/rail impact loads at frequencies above 700 *Hz* at an operating speed near 300 *km/h*, which may excite various vibration modes of the vehicle/track system [33,34]. High magnitude and high-frequency wheel-rail contact forces, arising from high-order polygonal wear of the wheels, have been associated with high magnitude noise emission and failures of different structural components, such as those of the axle box and gearbox [71]. Only limited efforts, however, have been made thus far to establish an understanding of the propagation of low-order wheel polygonalization to a

substantially higher order. The mechanisms leading to high-order wheel polygonalization remains exclusive, although it has been observed through field measurements. With increasing demands for the operation of railways at higher speeds, it is vital to gain a clear understanding of mechanisms leading to high-order polygonal wear of the wheels and the effects of wheel polygonalization on dynamic responses of the vehicle system. This will facilitate the development of a wheel-maintenance criterion to ensure safe operation of high-speed trains.

This dissertation research is aimed at characterization of high-order polygonal wear of wheels of a high-speed train, and dynamic response analyses due to excitations arising from both the local as well as periodic wheel defects. A comprehensive vehicle/track system model is developed considering flexibility of the wheelset and the axle box to investigate dynamic responses of a high-speed railway car due to the local as well as periodic wheel defects. A long-term measurement campaign is described for characterization of periodic defects and to study the propagation of high order polygonal wear of the wheels. The mechanism leading to high-order polygonal wear is further investigated through analysis of a long-term wear iteration model, developed by integrating a short-term Archard wear model to the coupled vehicle-track system model.

1.2 Literature review

A study of the formation of high-order wheel defects and effects of wheel polygonalization-induced dynamic responses of a high-speed rail vehicle encompasses various challenges associated with characterization and propagation of wheel defects, modelling of coupled vehicle/track system considering flexibility of the track and vehicle components, wheel/rail interactions, and wheel wear model. The reported relevant studies are reviewed to build essential knowledge on challenges and methods of analysis. The reported studies grouped under relevant subjects are briefly discussed below in order to develop the scope of the present investigation.

1.2.1 Characterization of wheel defects

Owing to the wheel-rail interactions, the railway wheels incur different forms of defects, which may be grouped on the basis of the wavelength of the wheel surface irregularity, namely short-and long wavelength defects. The flats, shelling and spalling in the circumferential surface of the wheel are regarded as local defects with short wavelength, while the corrugation and polygonal wear of the circumference possess longer wavelength [1]. Fig.1.1 illustrates examples of wheel surface defects. A number of studies have investigated the formation mechanisms of different types of

defects, resulting influences on the vehicle system and the mitigation methods, which are discussed in following sub-sections.

(a)

(b)

(b)

(d)
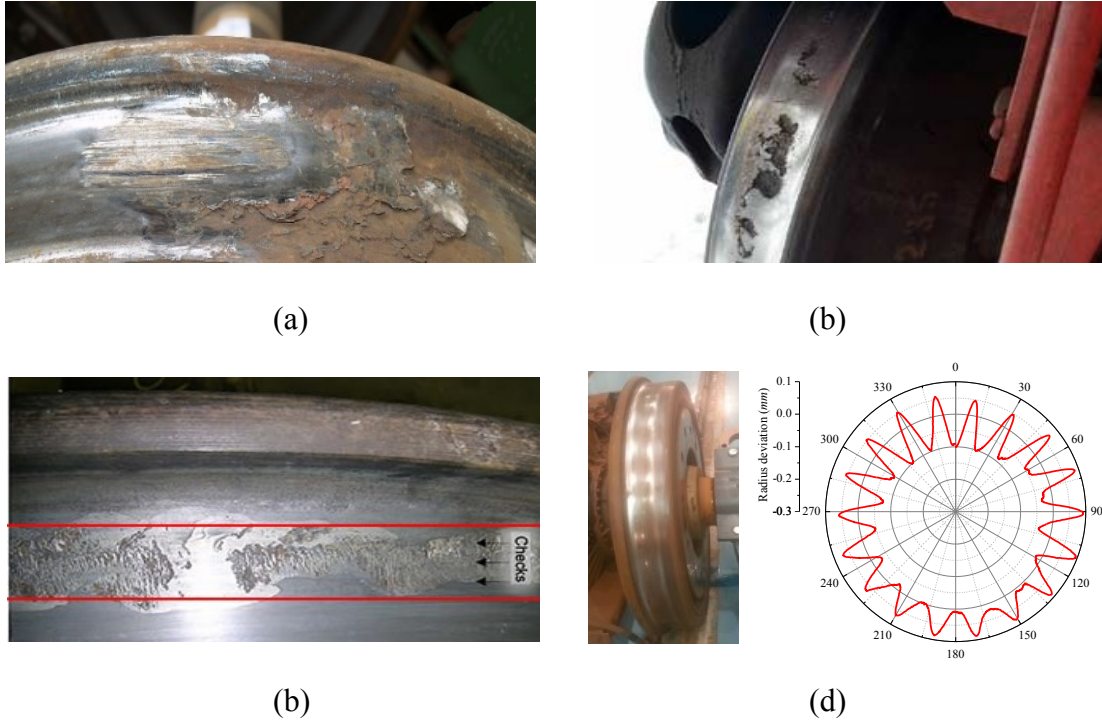
Figure 1.1: Examples of wheel defects: (a) wheel flat; (b) wheel spalling; (c) wheel shelling; and (d) wheel polygonalization.

1.2.1.1 Formation mechanisms

Wheel flats: A wheel flat is a flat spot on the rolling surface of a wheel, generally caused by sliding of the wheel on the rail. The wheel sliding could be attributed to poorly adjusted, frozen or defective brakes, or high magnitude of braking force compared to the available wheel/rail adhesion [2,3]. The contamination of the rail surface, such as leaves, grease, frost or snow, is also known to contribute to the formation of wheel flats[4]. Kumagai *et al.* [5] discussed factors limiting wheel/rail adhesion leading to wheel sliding and proposed preventive measures. During sliding, the local temperature build-up within the contact patch followed by rapid cooling leads to the formation of brittle martensite around the flat and residual stresses beneath the surface of the wheel. The interaction of a rolling wheel with a flat with the rail leads to high magnitude impacts. With continued service, the cracks may develop in the wheel surface due to the rolling contact stresses [4]. Jergeus [6] developed a finite element model to evaluate residual stresses due to a local thermal shock to investigate mechanism leading to the formation of a wheel flat. The study concluded that

a brittle martensite phase developed during sliding and thereby high tensile stresses in the wheel rim beneath the top layer of the phase transformations may initiate or propagate cracks into the rim resulting in spalling. The study involved various simplifying assumptions in the phase transformations, while a rapid temperature change was assumed over each time step without the phase transformation.

The formations of wheel flats have also been investigated experimentally in a few studies. Jergeus [4] performed experiments on full-scale railway wheels with more than 200 wheel flats under controlled conditions involving different wheel loads, rolling speeds, sliding duration, and friction coefficient between the wheel and the rail. Martensite was found beneath all the flats and cracks were observed in most cases. Snyder *et al.* [7] experimentally investigated the growth of a wheel flat using a rolling test rig and concluded that the arc of a newly formed flat increases with the impact forces developed at the wheel-rail interface, and the flat tends to become a chord flat. Moreover, the high magnitude impact forces developed at the wheel-rail interface can lead to increased potential for the hot box incidences, burnt journals, broken wheels and rail fractures.

Spalling and Shelling: Spalling is a result of thermo-mechanical interaction between the wheel and the rail, which commonly propagates from cracks induced by high transformation stresses in the martensite layer. The martensite is a brittle layer underneath the wheel tread with 0.1~0.2 *mm* thickness, where the cracks can easily be developed due to the wheel/rail rolling contact stress. Stone *et al.* [8] presented a detailed review of wheel spalling, and Sun *et al.* [9] discussed methods for reducing wheel spalling. Makino *et al.* [10] studied the effects of material properties on spalling of wheels via experiments and suggested that the maximum flat depth and thickness of martensite depends on a parameter related to flat generation energy, and the life of spalling could be determined by the rolling contact fatigue property. The study, however, did not clearly state martensite formation as the main causal factor of spalling.

Wheel shelling is defined as the loss of material from the wheel tread due to high magnitude vertical wheel/rail contact force and the rolling contact fatigue [11], which is usually generated along the wheel circumference with a width of about 10 *mm* [12]. The shelling cracks are initiated predominantly at the non-metallic inclusions and are primarily caused by high magnitude vertical wheel/rail contact forces [13].

Wheel corrugation: Wheel corrugation can be seen as small size multiple flats on the wheel surface, which lead to wheel/rail noise [1]. The wavelength of wheel corrugation mainly ranges

from 30 to 70 *mm* with amplitude of about 400 *μm*. The thermo-mechanical interactions between the brake block and the wheel rim are usually the primary factors contributing to wheel corrugation [13,14,15]. An indication of wheel corrugation is the generation of a hot spot on the wheel as a result of the thermo-elastic instability (TEI) between the brake block and the wheel tread [16]. A comprehensive review of the thermo-mechanical coupling between the brake block and the wheel has been presented by Barder and Ciavarella [17,18]. Using the finite element method, Geijselaers and Koning [19] studied the development of wheel corrugation due to the thermo-elastic instability. Vernersson [14,15] investigated the wheel-brake block interactions at a constant speed during braking, experimentally and theoretically, and concluded that the wheel-block interactions contribute to the generation of hot spots on the wheel tread and lead to wheel corrugation following the braking.

Wheel polygonalization: Polygonal wear is a periodic radial irregularity around the wheel circumference superposed on the wheel radius. Polygonalization is generally characterized by variation in the wheel radius, while the waviness is defined in terms of harmonic order of wheel surface defect (variations in the wheel radius). Earlier studies on wheel surface irregularities were mostly limited to the lower orders of wheel wear. These have suggested that the lower-order wheel polygonalization is caused by various factors such as wheel re-profiling process [1,21], brake blocks-induced thermo-elastic instability [13], bending vibration of the wheelset [23,25,26], track properties [25,27] and dynamic unbalance of the wheel [1,16,24]. The definite mechanisms leading to the formation of high order polygonal wear of the wheel, however, have not yet been fully understood. A thorough review of studies reporting low order polygonal wear (1~5th order) has been presented by Nielsen *et al.* [1,16], including the formation mechanism and the wheel removal criteria. Studies have reported 3rd and 2nd orders of polygonal wear in the solid wheels and rubber wheels, respectively, in trains operating in Germany [1,20]. Rode *et al.* [21] suggested that the third order harmonic waviness around the wheel circumference is likely caused by the claw clamping of the wheel during re-profiling operations. Similar conclusions were also reported by Johansson [22] on the basis of measurements of 99 different wheels employed in high-speed, freight and commuter trains. In the wheel re-profiling procedure, the ground lathe is supported under the wheel tread rather than the wheel centre, which can lead to low magnitude radial irregularities on the wheel tread.

Apart from the initial residual irregularities caused by the wheel re-profiling procedure, the wheel polygonalization has been associated with gradual wheel wear caused by the brake block and the wheel-rail interaction. Kaper [13] described the wheel polygonalization phenomenon in Netherland's railways and its effects on noise emission. The study suggested that wheel polygonalization defect is attributable to the brake block-induced thermo-elastic instability or the material transfers during braking. Brommundt [23] attributed the development of out-of-round (OOR) wheels to the wheel/rail wear and concluded that increase in speed contributes to deformations dominated by the lower order harmonics. Besides, the dynamic unbalance and material inhomogeneity in the wheel may also contribute to lower order harmonics of the continuous or periodic circumferential defects [24].

The dynamic deformations of the flexible track and vehicle components may also contribute to wear of the wheels and the rail. A few studies have suggested the low-order polygonal wear may develop into the higher order polygonalization. Owing to highly nonlinear wheel-rail interaction and flexibility of the track and vehicle components, comprehensive simulation models are desirable to develop a better understanding of the evolution of the wheel polygonalization from the lower to the higher order harmonics. Morys [25] developed an iterative simulation methodology involving simulations of the vehicle/track and wheel wear models to study evolutions of the OOR defects over relatively long periods. The study concluded that wheels with OOR defects could cause substantially higher impact loads at the wheel/rail interface, especially when operating on a relatively stiff track. Meywerk [26] proposed an iterative long-term simulation model together with a work hardening wheel tread model to account for the effects of varying hardness on the wear rates. The results suggested that the first and second bending vibration modes of the wheelset contribute considerably to the propagation of OOR defects, which may be further affected by the phase shift between the OOR deformities of the left and right wheels.

Johansson *et al.* [27] studied the growth of OOR deformities using a similar long-term iteration scheme considering a three-dimensional train-track interaction model together with a long-term wear model based on the Archard law of wear. The study suggested that the dominant wavelength of the wheel OOR is primarily related to the vertical mode resonance frequencies of the coupled train-track system and the vertical anti-resonance of the track. This iteration scheme was also employed by Luo *et al.* [28] to simulate the evolution of wheel OOR considering lower order initial harmonic irregularities of the wheel circumference. The study observed considerably

higher propagation rates of high order irregularities than those of low order irregularities, and negligible effect of track irregularities on the evolution of wheel polygonalization, when the excitation frequency is away from the wheelset bending mode frequency.

A few studies have shown that high magnitude impact loads could excite various bending and torsional deformation modes of the wheelset [29], which could cause higher lateral slippage of the wheel and wheel/rail material excavation, and thereby enlargement of the OOR deformities. Jin *et al.* [30] experimentally investigated the effects and growth of polygonal wear of subway wheels and concluded that the ninth-order polygonal wear observed in wheel deformations was due to the first bending mode of the wheelset. Chen *et al.* [31] attributed the 8th ~10th order wheel polygonalization, observed in the metro cars' wheels, to the self-excited vibration (less than 150 *Hz)* at the wheel-rail interface.

The aforementioned investigations have mostly focused on the low order wheel polygonalization, up to order 5, while the continuing increase in speed of high-speed trains can intensify the wheel/rail interactions and lead to higher order wheel polygonalization. A few recent studies have observed high order wheel polygonalization, ranging from 18 to 24, in wheels of high-speed trains [32,33,34]. Wu *et al.* [33] and Zhang *et al.* [32] observed the 20th order wheel polygonalization in wheels of a high-speed rail vehicle operating at a nominal speed of 300 *km/h*. From data acquired through filed tests on wheels of a high-speed train operating at a speed near 250 *km/h*, Wu *et al.* [34] reported the wheel polygonalization of order 23. Such high order polygonal irregularities of the wheel tread tend to cause high magnitude and high-frequency impact loads at the wheel-rail interface. The frequency of the wheel-rail contact force approaches near 600 *Hz* at a forward speed of 300 *km/h*, which may excite resonant responses of some of the structural components. The primary causal factors leading to such high order polygonal wheel OOR, however, have not yet been clearly identified.

1.2.1.2 Effects of wheel defects

The interaction of a wheel with OOR defects with the rail has been associated with considerable vibration and in-service failures of structural components due to the high magnitude impact loads developed at the wheel-rail interface. The effects of wheel defects of local as well as periodic nature on dynamic responses of the wheelset, bogie, and the car body have been widely investigated using the analytical models and experiments. The wheel shelling and wheel spalling are regarded as the local defects similar to wheel flats, while the wheel corrugation and polygonalization represent

defects of continuous nature. The wheel OOR defects have thus been generally treated as either flat or polygonalization with different dimensions in the reported studies. The reported effects of wheel flat and the wheel polygonalization on the dynamic responses of the vehicle are summarized below.

Wheel flats: In the simulation model, the geometry of a wheel flat is commonly described by either a chord-flat or a cosine-flat [35]. A chord-type flat represents a newly formed wheel flat with sharper edges. During service, the sharper edges of chord-type flat tend to become more rounded, which is more adequately described by a cosine-type flat, also referred to as a haversine flat [36,37]. Majority of the studies have considered haversine flats for investigating the effects of flats on wheel/rail impacts [7,38,39,40,41,42,43]. These investigations have shown that wheel flats, invariably, cause high magnitude impact forces at the wheel-rail interface, and contribute considerably to high-frequency vibrations of the rail and the wheelset. The flat-induced contact forces are strongly depended upon a number of design and operating parameters such as wheel load, speed, and track and vehicle properties apart from the geometry of the wheel flat [29,36,40].

The estimation of wheel/rail contact force is highly depended on the accuracy of the vehicle/track dynamic model. A number of investigations have been performed to illustrate the robustness of different track models in the presence of a wheel flat. Newton *et al.* [39] experimentally investigated the effects of wheel flats on dynamics of railway vehicles, and used measured data to examine the validity of different track models. The study concluded that the track model employing a Euler beam on the elastic foundation adequately describe the effects at low speeds, while it overestimates the effects of impact forces at high speeds. The discrete support model was considered to represent the track more realistically, while Timoshenko beam model provided more accurate estimations of rail deflections. Considering shear deformations and rotational inertia of the rail, the Timoshenko beam has been widely used to assess the high-frequency vibration responses of the rail up to 2500 *Hz* [80]. Nielsen *et al.* [38] developed a vehicle/track dynamic model using the state-space vector approach in conjunction with complex modal superposition for the track to investigate the effects of rail corrugation and wheel flats on the wheel/rail contact forces.

Johansson *et al.* [44] investigated the wheel flats-induced impact forces experimentally and analytically. The study examined the validity of two types of track models, namely, the linear [45] and the state-dependent track model [38] using the measured data. The results suggested that the

linear model underestimates peak wheel/rail impact forces up to the speed of 50 *km/h*, and overestimates the forces above 70 *km/h*. Although the state-dependent track model showed better agreements with the measured data, it also overestimated the impact forces for speeds above 70 *km/h*. A number of studies have investigated the effects of various vehicle/track design and operating parameters on the magnitudes of wheel flat-induced dynamic loads. Dukkipati *et al.* [46] developed a finite element model of the vehicle-track system to study the impact loads caused by chord-type and haversine wheel flats. The study concluded that the magnitudes of impact loads are strongly affected by the shape and size of the flat, axle load, vehicle speed, and rail-pad stiffness. The study further reported that reducing the rail-pad stiffness could lower the magnitude of the impact force. The results were in good agreement with the measured data reported by Fermer and Neilsen [49] on the effect of rail pad stiffness on the impact loads caused by a wheel flat. While a few studies have applied similar track models to evaluate wheel flat-induced contact forces at higher speeds, the validity of the models for the application to the high-speed train, operating at speeds up to 350 *km/h* has not yet been demonstrated. Zhai [47] investigated the impact of a wheel flat on dynamic responses of a high-speed train at a speed of 160 *km/h* considering a Bernoulli-Euler beam representation of the rail. Sun and Dhanasekar [48] employed a similar vehicle model coupled with a Timoshenko beam rail model to study the influences of wheel flats on variations in the wheel/rail contact forces. The validity of the model was demonstrated by comparing the simulation results with the measured data reported by Fermer and Neilsen [49]. The impacts of the wheel flat with the rail is also known to be among the primary sources of wheel/rail noise emission. Wu and Thompson [50,51,52] conducted a number of investigations on the noise emissions due to wheel flats and concluded that the wheel flats-induced noise levels are highly dependent on the vehicle speed, and the noise level increases considerably with increasing train speed.

The aforementioned studies on impact forces due to wheel flats have invariably considered negligible contributions of the wheelset deformation. A few studies have suggested that high magnitude impact forces arising from wheel or rail defects may cause elastic deformations of the wheelset. Moreover, the impact forces contribute to relatively higher frequency excitations, especially at high speeds, which may excite various deflection modes of the wheelset and other structural components. A few studies have incorporated flexible wheelset models to the car models considering several deflection modes of the wheelset. Morys [25] developed a flexible wheelset model by introducing linear elastic and damping elements to account for bending and torsional

deformations of the wheelset shaft. This model was validated in terms of the first bending and torsion mode frequencies of the wheelset.

A flexible wheelset model with discrete elastic and viscous elements, however, is considered valid only for the lower vibration modes of the wheelset. Alternatively, a few studies have employed the modal approach to describe high-frequency vibration modes of the rotating as well as non-rotating wheelsets. Nielsen *et al.* [53] used the modal method to develop a non-rotating flexible wheelset model, which was integrated to a vehicle-track dynamic model to investigate the influences of rail corrugation and wheel out-of-roundness on the vertical wheel-rail contact forces. The study concluded that consideration of the wheelset flexibility in the model yields lower magnitudes of wheel/rail contact forces, when compared to those encountered with a rigid wheelset. Popp *et al.* [54] used the modal approach to develop a rotating flexible wheelset model to study the influences of the wheelset flexibility on the stationary wheel/rail interactions and the hunting stability of the vehicle. The above studies have shown that the wheelset flexibility contributes considerably to high-frequency dynamic responses of the vehicle. Using the Eulerian approach Baeza *et al.* [55,56,57] developed a rotating flexible wheelset model to study the high-frequency vehicle's responses due to a wheel flat and rail corrugation. Nielsen *et al.* [58] compared the wheel/rail contact force responses obtained from the rigid, and non-rotating and rotating flexible wheelset models at high speeds, and concluded that the rotating flexible wheelset model yields more reliable estimation of the wheel/rail contact forces in the high-frequency range. Martinez-Casas *et al.* [59] employed the rotating flexible wheelset model to investigate the stresses developed in a wheelset axle due to the rail corrugation and wheel flats. The study identified a significant increase in the axle stress due to the wheel defect-induced impact forces.

The reported investigations mainly focused on the effects of the wheel flats on a rail vehicle traveling on the ballast supported track running at low speeds. The impact loads induced by a rail vehicle running over a slab track are expected to be more prominent in the presence of the wheel flat due to the relatively higher stiffness of the slab track. In addition, the validity of the models has been demonstrated at speeds below 140 *km/h* using the experimental data reported by Fermer and Neilsen [49,60] and Newton and Clark [39].

<u>Wheel polygonalization:</u> This periodic circumferential wear has been associated with high magnitudes of high-frequency impact loads at the wheel/rail interface, which contributes to undesired dynamic responses and reduced fatigue lives of the vehicle/track sub-structures,

especially under high-speed operations [1,33,61,62]. The low order polygonal wear of the wheels such as 1st order and 3rd order, have been widely reported for the freight and conventional low-speed passenger cars' wheel [1]. Owing to highly adverse effects of wheel polygonalization, considerable efforts have been made to build a better understanding of the effects of periodic circumferential defects in railway wheels. A thorough review on the effects of wheel polygonalization has been reported by Barke and Chiu [61] including the wheel/rail impacts, rail fatigue, rail joint deterioration, sleeper degradation as well as the noise generation. Earlier studies on wheel polygonalization were mainly related to the wheel polygonalization-induced wheel/rail noise problems [1,13]. These evolved in development of resilient wheels to mitigate both the wheel-rail contact force and the wheel/rail noise [13]. However, the fatigue lives of resilient wheels were found to be substantially lower compared to those of the rigid wheels. This was considered as polygonal wear of the resilient wheel as the main causal factor of the derailment of an inter-city express (ICE) train in 1988 in Germany [1,14].

The profile of a polygonal wheel is generalized idealized by a harmonic variation superposed on the wheel circumference [33,63,64,65]. The coupled vehicle/track dynamic model representing the track system and wheelset as flexible components is generally used to investigate the effects of wheel polygonalization on dynamic responses of the vehicle and track system, in terms of wheel-rail contact forces, axle box acceleration and ride comfort, as well as oscillations of the track. High magnitude and high-frequency wheel-rail contact forces induced by the wheel polygonalization have been reported in a number of investigations [28,29,33,62,64,66]. Whereas, the effects of wheel polygonalization on the ride comfort are considered negligible since the excitation frequencies are well above the range of frequencies associated with human discomfort [28,67].

The reported studies on the effects of wheel polygonalization are mainly limited to the lower order wheel polygonalization in a relatively low-speed range. A few studies have observed wheel polygonal wear of considerably higher orders, ranging from 18 to 24. Such high orders of wheel polygonalization could pose greater challenges to running safety of the high-speed trains. Using a vertical vehicle/track coupled dynamic model, Liu *et al.* [64] reported that a polygonal wheel generates considerable fluctuations in the wheel/rail contact forces, and the impact forces become more sensitive with the increasing speed, especially for the higher order polygonal wheels. Chen [68] reported that strong adverse effects of the higher order wheel polygonalization (20th order) on the fatigue lives of vehicle components, while the effects on stability limits could be considered

negligible. The contributions due to the flexibility of the wheelset, however, was ignored. Higher order polygonal wear of the wheels contribute considerably to high-frequency variations in wheel-rail contact forces, which could excite various deflection modes of the wheelset and the axle box [29]. A recent study has shown that the higher order wheel polygonalization causes considerably higher wheel/rail noise and interior noise, which is strongly dependent on the roughness of the wheel surface [32]. The high magnitude impact loads induced by the wheel polygonalization can also give rise to higher magnitudes of dynamic stresses in the wheelset axle, and substantially lower residual lifetime in the presence of a pre-existing crack [33,62]. Through the study of microstructure of the wheel, Pan *et al.* [69] concluded that the wheel polygonalization-induced impact loads can substantially affect the hardness of wheel tread material due to the work hardening. The study further showed nearly polygonal distribution of the material hardness on a polygonal wheel. Similar results were also reported by Kaper [13].

1.2.1.3 Mitigation methods of wheel defects

A number of studies have proposed measures to mitigate the effects of wheel defects including the wheel re-profiling process, operating parameters of the vehicle/track system and the wheel materials. The wheel re-profiling process is generally regarded as one of most common methods for removing defects from the wheel. In this process, a ground wheel lathe is usually employed, in which the wheelset is not separated from the vehicle but is simply supported on the tread rather than entirely at the wheel centre. The ovality or long wavelength irregularities in the wheel circumference are thus not entirely eliminated in this process [70]. Alternatively, re-profiling of the wheels removed from the vehicle and centred at the axle centres has been suggested to achieve more accurate re-profiling of the wheel [76]. This, however, is considered more costly and highly inefficient. Other re-profiling strategies such as the repeated re-profiling procedure using the ground wheel lathes has been proposed to eliminate the residual irregularities from the initial re-profiling procedure [71]. Alternatively, surface grinding of the wheel tread has been proposed. In the process, the grinding machine is used for re-profiling of the wheel tread at a low speed. The experimental studies have concluded that the wheel tread grinding can substantially reduce the growth rate of wheel roughness and increase the interval between successive wheel re-profiling cycles. Moreover, the grinding method is relatively more cost-efficient than the turning process, which has been widely used in China's high-speed rail vehicles and Japan's Shinkansen [71].

The wheel re-profiling process is generally governed by some removal criterion of wheel defects. Widely different criteria, however, have been employed by different railway operators. These are mostly based on either the impact loads arising from the wheel defects, or the size of defects or the magnitude of emitted noise. A thorough review of different wheel removal criteria has been reported by Nielsen *et al.* [1] including those commonly employed in North America and Sweden. In North America, the allowable length of the wheel flat is 63.5 *mm*, while the wheel must be replaced when the peak impact load exceeds 445 *kN* [1]. In Sweden, it is required that the vehicle approaches the nearest maintenance facility at a low speed when length of the defect lies in the 40 to 60 *mm* range or when the depth of the defect is less than 1 *mm*. The vehicle, however, must approach the nearest manned station at a speed less than 10 *km/h*, when length of a defect exceeds 60 *mm* or the defect depth is larger than 1 *mm* [1]. European standard, EN 15313[72], specifies the acceptable lengths of defects on the tread (flats) depending on the axle load, wheel diameter and vehicle speed [72], as summarized in Table 1.1. The standard also suggests the allowable deviation in radius of the wheel, as listed in Table 1.2.

Since the wheel flat is more related to the wheel sliding with respect to the rail, the anti-sliding control has been widely employed during acceleration and braking. A number of experimental tests as well as simulation models have been used to identify the optimal vehicle and track system parameters for the anti-sliding control strategy [73,74,75]. Although the formations of wheel polygonalization have not yet been fully understood, it is expected that the mitigation of wheel polygonalization would require alternate parameters of the vehicle and track system, which could be related to the bending stiffness of the wheelset axle and the rail, and damping property of the rail pads. Since the formation of wheel defects is strongly related to the wear process occurring at the wheel-rail interface, the materials with relatively higher resistance to wear have been suggested for the wheels. The wheel material used in Shinkansen train in Japan has shown far greater wear resistance compared to the frequently used wheel material, R7 [76]. Some studies have also suggested that increasing the hardness of the wheel tread can reduce the rate of wear [71]. Increasing the tread material hardness, however, presents a greater potential risk for the formation of other defects such as spalling.

Table 1. 1: Acceptable lengths of the wheel tread flats [72].

Axle load (tons)	≤18			18-22.5				>22.5		
Speed (km/h)	≤160	160-200	>200	≤120	120-160	160-200	>200	≤100	100-120	>120
Wheel Diameter (m)	Acceptable length of wheel tread defect (flat), mm									
>1	80	60	40	80	60	50	35	×	×	×
0.84-1	60	50	30	60	50	35	25	60	50	30
0.63-0.84	40	30	25	40	30	25	20	40	×	×
0.55-0.63	35	25	×	×	×	×	×	×	×	×
<0.55	30	×	×	×	×	×	×	×	×	×

Table 1. 2: Allowable deviations in radius of a wheel with out-of-roundness (OOR) defect [72].

Wheel diameter (m)	Maximum speed (km/h)	Permitted OOR, mm (deviation in radius)
>0.84	<60	1.5
	60-160	1.1
	160 – 200	0.7
	>60	0.5
0.38 to 0.84	<200	0.7
	>200	0.5
<0.38		0.3

1.2.2 Modelling of the vehicle/track system

The evolution of wheel defects is mostly related to forces arising at the wheel-rail interface. The characterization of the contact force during service via experimental means is extremely complex. Consequently, a wide range of simulation or analytical models of the vehicle/track system have been developed for characterization of the wheel-rail interaction as a function of various design and operating factors. These include analytical models of different types of tracks and vehicles,

which are coupled by the highly nonlinear wheel-rail contact models. The reported models are briefly discussed in the following sub-sections.

1.2.2.1 Modelling of the track system

High magnitude impact forces arising from the wheel defects could cause deflections of the track system and thus affect the contact forces at the wheel/rail interfaces. It is thus vital to incorporate the dynamic behaviors of the track system in the coupled vehicle/track system models. A large number of models of the track system with varying complexities have been reported for analysis of the track deformation responses to the moving wheels' loads. The railways generally employ two types of tracks, namely, the ballast track and the slab track, as shown in Fig. 1.2. The ballast track generally consists of the rail, fasteners, sleepers, ballast and sub-ballast, while the slab track includes the rail, fasteners, sleepers, concrete slab and the hydraulic sub-base [77,78]. Track models are formulated through integration of the structure's components models, which are described below.
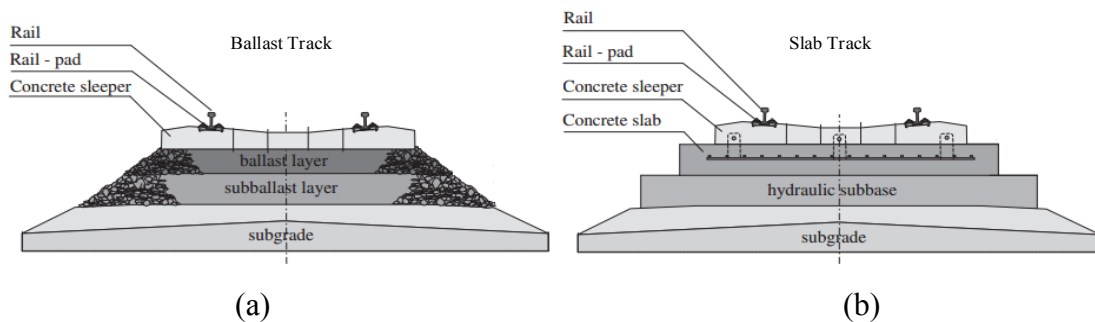
Figure 1.2: (a) ballast; and (b) slab track [77,78].

Rail models: Rail constitutes one of the most important components for analysis of the vehicle/track interactions, which directly affects the dynamic wheel/rail contact and responses of the vehicle components. Accurate representation of the rail is thus essential for predictions of the wheel/rail contact forces. The simplest way of modelling the rail is to consider the rail as a lumped mass, supported on stiff springs [79]. The beam representation of the rail is generally employed for the study of dynamic responses of the rail under wheel/rail forces. In general, the rail is considered as either a Euler-Bernoulli beam or a Timoshenko beam. The Bernoulli-Euler beam has been shown to accurately describe the rail responses up to about 500 *Hz* in a computationally efficient manner [80]. This formulation, however, can yield substantial errors at higher frequencies, as the shear deformation of the rail becomes increasingly important. Alternatively, Timoshenko beam

modelling approach has been widely used for predicting the rail responses at frequencies up to 2.5 *kHz*. Newton *et al.* [39] compared the responses of the Euler and the Timoshenko beam rail models with the measured responses in the presence of wheel flats. The study concluded that the Euler beam overestimates the impact loads at the high frequencies, while the Timoshenko beam model characterizes the rail deflections and impact loads more realistically. The assumption of the rigid cross-section used in the beam theory, however, is not considered applicable in studies on noise emissions. The finite element models of the rail and the wheel have thus been employed to account for elastic deformations in the cross section [81,82].

The rail fastener system mainly includes a rail pad beneath the rail and two fastener springs on each side of the rail foot. The rail pads made of either elastic rubber or composite materials are designed to reduce the magnitude of impact forces transmitted to the sleepers. Fenander [83] experimentally investigated the stiffness and damping properties of rail pads, and concluded that the stiffness of rail pads increases considerably with an increase in the preload and the dominant frequency of the dynamic wheel load. Through experiments, Remennikow *et al.* [84] concluded that elastic properties of the pads may deteriorate during the service life due to repeated high-intensity wheel impacts and extreme weather conditions. Relatively soft rail pads have been considered favorable for limiting the loading of sleepers and the ballast [36]. The experimental study by Fermer and Nielsen [49], however, suggested that soft pads may not always yield lower wheel/rail contact forces. Ilias [85] investigated the influence of rail pad stiffness on the wheelset/track interactions using a long-term wear iterative model, and suggested that the stiffer rail pads lead to faster growth of corrugation on the rail.

Sleeper models: Sleeper is a beam-like structure that is used to discretely support the rail on the ballast. In the coupled vehicle/track dynamic models, the sleeper is considered as either a Euler beam or a Timoshenko beam to account for deformations induced by the wheel/rail impacts [86,87]. Most of the studies, however, consider sleeper as a rigid body neglecting possible deformations due to the wheel/rail impacts. Knothe *et al.* [80] suggested that a rigid sleeper model accurately describes the response of the railhead up to 1 *kHz*. Through simulations of a coupled vehicle/track dynamic model incorporating sleeper as a rigid body, Xiao *et al.* [88] investigated the effects of sleeper support failure on dynamic behaviors of the vehicle system. The study concluded that the sleeper support failure can cause high magnitude shock loads at the wheel-rail interface, when the wheel passes through a failed section.

Ballast and subgrade models: The ballast and subgrade constitute the foundation of the track system and represent strongly non-linear features of the track system. A number of analytical models have thus been formulated for a better representation of features of the ballast and the subgrade [80]. Two-parameter vertical linear models, representing the ballast and subgrade as a massless spring-damper element, has been widely used in a variety of investigations focusing on the low-frequency performance, irrespective of the high-frequency range [39,68,74]. The ballast and the subgrade have also been modelled as an elastic or visco-elastic half-space in the investigation of ground-borne vibration, which is capable of representing the performance of the ballast and subgrade less than 500 *Hz* [89]. Such models, however, neglect the shear effects between the ballasts. Alternatively, Sato [90] and Zhai *et al.* [91, 92] proposed a more comprehensive model to consider the shear effects between the ballasts using shear springs and dampers between the ballasts. The validity of the ballast model was further demonstrated by comparing the ballast acceleration response obtained from the proposed model with that acquired from the field test measurements.

Slab track models: Slab track is widely adopted in the railway industry because of its relatively lower maintenance demands, especially in the high-speed railway lines [93]. The most well-known slab tracks are the Shinkansen slab track (Japan), Rheda slab track (Germany), Stedef slab track (France), Walo slab track (Switzerland) and Edilon block track (Netherlands) [93]. Fig.1.3 illustrates the Shinkansen slab track, which consists of a sub-layer stabilized using cement, cylindrical stoppers to prevent lateral and longitudinal motions, reinforced pre-stressed concrete slab and a CAM (Cement Asphalt Mortar) layer under the slab [93]. In the reported dynamic models, the track slab is usually described using the finite element methods, while the modal superposition method is adopted to calculate dynamic responses of the track slab to moving wheel's loads [87]. The CAM layer is modelled as the spring-damper elements under the track slab. Using the multibody dynamic model of a rail vehicle together with a flexible track model, Blanco *et al.* [94] compared the influences of different slab and ballasted tracks on the wheel/rail interactions. The study concluded that the slab track models yield higher wheel-rail contact force and show more prominent sleeper passing impacts comparing to those on the ballasted track model due to the relatively higher support stiffness.
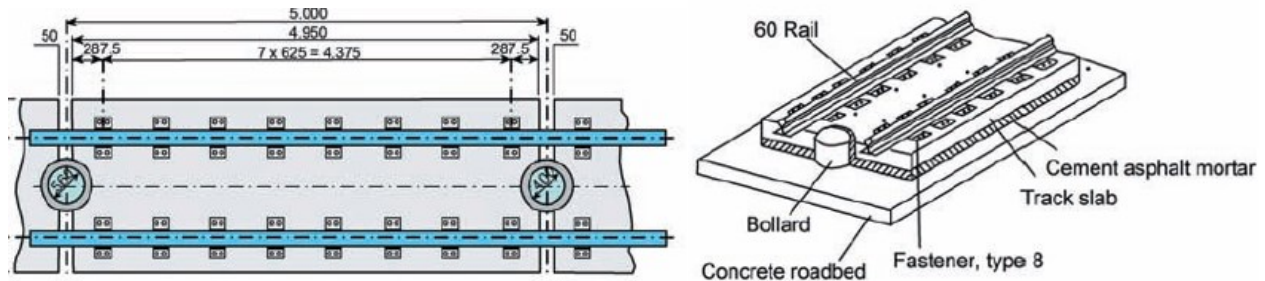
Figure 1.3: Shinkansen slab track [93].

1.2.2.2 Vehicle dynamic models

During the past few decades, a large number of models of the vehicle system have been reported to study the effects of wheel defects on the vehicle and the track system. High magnitude impact forces in the presence of wheel defects, however, cause high-frequency vibration, which must be taken into consideration in developing the simulation models. The local defects such as flats, spalling and shelling can lead to excitations near fundamental frequency corresponding to wheel rotation, while the wheel corrugation and the wheel polygonalization usually generate disturbance at much higher frequencies up to 1000 *Hz* [1]. Therefore, the frequency range of interest should be a key consideration when a model is developed for such studies.

A typical rail vehicle system consists of the car body, bogie frame, wheelset, as well as primary and secondary suspensions. The car body rests on two bogies, while each bogie contains two wheelsets. The spring and damping elements connecting the bogie frame and the wheelsets are referred to as the primary suspension. The secondary suspension is employed between the car body and the bogie frame, which may have widely different configurations. Depending on the specific objectives, the vehicle model can be formulated using different approaches such as rigid or elastic multibody models [95]. The rigid multibody model is considered adequate for the ride comfort, running stability and safety analyses, where the frequency range of interest is generally below 50 *Hz* [80]. The elastic multibody model, on the other hand, is better suited for structural vibration and fatigue analysis, where the frequency range of interest may be up to 1500 *Hz* [80]. Popp *et al.* [95] presented a detailed overview of the vehicle/track dynamics in the mid-frequency range (50 ~ 500 *Hz*). The modelling of vehicle/track interaction at high frequencies, up to 5000 *Hz*, was presented by Knothe and Grassie [45,80,96].

In an elastic multibody model of the vehicle/track system, some of the subsystems are modeled as flexible bodies using the modal approach. A general method for modelling and analysis

of flexible bodies using finite element technique was presented by Guyuan [97], which has been used to formulate the modal matrix in a standard data format [45]. Carlbom [98] discussed the modelling of a flexible car body in rail vehicles, and proposed four different criterion to select eigenmodes, namely, the modal participation, excitation spectra, modal contribution factors and comfort filters. The validation of the flexible car body in the vehicle dynamic model was demonstrated by Stribersky [99] using the experimental results. The modelling and applications of flexible bogie frame were presented by Claus and Schiehlen [97], which suggested that the structural vibrations of the bogie frame could be excited by the track irregularities. Dietz *et al.* [100] employed the flexible bogie frame coupled to the multibody dynamic model of the vehicle together with the nonlinear wheel/rail contact model for predicting fatigue life of the bogie frame under dynamic loads. Baeza *et al.* [101,102] developed a rotating flexible wheelset model with Eulerian modal coordinates, and predicted the development of corrugation on the rail. Other relevant investigations using the flexible wheelset can be found in [103,104].

The vehicle system dynamic models can also be categorized into three groups on the basis of model dimensions, namely, the one-, two- and three-dimensional models. One-dimensional models have been developed to study dynamic responses of a single wheel subject to static load of the car body and the bogie frame. The contact between the wheel and the rail is considered via either a linear or a non-linear spring. Such simple models are considered adequate for the analysis of high-frequency dynamic interactions between the wheel and the rail induced by a wheel defect [44,50,105,106]. Such a model, however, is limited only to vertical motion of the wheel induced by the wheel/rail forces

A number of two-dimensional vehicle models have been formulated to describe the car or wheelset dynamic responses in either the pitch-plane or the roll-plane. The simplest pitch-plane vehicle model consists of two wheels coupled to one bogie frame through the primary suspension with a car body loaded at the center of the bogie frame [36,38,107]. Half car body models have also been considered to study vertical and pitch responses of the car body and the bogie due to wheel/rail forces [108,109]. A typical half-car model is a 10-DOF pitch-plane vehicle model, which includes the vertical and pitch motions of the car body and the two bogies attached to the two ends of the car, as well as vertical motion of each of the four wheelsets. Such a model has been widely used to investigate dynamic responses of a rail vehicle due to the wheel/rail impact loads in the presence of the wheel and rail defects [64,92,108,109,110]. Considering that the vehicle pitch

mostly occurs at low frequencies, a quarter-vehicle pitch plane model may also be sufficient for the analysis of wheel/rail interactions in the presence of the wheel and rail defects, while the 10-DOF pitch-plane vehicle model is more suited for analyzing pitch motions of the car body and effects of defects in multiple wheels of a car.

Two-dimensional models of the vehicle in the roll-plane have also been developed in order to incorporate the complex wheel-rail geometry effects. Such models consist of a wheelset coupled to a bogie via the primary suspension and the car body resting on the bogie frame through the secondary suspension [111]. Each component in the roll plane model is described by its lateral, vertical and roll DOF. Since the lateral motion of the wheelset is coupled with the roll motion, the contact geometry relationships between the wheel and rail are incorporated for analyses of the vertical and lateral dynamic responses of the vehicle system.

A number of linear and nonlinear three-dimensional models of the rail vehicle system have also been developed for comprehensive analyses of the wheelset, bogie and car body responses, and interactions among the various components [88,91,112,113]. Such models incorporate the wheel/rail contact and geometric nonlinearities together with coupled longitudinal, vertical, lateral, yaw, pitch and roll motions of the wheelsets, and other components. Such models have been widely used for analyses of ride comfort [99], and stability and curving performance [88]. Considering the nonlinearities of the wheel/rail contact geometry and yaw dampers in a high-speed rail vehicle dynamic model, Huang *et al.* [114] studied the effects of vehicle suspension parameters and equivalent conicity of the wheel/rail on the low-frequency carbody hunting motion. The study concluded that higher stiffness of the secondary suspension poses greater potential risk of the carbody hunting motion, which affects ride comfort of the passengers. A number of investigations also employed nonlinear three-dimensional dynamic models to study bogie hunting under high-speed operations considering strong nonlinearities in the wheel/rail contact [115,116,117]. These have, invariably, shown strong effects of nonlinearities in the wheel/rail contact geometry on stability of the rail vehicle.

1.2.2.3 Wheel/rail contact models

An accurate wheel/rail contact model is most critical for the study of vehicle/track interactions, which directly determine the dynamic performance of the vehicle and track systems. The contact model provides estimations of the normal and tangential forces developed at the wheel/rail contact. Kalker [118,119] reviewed the developments in wheel/rail rolling contact theory. The continuum

rolling contact theory of the wheel/rail interface was initiated by Carter [120] in 1926, in which the wheel and rail were represented as a cylinder and an infinite half space, respectively. In the theory, the wheel/rail rolling contact was treated in two dimensions. Subsequently, de Parter and Johnson [103] proposed the widely used Hertz solution for the wheel/rail contact to predict the shape and size of contact area and the normal pressure. The theory also served as the basis for the more generalized wheel/rail creepage formulae.

In 1967 Kalker [119] proposed a linear creep theory assuming small creepage based on the Carter's formula, which has been widely adopted for dynamic analyses of railway vehicles, especially for the linear models [121,122]. A comprehensive nonlinear wheel/rail rolling contact theory was further established by Kalker [119], which served as the basis for developing the CONTACT algorithm. Although the CONTACT is considered reliable for predicting wheel/rail contact forces, it is difficult to use in real time simulations due to excessive computational demands [118]. Consequently, simplified creep theories, developed by Vermeulen and Johnson [123], have been used for developing accurate but simpler prediction models. Shen *et al.* [104] employed this theory and illustrated its validity considering small spin and unrestricted creepage. Kalker [124] further developed a simplified Hertzian contact model, which evolved into a computationally efficient FASTSIM algorithm. The FASTSIM is about 400 times faster than the CONTACT algorithm but about 100 times slower than that proposed by Shen [119]. Owing to its accurate prediction ability for the contact patch geometry and forces, the FASTSIM algorithm is most widely used in many commercial railway dynamics simulation platforms such as SIMPACK, UM, ADAMS and NUCARS [125,126,127,128].

The Hertzian contact spring has been widely employed to evaluate the wheel/rail normal forces [39,129]. A linearized contact spring is often used to represent the wheel/rail contact for relatively small wheel and rail deformations. Grassie [45,96] and Sato [130] used the linear spring contact model to study influences of the rail corrugation and wheel defects. The linearized contact spring, however, may overestimate the wheel/rail impact forces, especially in the case of wheel/rail defects [131]. Alternatively, a number of non-Hertzian contact models have been proposed, where the contact is described in either two- or three-dimensions [108]. Pieringer *et al.* [132,133] used the two- (2D) and three-dimensional (3D) non-Hertzian contact models to investigate wheel/rail interactions due to wheel flats, and concluded that a 2D model yields an overestimation of the contact force compared to the 3D model. More significant differences in the contact forces obtained

from the 3D and 2D models were especially observed at higher frequencies (above 2 *kHz*). The wheel/rail contact in such models is generally described by either a point-contact or distributed over a very small contact area, which may contribute to the overestimation of peak impact forces. Dong *et al.* [36,40] developed an adaptive wheel-rail contact model, in which the wheel/rail interaction is presented by a set of uniformly distributed spring elements with equal stiffness. Alternatively, Zhu *et al.* [134] proposed a modified adaptive wheel-rail contact model, comprising continuous radially-distributed spring elements within the contact patch that can account for asymmetry of the patch as the defects enter and exit the contact region. The study concluded that the adaptive wheel-rail contact model could provide a more accurate prediction of the impact force due to wheel flats over a wide speed range.

1.2.3 Wheel/rail wear model

The railway wheels are invariably subjected to wear owing to either the wheel tread-braking block interactions or the wheel-rail interactions. The wheel tread wear contributes to alternation of the transverse as well as circumferential profile of the wheel, and thereby affects dynamic performance of the vehicle system. A comprehensive review of the wheel wear was reported by Tunna *et al.* [135], which focused on the loading environment, wheel materials, wheel wear and wheel rolling contact fatigue. A number of wear mechanisms have been used to describe the railway wheel wear, such as delamination wear, oxidation or corrosive wear, abrasive wear and adhesive wear [136]. Bolton *et al.* [137] classified the wear into three different wear regimes: mild wear, severe wear, and catastrophic wear, through experimental investigations. The mild wear was mainly attributed to oxidation and abrasion of the wheel material. The mild delamination of oxide layers contributed to material removal leading to severe wear, whereas the subsequent delamination lead to catastrophic wear regime [138]. A vast number of wear models have been formulated to quantify the material removal attributed to different wear processes. Meng *et al.* [139] reviewed more than 180 wear models developed for different applications. In the wheel-rail contact, the Archard wear model and the dissipated energy- based wear model are commonly used in the wear prediction of the wheel and rail [140]. Johansson [141] compared the predictions from the Archard wear and the energy- based wear models for a given reference case, and concluded that both wear models yield similar wear distribution on the wheel circumference.

The wear prediction usually involves a long-term wear accumulation process. The wear prediction models thus generally integrate the wear model with a long-term iteration scheme

[25,142]. In such models, the coupled vehicle and track dynamic model is usually employed to calculate the dynamic responses at the wheel-rail interface, which further serve as inputs to the wear model to determine the wheel wear in the short term. The wear response is used to update the wheel profile either in the transverse or in the circumferential direction. The updated wheel profile is subsequently returned to the vehicle/track dynamic model to determine the resulting response in the subsequent iteration step, and accumulated wear. Such long-term wear iteration models have been widely used for predicting transverse profile of the wheel [143,144,145,146] and rail [147,148,149], wheel polygonalization [24,25,26,28,27,44] and rail corrugation [150,151,152]. The models, however, may result in large accumulation errors in wear prediction results due to the large number of iterations. The iteration based wear prediction model is thus needed to be further tuned on the basis of the wear measurements. Considerable efforts have been made to improve the accuracy of the wear models in predicting transverse profiles of the wheel and the rail. The rail corrugation and wheel polygonalization, however, are regarded as the abnormal wear patterns at the wheel-rail interface. The wear models used for predicting the rail corrugation and wheel polygonalization have not yet been proven since the growth rate is of greater concern rather than the wear amplitude.

1.3 Scope and objective of the dissertation research

From the review of reported studies, it is evident that the effects of wheel defects on dynamic responses of the bogie and the car have been widely investigated. The studies, however, are mostly limited to relatively low speeds, especially for the wheel flats. Many knowledge gaps exist on the impacts of wheel defects, particularly in case of high order wheel polygonalization during high-speed operations. Owing to the highly adverse influences of high order wheel polygonalization, it is vital to investigate the resulting influences and the formation mechanisms of high order wheel polygonalization theoretically and experimentally so as to identify possible countermeasures for safe and efficient operations of high speed railways.

The primary objective of this dissertation research is formulated to conduct theoretical and experimental studies to contribute to the knowledge on evolution of high-order wheel polygonalization, and its effects on the operational performance of the vehicle and the vehicle components. The dissertation research is particularly focused on a long-term field study on characterization and growth rate of polygonal wheel wear, and development of a comprehensive coupled vehicle/track dynamic model to investigate (i) response characteristics of the vehicle/track

system under excitations arising from the interactions of the polygonal wheel with the rail and (ii) to identify the main contributors of high order wheel polygonalization via a long-term wear iteration model. The specific goals are summarized below:

a) Develop a coupled vehicle/track dynamic model considering the flexibility of the wheelset and the slab track, and demonstrate its validity using the available measured data;

b) Investigate dynamic responses of the vehicle/track system, namely, the wheel/rail contact forces, axle box acceleration and bending stress of the wheelset axle considering different vehicle speeds under discrete wheel defects as well as different patterns of continuous wheel defects (polygonal wear);

c) Characterize patterns (orders) of wheel polygonalization and rate of growth of wear through a long-term field test program, and explore correlations between the axle box acceleration and the order and amplitude of the polygonal wear;

d) Develop a long-term wear iteration model and investigate the evolution of wheel polygonalization considering different vehicle and track parameters, and identify primary causal factors leading to high order wheel polygonalization.

1.4 Organization of the dissertation

This dissertation is prepared according to the manuscript-based format described in "Thesis Preparation, Examination Procedures and Regulations" guidelines of the School of Graduate Studies, Concordia University. This dissertation research is organized in 6 chapters, which address the research goals stated in section 1.3, including the Introduction and Literature Review chapter (Chapter 1), and the concluding chapter (Chapter 6). The first chapter presents the review of relevant studies reporting wheel defects, modelling of vehicle/track dynamic system and wear models, in order to build the essential knowledge of methods and scope of the study. In Chapter 2, a coupled vehicle/track dynamic model is formulated considering the flexibility of wheelset, rail and the slab (goal a). Chapter 3 presents an investigation of dynamic responses of a high-speed rail car under excitations arising from the high order wheel polygonalization (goal b). Chapter 4 presents a long-term field test program for characterizing the wheel wear, and its progression to high-order wheel polygonalization in addition to vibration response of the axle box. The data are analyzed to illustrate relationships among the mileage, wheel wear amplitude and the axle box acceleration (goal c). Chapter 5 presents a long-term wear iteration model to investigate the

evolution of wheel polygonalization considering different vehicle and track parameters to identify the primary causal factors of high order wheel polygonalization (goal d).

Chapters 2 to 5 are compiled from 4 different manuscripts, which have been either published or submitted for possible publication in international peer-review journals. The references in each chapter are reorganized so as to eliminate duplications. Furthermore, the 'Introduction' sections in Chapters 2 to 4 have been condensed, since a more comprehensive review of relevant studies has been presented in Chapter 1. The highlights of the manuscripts are further summarized below:

Chapter 2 presents the following paper published in the *Journal of Rail and Rapid Transit*: Wu, X., Rakheja, S., *et al.* (2017). Influence of a flexible wheelset on the dynamic responses of a high-speed railway car due to a wheel flat. *Journal of Rail and Rapid Transit, 0954409717708895.*

Large magnitude impact loads caused by wheel flats may excite various vibration modes of the wheelsets employed in high-speed trains and thereby contribute considerably to dynamic response of the vehicle. In this study, the wheelset and the track slab are modeled as flexible bodies, and integrated to a multi-body dynamic model of the high-speed train using the modal approach. The multi-body dynamic model is formulated for a typical high-speed train consisting of a car body, two bogie frames and four wheelsets. The track is modeled considering the rail as a Timoshenko beam discretely supported on a flexible track slab. The effects of wheelset flexibility on the dynamic response are illustrated through comparisons with those obtained with a rigid wheelset considering different vehicle speeds and sizes of a discrete wheel defect (wheel flat). Subsequently, the effects of a wheel flat, characterized by a haversine function, on the vehicle/track system are evaluated in terms of wheel-rail impact forces, axle-box vertical acceleration and dynamic stress developed in the wheelset. The results suggested that the wheelset flexibility can lead to significantly higher axle-box vibration and wheelset axle stress compared to a rigid wheelset in the presence of a wheel flat.

Chapter 3 presents the following paper that has been accepted for publication in the *Vehicle System Dynamics Journal*.
Wu, X., Rakheja, S., *et al.* (2017) Dynamic responses of a high-speed railway car due to wheel polygonalization. *Vehicle Systems Dynamics* (Accepted: 28 January 2018)

The paper investigates the effects of different orders of wheel polygonalization on the dynamic responses of a high-speed rail vehicle through simulations of the coupled vehicle/track dynamic model, described in Chapter 2. A field-test program was undertaken to acquire the polygonal wheel

wear profiles and the axle box acceleration response of a high-speed train. The data are used to demonstrate validity of the coupled vehicle/track system model. Subsequently, the effects of wheel polygonalization are evaluated in terms of wheel-rail impact forces, axle-box vertical acceleration and dynamic stress developed in the axle considering different amplitudes and harmonic orders of the polygonal wear. The results suggested that the high-order wheel polygonalization can give rise to high frequency impact loads at the wheel/rail interface, and excite some of the vibration modes of the wheelset and the axle box leading to high magnitude axle box acceleration and the dynamic stress in the wheelset axle.

Chapter 4 presents the following paper has been reviewed for publication in the *Vehicle System Dynamics Journal.* The manuscript required revisions of minor nature and a revised manuscript has been submitted.

Wu, X., Rakheja, S., *et al.* (2017) A study of polygonal wheel wear through a field test program. *Vehicle Systems Dynamics* (submitted).

The paper describes a long-term field test program for establishing an understanding of growth in wheel polygonal wear. The data are analyzed to characterize the pattern of polygonal wear and its rate of growth in addition to its correlation with the axle box vibration response. The field measurements, conducted on a high-speed railway, involved monitoring of wheels profiles between successive re-profiling of the wheels so as to identify the rate of growth of wear in addition to the axle box acceleration. The data suggested rapid growth in wheel wear, which could be characterized by polygonal wear of nearly 18th and 19th harmonic order. It is further shown that the magnitude of axle box acceleration increased considerably with increasing wear magnitude of the wheel.

Chapter 5 presents the following paper that has been submitted for publication in the Wear Journal.

Wu, X., Rakheja, S., *et al.* (2018) Investigation on the formation mechanism of wheel polygonalization using a long term wear model. *Wear* (submitted).

The paper presents a long term wear iterative scheme integrating the coupled vehicle/track dynamic model, presented in chapter 2, with an Archard sliding wear model. The model is formulated with a goal to identify primary contributors of high order wheel polygonalization, and to demonstrate the growth in polygonal wear of the wheels over a relative long service period. The effects of different vehicle and track parameters on the wear propagations are investigated, which

include flexibility of the wheelset and the rail, vehicle speed, wheelbase, and rail pad stiffness and damping. The localized bending vibration mode of the rail section between the two wheelsets of the bogie, regarded as three half wavelength bending vibration mode (near 650 Hz), is identified as the primary contributor to high magnitude wheel/rail contact forces in the 500 ~ 700 Hz frequency range. This constitutes spatial dynamic loading of the wheelset and other vehicle components, which is shown to be the primary causal factor leading to the formation of high order wheel polygonalization. The results suggested that the wheelset flexibility can accelerate the wear at the wheel-rail interface, which more likely contribute to formation of low order wheel polygonalization. Increasing the support stiffness of the rail pad intensified the wheel/rail coupled vibration, which may also lead to the lower order wheel polygonalization. The formation of high order wheel polygonalization, however, could be greatly suppressed by increasing effective damping of the rail pads. It is suggested that eliminating the initial wheel irregularities can slow the formation of polygonal wear, and frequent variations in the operating speed and operating railway line could help eliminate the spatial nature of the contact forces and thereby mitigate formation or growth in high-order wheel polygonalization.

CHAPTER 2: INFLUENCE OF A FLEXIBLE WHEELSET ON DYNAMIC RESPONSES OF A HIGH-SPEED RAILWAY CAR DUE TO A WHEEL FLAT

2.1 Introduction

The railway wheels are invariably subjected to the defects owing to the wear process and rolling contact fatigue of the wheel and the rail [1]. A detailed review of wheel defects including the known formation mechanism, effects and mitigation methods has been presented in the Chapter 1. The reported studies show substantially high impact loads at the wheel/rail interface due to the excitations arising from the wheel defects, which further impose highly adverse effects on the vehicle and the track subsystem [1,8,49,153]. These results, however, are limited to lower operating speeds, and many knowledge gaps exist on the impacts of wheel defects in high speed operations. This chapter presents a comprehensive coupled vehicle track dynamic model of a high speed rail car. Considering that large magnitude impact loads caused by wheel defects may excite various vibration modes of vehicle and track subsystems, the wheelset is modeled as a flexible body. The modal approach is used to incorporate the effect of wheelset flexibility in the multi-body dynamic model of a high-speed train car, which is also coupled with a flexible track slab model via the modal method. The multi-body dynamic model is formulated for a typical high-speed train consisting of a car body, two bogie frames and four wheelsets. The track is modeled considering the rail as a Timoshenko beam discretely supported on a flexible track slab. The validity of the model is demonstrated by comparing the wheel/rail impact forces due to a haversine flat with the measured data reported by Fermer and Neilsen [49,153]. The dynamic stress of the axle shaft obtained from the flexible wheelset model is further compared with the results obtained from the finite element analysis of the wheelset.

Using this model, the effects of wheelset flexibility on the dynamic responses are illustrated through comparisons with those obtained with a rigid wheelset considering different vehicle speeds and sizes of the wheel flat. Subsequently, the effects of wheel flats on the vehicle/track system are evaluated in terms of wheel-rail impact forces, axle-box vertical acceleration and dynamic stress developed in the wheelset due to a haversine wheel flat.

2.2 Wheelset-vehicle-track model formulations

A comprehensive model of a high-speed vehicle/track system is formulated through integration of three component models. These included models of flexible wheelsets, a flexible slab track and the vehicle. Figure 2.1 illustrates the simulation scheme comprising finite element (FE) models of the flexible wheelset and the slab-track coupled with the vehicle model in the SIMPACK platform [125]. The FE model of the wheelset is used to determine its modal properties via the eigen-analysis. The modal vectors are subsequently integrated to the vehicle model using the FEMBS (Finite Element Multibody Systems) interface available in SIMPACK [125]. The resulting dynamic forces developed at the wheel/rail interface are obtained to serve as excitations to the slab track model to evaluate deflection response of the rail. The rail deflection response is subsequently integrated to the vehicle model using the SIMAT (SIMPACK-MATLAB) co-simulation interface, as shown in Fig.2.1, to study its dynamic responses in the presence of a wheel flat. The component models' formulations are described in the following subsections.
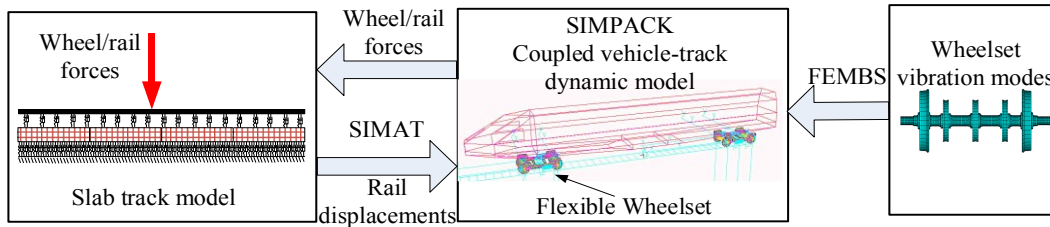
Figure 2.1: Wheelset-vehicle-track dynamic system model.

2.2.1 Flexible wheelset model

In the presence of a wheel flat, the forces developed at the wheel/rail interface and the resulting wheelset deformations constitute a close-loop process. The wheel flat- induced forces may contribute to elastic deformation and acceleration response of the wheelset, which could subsequently alter the characteristics of the wheel/rail contact force. The rotating wheelset is thus modeled as a flexible body to determine its dynamic deformations and the resulting wheel/rail contact force responses. In the model, a fixed reference frame, located at the mass center of the rotating wheelset, is used to describe its translational and rotational motions, as shown in Figure 2.2(a). The elastic deformations of the wheelset due to the external forces arising from the wheel/rail contact and the primary suspension are defined with respect to this frame, as shown in Figure 2.2(b), such that:

$$\mathbf{d}(\mathbf{c},\ t)=\mathbf{c}+ \mathbf{u}(\mathbf{c},\ t) \tag{1}$$

where vector **d** describes the displacement response at a point in the wheelset with respect to the reference frame, **c** is the position vector of the same point in the undeformed state and **u** is time-varying dynamic displacement vector at the same location, as shown in Fig.2.2(b). The dynamic deformation of the wheelset $\mathbf{u}(\mathbf{c}, t)$, is obtained using the mode superposition approach [154]:

$$\mathbf{u}(\mathbf{c},\ t) = \mathbf{\Phi}\ \mathbf{q}_w(t) \tag{2}$$

where $\mathbf{q}_w(t)$ denotes the generalized coordinate vector, and $\mathbf{\Phi}$ is the modal matrix of the wheelset. In this study, a finite element (FE) model of the flexible wheelset is formulated to determine the modal matrix $\mathbf{\Phi}$. The model is developed in the ANSYS platform using 43764 Solid 45 elements (Figure 2.2). The modal vectors of the wheelset are obtained from the eigen-analysis. Considering that the high impact loads can excite a number of high frequency modes of the wheelset, a total of 58 vibration modes occurring at frequencies up to 2533 *Hz* are considered to determine the wheelset response.
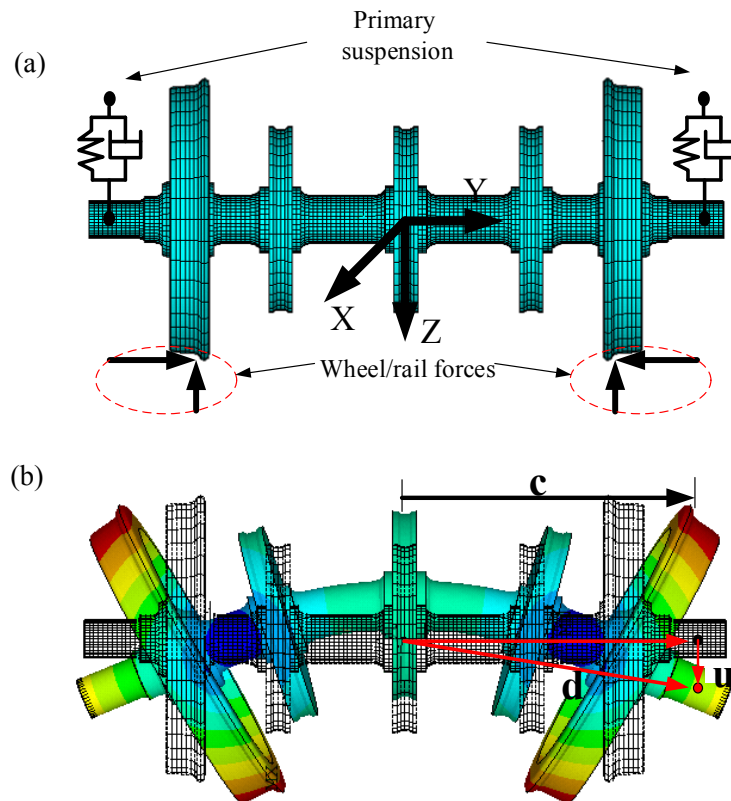
Figure 2.2: Modelling of a flexible wheelset.

The modal matrix is integrated into the car model in the SIMPACK platform via the FEMBS interface [125], which is subsequently used to determine the deflection responses of the wheelset. The computational method also incorporates the force and moments arising from the primary suspension and the wheel/rail contact (Fig. 2.2). The stress vector $\boldsymbol{\sigma}$ at a point in the wheelset axle can be obtained from wheelset deformations using the modal stress recovery approach [155], such that:

$$\boldsymbol{\sigma} = \mathbf{D}\boldsymbol{\varepsilon} = \mathbf{DL}\boldsymbol{\Phi}\mathbf{q} \tag{5}$$

where $\mathbf{D}$ is the elasticity matrix, and $\mathbf{L}$ is the linear operator relating to strain $\boldsymbol{\varepsilon}$ and displacement $\boldsymbol{u}$.

2.2.2 Slab track model

The track model integrates the models of the rails and the track slab supported on the cement asphalt mortar (CAM) layer, as shown in Figure 2.3(a). The rails are supported on the slab via the fasteners, which are represented by discrete spring-damping elements. The formulations of the rail and slab models are described in the following sub-sections.

2.2.2.1 Rail model

The rail is represented by a finite length continuous Timoshenko beam discretely supported on the slab via fasteners and rail pads. The model is formulated for the 100 m rail with the sleeper bay of 0.6 m, which is considered to represent characteristics of the infinite length rail with reasonable accuracy and computational efficiency [110]. Both ends of the rail are assumed to be fixed, while each rail is subject to moving loads attributed to the contact forces at each wheel/rail interface $\mathbf{F}_{wri}$ (i=1, 2, 3, 4), as shown in Figure 2.3(b). The lateral and vertical forces due to discrete supports are represented as $\mathbf{F}_{syi}$ and $\mathbf{F}_{szi}$(i=1,.., N_s), where N_s is the number of supports. The figure also illustrates the moments caused by the wheel/rail contact forces, $\mathbf{M}_{Gi}$ (i=1, 2, 3, 4) and the support forces, $\mathbf{M}_{si}$ (i=1, 2, 3, N_s), which are taken about the center of rail. x_{Gi} (i=1, 2, 3, 4) defines position of each wheel along the rail, and x_{si} is position of the ith discrete support along the rail.

The governing equations describing the vertical z and bending ψ_y deflections of the rail subjected to vertical wheel/rail contact F_{wrzj} and support F_{szi} forces are obtained as [156]:

$$m\frac{\partial^2 z(x,t)}{\partial t^2} + \kappa_z GA\left[\frac{\partial \psi_y(x,t)}{\partial x} - \frac{\partial^2 z(x,t)}{\partial x^2}\right] = -\sum_{i=1}^{N_s} F_{szi}\delta(x-x_{si}) + \sum_{j=1}^{N_w} F_{wrzj}\delta(x-x_{wj}) \tag{6}$$
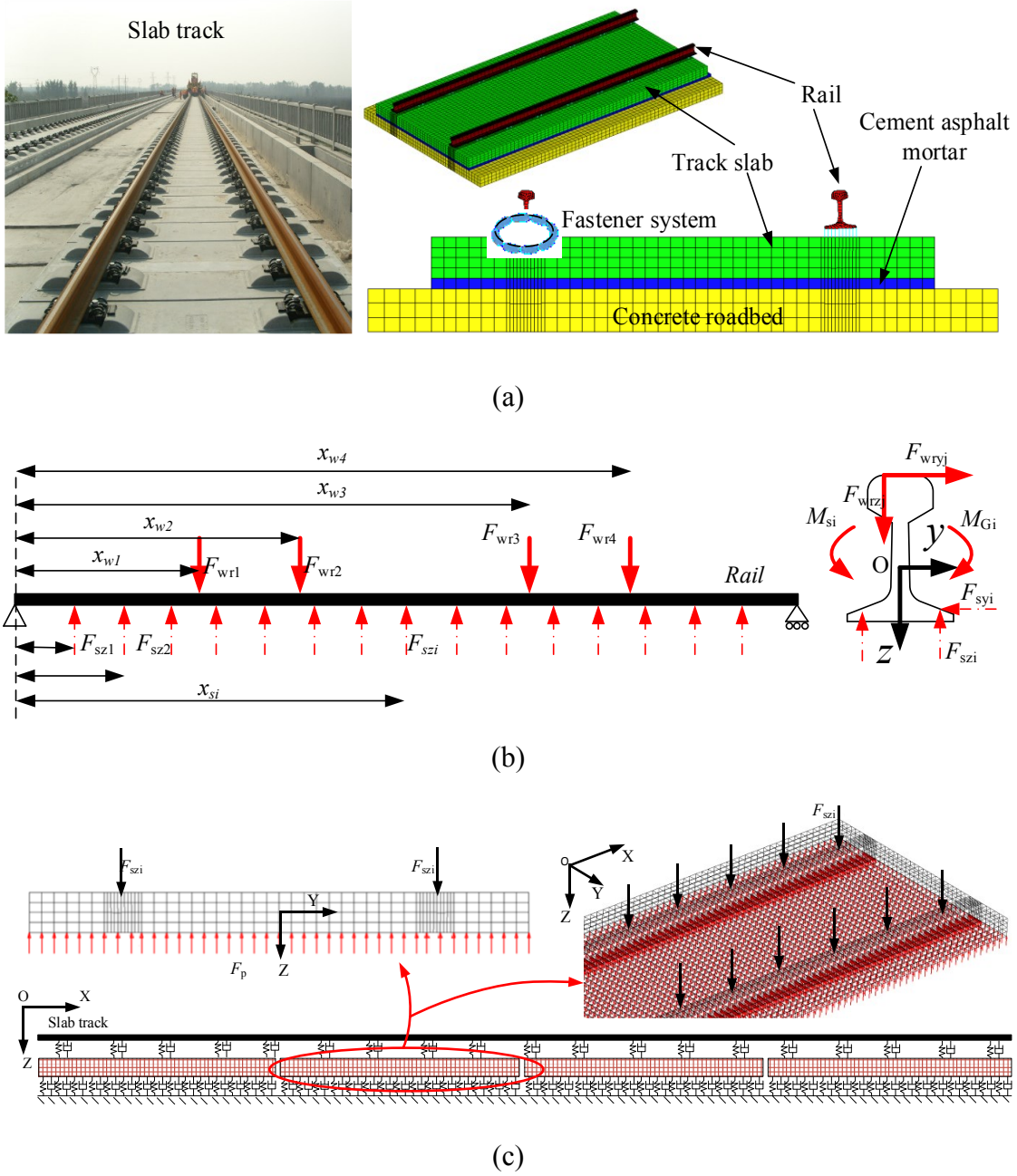
Figure 2.3: (a) Slab track system; (b) the rail model; and (c) track slab model.

$$\rho I_y \frac{\partial^2 \psi_y(x,t)}{\partial t^2} + \kappa_z GA\left[\psi_y(x,t) - \frac{\partial z(x,t)}{\partial x}\right] - EI_y \frac{\partial^2 \psi_y(x,t)}{\partial x^2} = 0 \qquad (7)$$

where m is mass of the rail per unit length, ρ is mass density, A is rail cross section area, G is shear modulus, E is Young's modulus and I_y is second moment of area of the rail cross section about the

y-axis. In the above equations, κ_z is vertical shear coefficient, $\delta(x)$ is Dirac delta function, and N_w is the number of wheelsets considered in the model.

Similarly, the governing equations for the lateral y and yaw ψ_z deflections of the rail are formulated considering lateral forces due to wheel/rail contact F_{wryj} and the supports F_{syi} :

$$m\frac{\partial^2 y(x,t)}{\partial t^2} + \kappa_y GA\left[\frac{\partial \psi_z(x,t)}{\partial x} - \frac{\partial^2 y(x,t)}{\partial x^2}\right] = -\sum_{i=1}^{N_s} F_{syi}\delta(x-x_{si}) + \sum_{j=1}^{N_w} F_{wryj}\delta(x-x_{wj}) \qquad (8)$$

$$\rho I_z \frac{\partial^2 \psi_z(x,t)}{\partial t^2} + \kappa_y GA\left[\psi_z(x,t) - \frac{\partial y(x,t)}{\partial x}\right] - EI_z \frac{\partial^2 \psi_z(x,t)}{\partial x^2} = 0 \qquad (9)$$

where I_z is the second moment of area of the rail cross-section about the z-axis, and κ_y is the lateral shear coefficient.

The equation of motion describing the torsional deflection ψ_x of the rail subjected to wheel/rail and support forces is formulated as:

$$\rho I_0 \frac{\partial^2 \psi_x(x,t)}{\partial t^2} + \kappa_x \frac{\partial^2 \psi_x(x,t)}{\partial x^2} = -\sum_{i=1}^{N_s} M_{si}\delta(x-x_{si}) + \sum_{j=1}^{N_w} M_{Gj}\delta(x-x_{wj}) \qquad (10)$$

where I_0 is the polar moment of inertia of the rail cross-section and κ_x is the torsional stiffness coefficient.

The above governing partial differential equations describing the deflections of the rail can be converted to a series of ordinary differential equations using the modal superposition method in terms of generalized coordinates as [48]:

$$z(x,t) = \sum_{k=1}^{N_z} Z_k(x)q_{zk}(t); \quad y(x,t) = \sum_{k=1}^{N_y} Y_k(x)q_{yk}(t); \quad \psi_x(x,t) = \sum_{k=1}^{N_\phi} \Phi_k(x)q_{Tk}(t)$$

$$\psi_y(x,t) = \sum_{k=1}^{N_{\psi y}} \Psi_{yk}(x)\omega_{yk}(t); \quad \psi_z(x,t) = \sum_{k=1}^{N_{\psi z}} \Psi_{zk}(x)\omega_{zk}(t) \qquad (11)$$

where $q_{zk}(t)$, $\omega_{yk}(t)$, $q_{yk}(t)$, $\omega_{zk}(t)$ and $q_{Tk}(t)$ are the generalized modal coordinates, and $Z_k(x), \Psi_{yk}(x)$, $Y_k(x)$, $\Psi_{zk}(x)$ and $\Phi_k(x)$ are the mode shape functions of the rail. N in the above formulation relates to the number of modes considered for each coordinate, which is denoted in the subscript.

Upon substituting the above relations in the governing equations of motion, (6) to (10), and applying the normalized mode shape functions of the rails, the partial differential equations of the rail are converted to a set of ordinary differential equations, such that:

$$\ddot{\quad} \qquad \frac{c_z \mathrm{GA}}{m}\left(\frac{k\pi}{l}\right)^2 q_{zk}(t) + \kappa_z \mathrm{GA}\frac{k\pi}{l}\sqrt{\frac{1}{m\rho I_y}}\omega_{yk}(t) = -\sum_{i=1}^{N_s} F_{szi}Z_k(x_{si}) + \sum_{j=1}^{N_w} F_{wrzj}Z_k(x_{wj})$$

$$\ddot{\quad} \qquad \left[\frac{\kappa_z \mathrm{GA}}{\rho I_y} + \frac{\mathrm{EI}_y}{\rho I_y}\left(\frac{k\pi}{l}\right)^2\right]\omega_{yk}(t) - \kappa_z \mathrm{GA}\frac{k\pi}{l}\sqrt{\frac{1}{m\rho I_y}}q_{zk}(t) = 0$$

$$\ddot{\quad} \qquad \frac{c_y \mathrm{GA}}{m}\left(\frac{k\pi}{l}\right)^2 q_{yk}(t) + \kappa_y \mathrm{GA}\frac{k\pi}{l}\sqrt{\frac{1}{m\rho I_y}}\omega_{zk}(t) = -\sum_{i=1}^{N_s} F_{syi}Y_k(x_{si}) + \sum_{j=1}^{N_w} F_{wryj}Y_k(x_{wj})$$

$$\ddot{\quad} \qquad \left[\frac{\kappa_y \mathrm{GA}}{\rho I_z} + \frac{\mathrm{EI}_z}{\rho I_z}\left(\frac{k\pi}{l}\right)^2\right]\omega_{zk}(t) - \kappa_y \mathrm{GA}\frac{k\pi}{l}\sqrt{\frac{1}{m\rho I_z}}q_{yk}(t) = 0$$

$$\ddot{\quad} \qquad \frac{\kappa_x}{\rho I_0}\left(\frac{k\pi}{l}\right)^2 q_{Tk}(t) = -\sum_{i=1}^{N_s} M_{si}\Phi_k(x_{si}) + \sum_{j=1}^{N_w} M_{Gj}\Phi_k(x_{wj}) \qquad (12)$$

The solutions of above equations together with the relation in (11) yield deflection responses of the rail. The rail deflection responses at the wheel/rail interfaces are applied to the wheelset model to determine the normal contact forces, F_{wri} ($i=1, 2, 3, 4$), using the Hertzian contact model available in the SIMPACK platform. For this purpose, the SIMAT co-simulation interface is used, as described in Figure 2.1.

2.2.2.2 Track slab model

The high magnitude impact forces induced by the wheel defects are transmitted to the slab track through the rail pads and the fasteners, which cause deflections of the slab primarily due to flexibility of the CAM layer. The flexibility of the slab may also contribute to its deflection, especially under high magnitude vertical forces caused by wheel flat. The bending deflections of the slab directly contribute to the rail deflections and thus the wheel/rail contact forces. The lateral deflection of the slab, however, is considered negligible compared to its vertical deflection.

A FE model of the flexible track slab is formulated considering vertical components of the forces due to discrete supports between the rails and the track slab F_{szi} together with vertical forces arising at the CAM-slab interface F_{pi}, as shown in Figure 2.3(c). The vertical deflection responses z_s of the slab subjected to these forces are evaluated from solutions of equations of motion of the track slab:

$$[M]\{\ddot{\quad} \quad \dot{\quad} \quad z_s\} = \mathbf{F}_{sz} + \mathbf{F}_p \qquad (17)$$

where $[M]$, $[C]$ and $[K]$ are the global mass, damping and stiffness matrices of FE model of the track slab, respectively. Modal superposition approach is employed to determine vertical deflection response at a given point in the slab assuming propositional damping, such that:

$$\{z_s\} = \sum_{i=1}^{N_m} \{\phi\}_i Z_i \tag{18}$$

where Z_i is the generalized modal coordinates vector corresponding to the ith mode, $\{\phi\}_i$ is the ith mode shape function of the track slab, and N_m is the total number of vibration modes considered in the slab model.

In this study, the FE model is formulated for a 100 m section of the track comprising various slab segments (6.5 m long×2.5 mm wide× 0.3 m) with free-free boundary conditions. The FE-model is formulated in ANSYS platform using Solid 45 elements, and each slab segment is discretized using 5070 elements. A total of 20 vibration modes of the track slab were considered with natural frequencies up to 382.9 Hz for analyzing deformation responses of the track slab. Figure 2.4 illustrates some of the vibration modes of a track slab segment. The first and secondary bending modes are observed at frequencies of 29 Hz and 79.6 Hz, respectively.
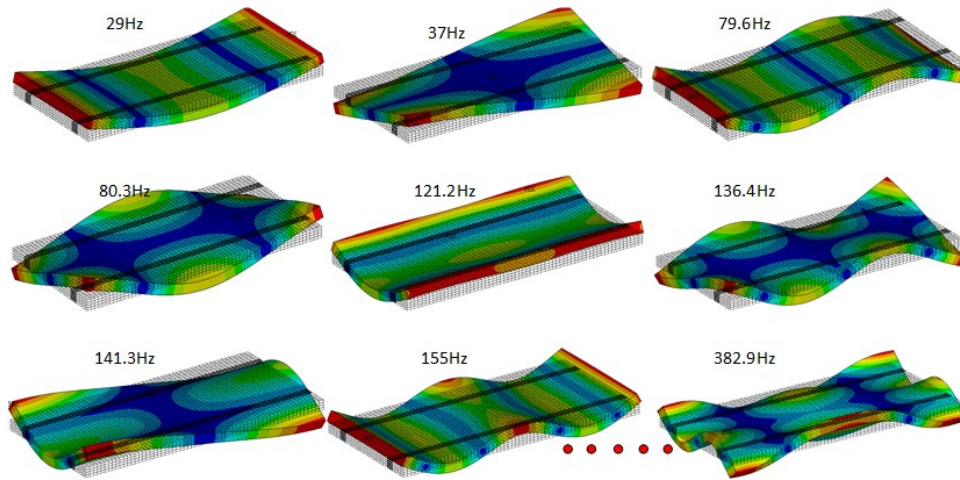
Figure 2. 4: Selected vibration modes of track slab

2.2.3 Vehicle model

A multibody dynamic model of a typical high-speed railway car is formulated in the SIMPACK platform. The model consists of a rigid car body supported on two rigid bogie frames via the secondary suspensions, and four flexible wheelsets coupled to the bogie through the primary suspensions. The model also incorporates two axle boxes on each wheelset, which are coupled to

the bogie frame via elastic mounts oriented along the longitudinal direction. The primary and secondary suspensions are modelled as parallel combinations of equivalent linear springs and viscos dampers along the three translational directions. A pictorial view of the bogie showing the primary suspension (coil spring and vertical damper) and secondary suspension (air springs, antiroll bar, and yaw, lateral, and vertical dampers), is presented in Fig.4.2. Both the car body and the bogie frames are modelled as rigid bodies with 6 degrees-of-freedom (DOF), while each axle box is permitted to pitch with respect to the wheelset to which it is attached. Each wheelset is considered as a rotating flexible body, whose deflection responses are obtained from modal superposition, as described in section 2.2.1.

2.2.4 Wheel/rail contact model

The vehicle and the track models (rail and slab) are coupled via the wheel/rail contact model. The lateral and longitudinal creep forces and the spin moments at each wheel/rail contact point are determined using the FASTSIM algorithm [124] considering the S1002CN wheel tread profile coupled with the Rail 60 profile. The normal forces developed at each wheel/rail interface are evaluated as a function of the wheel/rail overlap $\Delta z_i(t)$ in the vertical direction using the Hertzian contact theory [157], such that:

$$F_{wrzi} = C_H \left[\Delta z_i(t) \right]^{3/2}; \ i = 1, 2, 3, 4 \tag{19}$$

where C_H is the Hertzian contact coefficient. For a normal wheel, the wheel/rail overlap $\Delta z_i(t)$ can be directly obtained from vertical motion of the wheel z_{wi} with respect to the rail at the contact point $z(x_{wi},t)$, determined from (11) and the rail profile. The wheel displacement, in a similar manner, is determined from deflection responses of the flexible wheelset together with the wheel profile. In the presence of a wheel defect, the wheel/rail overlap is computed considering the geometry of the wheel defect, $r_i(t)$, in addition to the relative motion between the wheel and rail (Fig. 2.5(a)), such that:

$$\Delta z_i(t) = z_{wi}(t) - z(x_{wi},t) - r_i(t) \tag{20}$$

Assuming a haversine wheel flat, the wheel flat profile can be represented by a cosine function of the flat chord, as shown in Figure 2.5(a). The change in wheel radius $r_i(t)$ in the presence of a flat of depth D_{fi} and length L_{fi} is given by [2]:

$$r_i(t) = \frac{1}{2} D_{fi} \left[1 - \cos(2\pi x / L_{fi}) \right], D_{fi} = L_{fi}^2 / (16R) \tag{21}$$

where R is the wheel nominal radius. Figure 2.5(b) illustrates change in the wheel radius as a function of length of the wheel flat, as obtained from Equation (21).
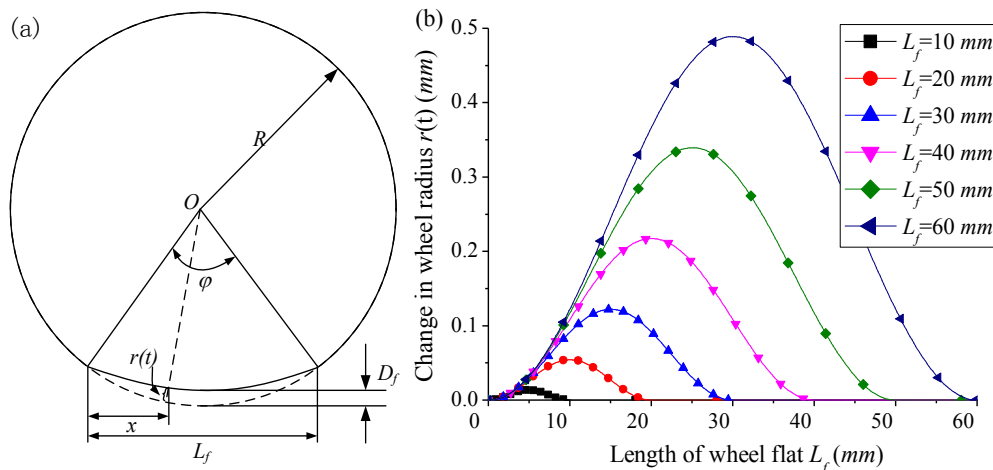
Figure 2.5: (a) Haversine wheel flat geometry; and (b) change in wheel radius as a function of the flat length.

2.3 Method of analysis and simulation strategy

In this study, the coupled vehicle/track dynamic model integrating the flexible wheelset and track models is employed to investigate the effects of wheelset flexibility on dynamic behaviors of a high-speed rail vehicle in the presence of a wheel flat. The modal matrix obtained for the free-free wheelset is modified to account for its couplings with the axle box and the primary suspension. For this purpose, the modal matrix obtained from FE model of the free-free wheelset is initially used to build the coupled wheelset-vehicle model, in the absence of the track model. The eigen-analysis of the coupled model is performed in SIMPACK software to derive the modified modal matrix of the wheelset subject to constraints due to axle box and primary suspension. This modified modal matrix is subsequently applied to the coupled vehicle-track-wheelset model to determine wheelset deflection and wheel-rail contact force responses.

The forces developed at the wheel/rail contact points are initially evaluated in the SIMPACK, and transferred to the flexible track model in the MATLAB via the SIMAT. The deflection responses of the rail due to the wheel/rail contact forces are determined from the flexible slab-track model during the same integration interval using the method described in section 2.2.2. The resulting deflection responses are subsequently transferred back to the vehicle model in SIMPACK via the SIMAT, as shown in Figure 2.1. This approach thus permits analyses of the effects of the constrained wheelset flexibility and wheel flats on dynamic behavior of the vehicle system.

The simulation of the coupled vehicle/track model are performed to determine responses in terms of wheel/rail normal forces, lateral wheel/rail creepage, dynamic stresses developed in the axle shaft and vertical accelerations of the axle box. The dynamic wheel/rail contact force responses are evaluated using the Hertzian contact model considering both rigid and flexible wheelsets. The contribution due to track slab flexibility to lateral creepage, however, is neglected for both the rigid and flexible wheelsets, so as to study the effects of wheelset flexibility alone on the lateral creepage. The dynamic stress developed in the axle shaft is evaluated using modal stress recovery method, as described in section 2.2.1. The contributions of the wheelset flexibility to the responses are illustrated through comparison with those obtained for the vehicle model employing rigid wheelsets.

2.4 Results and Discussions

2.4.1 Model validation

The wheel flat-induced wheel/rail contact forces have been widely investigated experimentally and analytically. The reported results, however, are limited to relatively lower speeds; only a few studies have numerically investigated wheel flat-induced contact forces at higher speeds, exceeding 300 km/h. The validity of the coupled vehicle/track dynamic model in the presence of wheel flat is thus examined by comparing simulation results with the reported measured data at speed up to 140 km/h [13]. The simulation results are obtained for the flexible wheelsets considering the reported experimental conditions (static axle load= 117.72 kN, wheel flat length, L_f= 40 mm), while the wheel flat is limited to the leading left-side wheel. Simulation results in terms of peak wheel/rail contact force deviations from the static load are compared with the reported measured data in the 0 to 140 km/h speed range in Figure 2.6. The comparisons suggest reasonably good agreements with experimental results in the reported speed range. The simulation results are also presented at higher speeds, up to 400 km/h. The results show that the peak wheel/rail contact force increases with increasing vehicle speed up to about 100 km/h. Both the simulation and experimental results show saturation of the peak force in the 100-120 km/h speed range. The peak contact force tends to decrease with further increase in the speed beyond 120 km/h. Although such a trend of decreasing wheel/rail contact force with increasing speed has not yet been verified through experimental measurements, the simulation results reported in [2] also exhibit same tendency.

The validity of the modal stress recovery method, described in section 2.2.1, is also examined by comparing dynamic stress response of the axle shaft with that obtained from the FE model of the wheelset. The FE analysis of the wheelset was limited only to the static axle load, while the stress response of the coupled vehicle/track model was evaluated at a speed of 100 *km/h* but in the absence of the wheel flat. The steady-state dynamic stress responses are evaluated at different points on the axle shaft surface, as shown in Fig. 2.7 (a). The quasi-static bending stress responses in the FE model was also evaluated at the same locations, which are considered to represent the peak steady-state stress, evaluated from the rotating axle shaft in the coupled model. The peak stress magnitude at a point fixed to either top or bottom surface of the shaft thus equals the static stress. The steady-state bending stress responses at different locations of the rotating axle shaft obtained using the modal stress recovery method, are illustrated in Fig. 2.7(b). The stress responses at all the locations exhibit harmonic variations at the rolling frequency of the wheelset, near 9.58 *Hz*. The peak magnitudes at different locations are compared with those obtained from the FE model in Table 2.1. The comparisons suggest reasonably good agreements between the two at some of the locations, while notable differences are evident in stresses at points A, D and E, shown in Fig. 2.7(a). The modal method yields relatively lower stress magnitudes at all the locations compared to the FE model, which may be attributed to consideration of limited number of deflection modes.
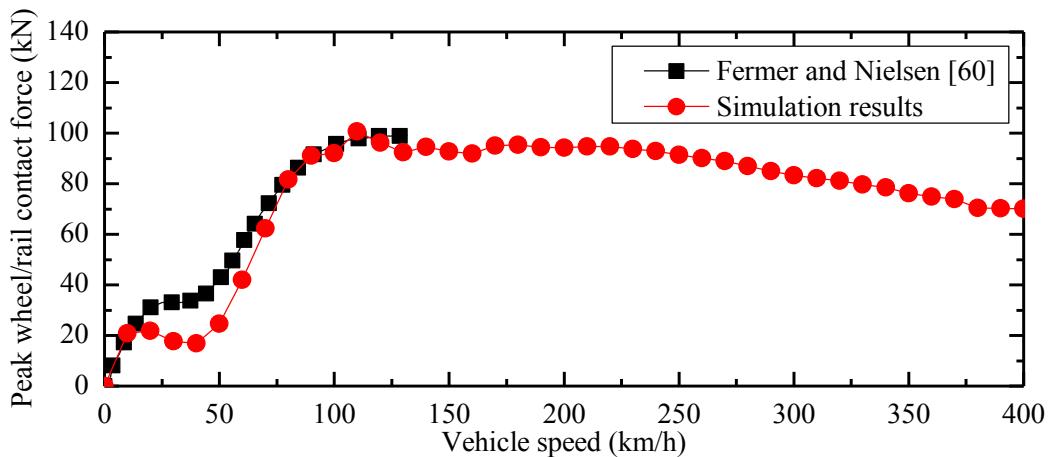
Figure 2.6: Comparisons of peak wheel/rail contact force deviations from the static load with vehicle speed obtained from coupled vehicle/track model with the reported measured data [60] (Flat length: 40 *mm*).
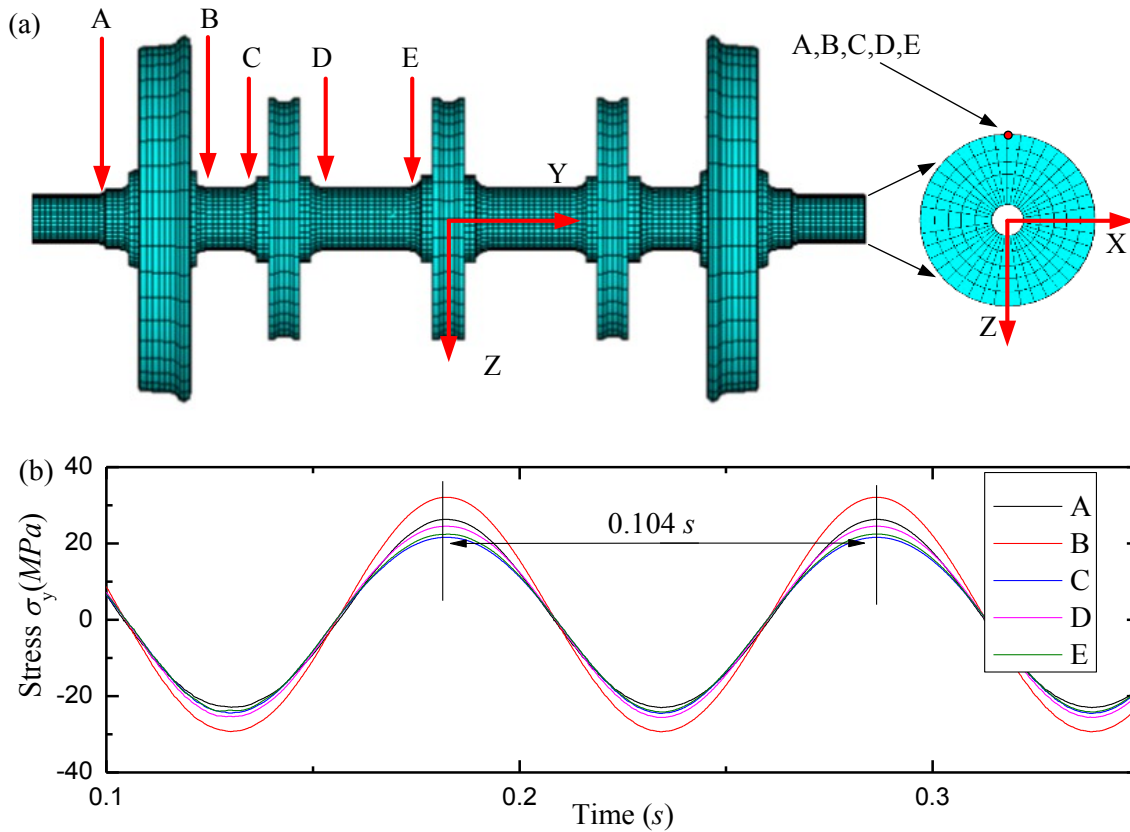
Figure 2.7: (a) Illustrations of points in the wheelset model considered for evaluation of the bending stress; and (b) steady-state stress responses at different location of the rotating axle shaft obtained from modal stress recovery method.

Table 2.1: Comparisons of bending stress magnitudes at different locations of the axle shaft obtained from FE model and modal stress recovery method.

Method	Peak stress at different locations on shaft surface (MPa)				
	A	B	C	D	E
Modal method	25.2	32.1	26.3	25.5	24.3
FEM	29.0	32.6	29.5	29.8	29.7

2.4.2 Vibration modes of the flexible wheelset

Figure 2.8 illustrates some of the vibration modes of the wheelset together with the corresponding frequencies considering free-free boundary conditions. The observed frequencies for the bending and torsion modes are comparable with those reported by Morys [25], although notable differences

were evident. These are attributed to difference in wheelset design and modelling method. The wheelset employed in the reported study [25] comprised 4 brake discs and discrete spring/damping elements to account for bending and torsional elasticity of the wheelset. Baeza *et al.* [55] reported modal frequencies of a wheelset without the brake discs. The study reported first umbrella mode of 298 *Hz*, which is comparable with that obtained for the wheelset considered in this study (267.1 *Hz*). The second umbrella mode frequency was obtained as 372.2 *Hz*, which is substantially lower than 436 *Hz* reported in [55]. The observed difference is believed to be due to differences in the wheelsets considered.
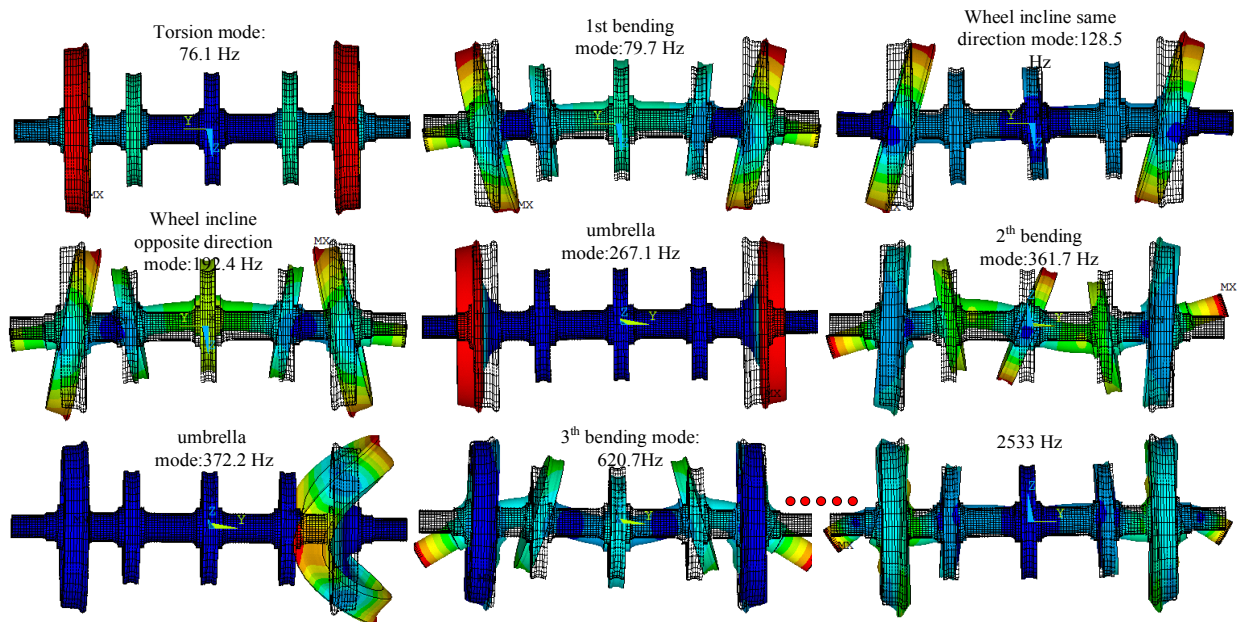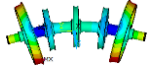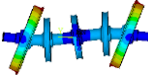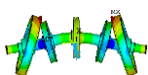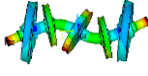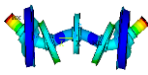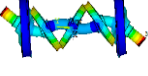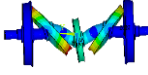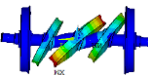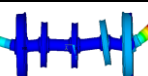
Figure 2.8: Selected vibration modes of the flexible wheelset obtained from the FE model.

The wheelset employed in the coupled vehicle-wheelset-track model is subject to revolute constraint imposed by the axle box and primary suspension apart from the car body and bogie inertia. The couplings may affect some of the vibration modes of the wheelset, especially the bending modes. Studies reporting vibration modes of flexible wheelsets mostly consider free-free conditions [25,55,59]. In this study, the vibration modes and corresponding frequencies of the flexible wheelset are evaluated considering the couplings with the axle box, bogie and the car body, as described in section 2.3. The eigen frequencies of the coupled vehicle-wheelset model were evaluated in the SIMPACK software, and the modes corresponding to the wheelset deformations were extracted. Table 2.2 compares some of the vibration modes of the coupled wheelset with those

of the free-free wheelset. The comparisons suggest significant effect of the couplings on the modal frequencies associated with shaft bending and wheels/brake discs deflections. Relatively small effects were observed on the umbrella mode frequencies.

Table 2.2: Comparisons selected modal frequencies of the coupled and free-free wheelset

Mode shape	Vibration mode	Modal Frequency (*Hz*)	
		Free-free	Coupled
	1st bending	79.7	96.2
			178.2
	In-phase wheels deflections	128.5	116.2
			132.4
	Out-of-phase wheels deflections	192.4	148.5
			225.2
	2nd bending	361.7	280.3
			324.1
	3rd bending	620.7	416.2
			488.1
	4th bending	694.1	536.5
			586.7
	Out-of-phase brake discs deflections	895.9	880.5
			911.7
	In-phase brake discs deflections	899.5	891.2
			905.3
	5th bending	1169.0	826.3
			871.7

For the free-free condition, each bending mode about *x*- and *z*-axis occurred at the same frequency, due to the symmetry. These bending frequencies, however, differ for the coupled wheelset, as seen Table 2.2. The first bending mode of the free-free wheelset occurred at 79.7 *Hz*, while those of the coupled wheelset are observed at substantially higher frequencies of 96.2 *Hz* and 178.2 *Hz*. This is likely due to axle box revolute constraint imposed on the wheelset. The coupling

of the wheelset with the bogie and the car body yields considerably lower values of higher bending mode frequencies compared to the free-free wheelset. The vibration modes of the coupled wheelset associated with in-phase and out-of-phase deflections of wheels and brake discs, however, are relatively close to those of the free-free wheelset. The two frequencies of the coupled wheelset corresponding to each of these modes tend to be lower and higher than that of the free-free wheelset. Owing to considerable coupling effects, the modified modal vectors of the coupled wheelset were considered for determining deflection responses of the wheelset under the suspension and contact forces.

2.4.3 Influences of wheelset flexibility on the wheel/rail contact forces

Figure 2.9(a) illustrates time histories of wheel/rail normal forces obtained considering rigid and flexible wheelset models in the presence of a 60 *mm* long flat in the left-side wheel of the leading wheelset. The results, presented for one complete wheel revolution, are obtained at the forward speed of 300 *km/h*, while a very small integration time step (0.0001 *s*) was chosen to accurately identify the peak force. Contact force obtained with both the rigid and flexible wheelsets, exhibits similar trends. The results show rapid loss of wheel-rail contact as the wheel flat enters the contact patch near *t*=0.7974 *s*. Substantially higher contact force is observed due to impact as the wheel regains its contact with the rail. Subsequently, the contact force exhibits oscillations, which gradually decay to the steady-state contact force. The results suggest that the flexible wheelset results in slightly lower peak impact force compared to the rigid wheelset, as seen in Figure 2.9(a). The observed difference between the contact forces due to flexible and rigid wheelset is in a good agreement with those reported by Nielsen *et al.* [58] and Baeza *et al.* [55].

The dominant frequencies of oscillations in the contact force are identified through Fast Fourier Transform (FFT) of the force time-history for one wheel revolution, excluding the data corresponding to loss of contact and primary impact (0.799≤*t*≤0.83 *s*). Figure 2.9(b) illustrates the frequency spectrum of the contact force, which suggests dominant frequency of 624 *Hz* for both the rigid and flexible wheelsets. This frequency is attributed to the rail bending mode. The results obtained with flexible wheelset also exhibit a secondary peak near 824 *Hz*, which corresponds with one of the higher bending mode (Table 2.2). The results also show peak around 74.9 *Hz*, which has been attributed to the wheel/rail coupled vibration mode for the rigid wheelset [40]. The results further show that magnitude of the contact force in the vicinity of this frequency is substantially

lower for the flexible wheelset compared to that of the rigid wheelset. This is likely due to first bending mode of the flexible wheelset.
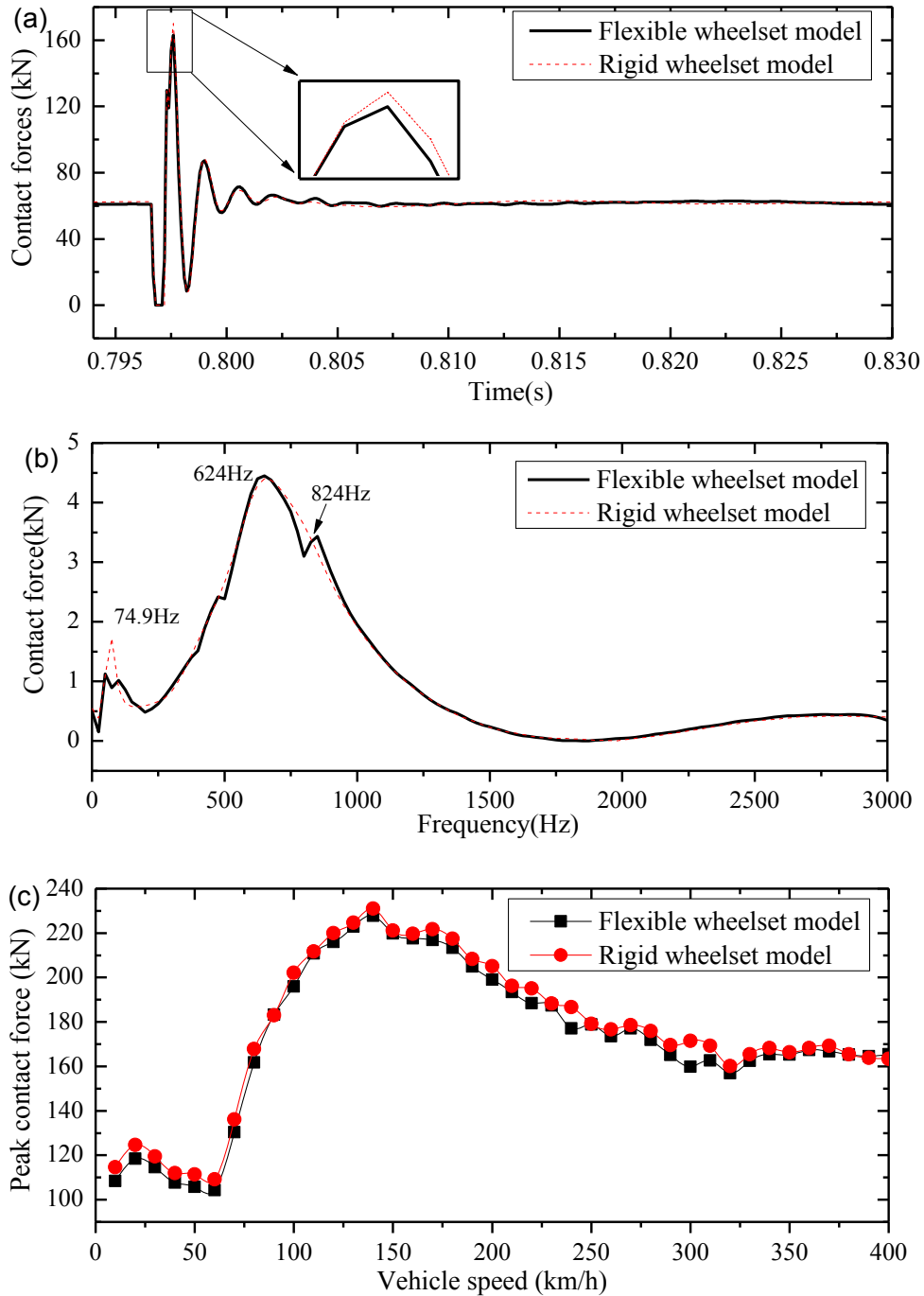
Figure 2.9: Comparison of peak wheel/rail contact force obtained for the flexible and rigid wheelset models: (a) Time histories of contact force at 300 *km/h*; (b) frequency spectrum of the contact force; and (c) variations in peak contact force with vehicle speed.

The peak contact force is strongly influenced by the forward speed, which also determines the contact duration of the flat with the rail during each revolution. Both the rigid and the flexible wheelset models show comparable dependency of the contact force on the forward speed, as shown in Figure 2.9(b). The peak magnitudes of the impact forces of both the wheelsets show a smaller peak around 25 *km/h* speed, followed by a rapid increase with increasing speed due to loss of wheel-rail contact. The peak impact approaches its maxima near 140 *km/h* and decreases with further increase in the speed. Such trends have also been reported in a number of studies [2,134]. In the lower speed range, the wheel flat impacts the rail as it regains contact, which leads to larger penetrations at the wheel/rail interface and thus higher impact force. The contact between the flat and the rail, however, may not occur at higher speeds when wheel impacts the rail as it regains the contact, which contributes to relatively lower impact force. Moreover, the duration of the flat contact with the rail also decreases with increasing vehicle speed.

2.4.4 Influences of wheelset flexibility on wheel/rail creepage

The elastic deformations of the wheelset caused by high magnitude wheel flat-induced impact force can also contribute to fluctuations in the wheel/rail creepage, which could cause uneven wear on the wheel circumference. The simulation results are obtained to study the influence of wheelset flexibility on the wheel/rail creepage in the presence of interactions with a wheel flat. The results are also obtained for the rigid wheelset model. Simulations are performed for the rigid track slab so as to study the effects of wheelset flexibility alone on the wheel/rail creepage.

Figure 2.10 compares time-histories of lateral wheel-rail creepage obtained for the rigid and flexible wheelset models under excitations due to 60 *mm* long flat and forward speed of 300 *km/h*. The results clearly show significantly higher variations in lateral creepage with the flexible wheelset compared to the rigid wheelset, which is attributed to elastic deformations of the wheelset. The results suggest predominant oscillation frequencies of about 166 *Hz* and 430 *Hz* for the rigid and flexible wheelsets, respectively. The frequency for the flexible wheelset corresponds to the 3rd bending mode of the wheelset coupled with out-of-phase lateral motions of the wheels, as seen in Table 2.2. The frequency for the rigid wheelset was attributed to its roll and yaw motions due to asymmetric radial deformations of the longitudinal elastic mount between the axle box and the bogie.
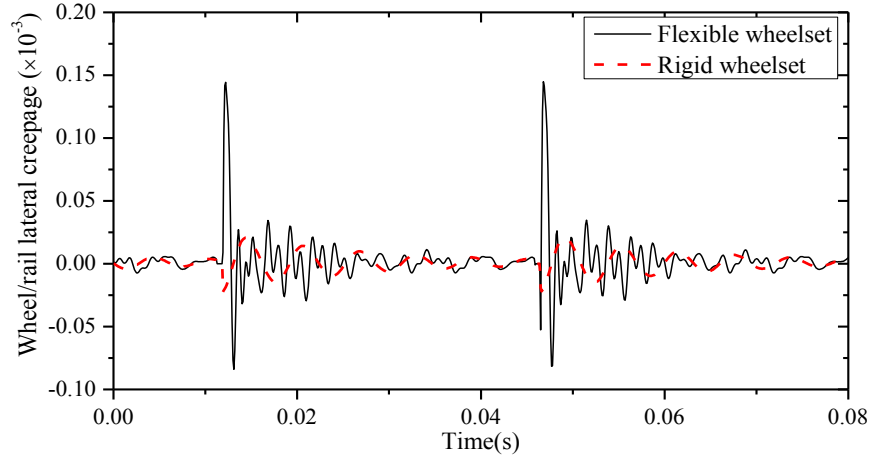
Figure 2.10: Influence of the wheelset flexibility on the wheel/rail lateral creepage in the presence of a wheel flat.

2.4.5 Influences of wheelset flexibility on axle box acceleration

The wheelset deformations under a flat-induced impact force can also lead to considerable axle box motion, which has been suggested as an effective measure for detecting wheel/rail defects [158]. Figure 2.11 illustrates variations in vertical axle box acceleration responses of the model with flexible and rigid wheelsets due to 60 *mm* long wheel flat excitation at a forward speed of 300 *km/h*. The results clearly show significantly large acceleration response of the model with flexible wheelset compared to the rigid wheelset. This is attributed to deflections of the flexible wheelset, especially those caused by shaft bending. The axle box accelerations response with the rigid wheelset exhibit substantially lower peak and rapid decay compared to that with the flexible wheelset. The oscillations in the acceleration response with the flexible wheelset occur at relatively higher frequencies in 400-500 *Hz* range and near 824 *Hz*, attributed to third and fifth bending modes of the wheelset shaft (Table 2.2), respectively.

The effect of forward speed on the peak axle box acceleration is also investigated and illustrated in Figure 2.11(b) in the 10 to 400 *km/h* speed range. The results show substantially higher peak acceleration with the flexible wheelset compared to the rigid wheelset in the entire speed range, particularly above 30 *km/h*. The effect of speed on the axle box acceleration is comparable to that observed for the contact force for both rigid as well as flexible wheelsets. This is evident from reasonably good correlation between the peak contact force and peak axle box acceleration in the entire speed range, as seen in Fig. 2.11(c).
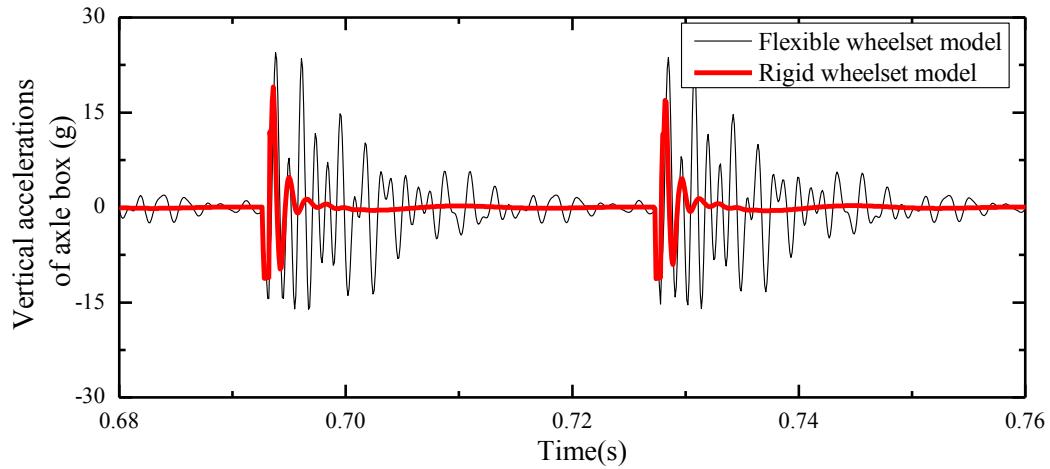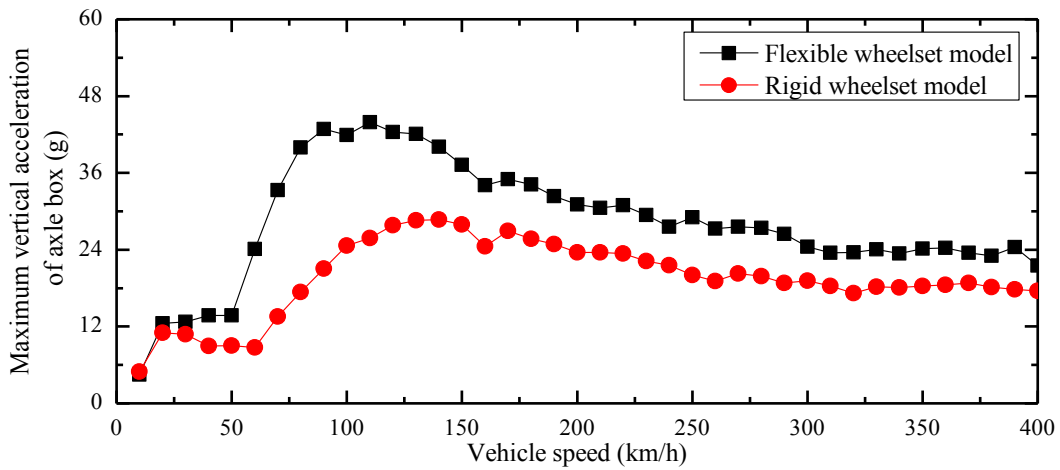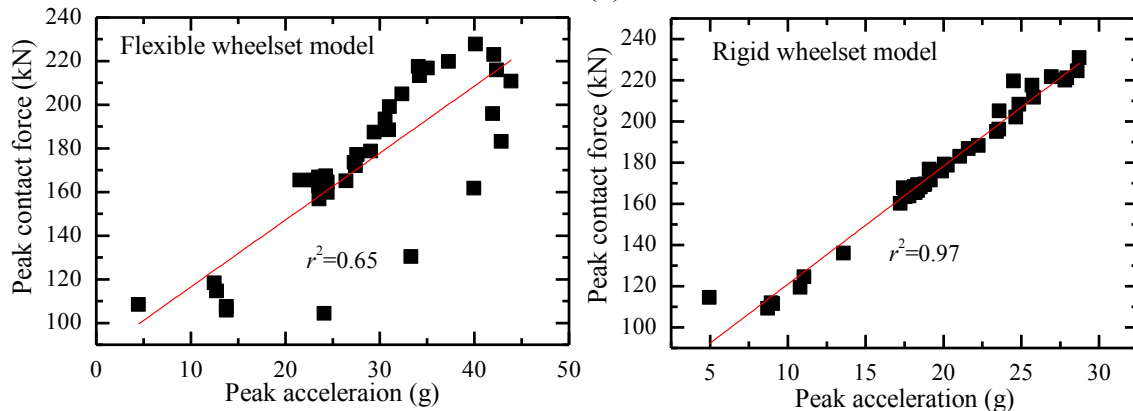
Figure 2.11: Comparison of peak vertical axle box acceleration obtained for the flexible and rigid wheelset models: (a) Time histories of axle box acceleration at 300 *km/h*; (b) variations in peak acceleration with vehicle speed; and (c) correlations between peak contact force and peak acceleration responses.

The figure further shows substantial differences between the responses obtained with flexible and rigid wheel sets. A very good correlation between the peak contact force and axle box acceleration is observed for the rigid wheelset (correlation coefficient, $r^2 > 0.9$). The correlation coefficient for the flexible wheelset is in the order of 0.65. The maximum of peak axle box acceleration occurs near 90 and 140 *km/h* for the flexible and rigid wheelsets, respectively. The maxima of peak contact force for the two wheelsets, however, occur at the same speed (near 140 *km/h*), as seen in Fig. 2.9(b). This further shows considerable contribution of wheelset deformation to the axle box acceleration. Results in Fig. 2.11(c) suggest that axle box acceleration can serve as a reliable direct measure of the wheel flat induced force in case of a rigid wheelset. The effectiveness of this measure, however, needs to be examined further for a flexible wheelset.

2.4.6 Influences of wheelset flexibility on axle shaft stress

The stress developed in the axle shaft of the flexible wheelset is initially computed in the absence of the wheel flat using equation (5), which is denoted as the quasi-static stress. The total stress developed due to the impact force arising from the 60 *mm* long flat is subsequently evaluated. The dynamic stress, attributed to the wheel flat excitation alone, is determined by subtracting the quasi-static stress from the total stress in the axle shaft. As an example, Figure 2.12 illustrates variations in dynamic stress developed at Point B on the axle shaft (Figure 2.7a) due to the wheel-rail contact force at a speed of 100 *km/h*. The results show that impact force yields considerable dynamic stress in the shaft. The oscillations in dynamic stress response predominantly occur near 414 *Hz*, attributed to 3rd bending vibration mode of the flexible wheelset.
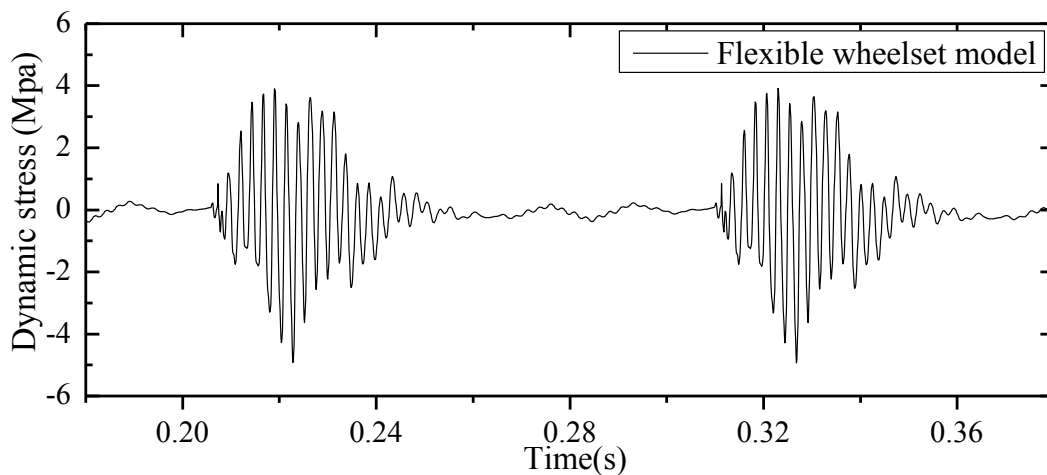
Figure 2.12: Dynamic stress developed at point B on the flexible wheelset shaft surface under excitations from the wheel flat at a speed of 100 *km/h*.

2.5 Conclusions

A coupled high-speed vehicle/track model integrating flexible wheelsets was developed in the SIMPACK platform to investigate influences of wheelset flexibility on dynamic responses in the presence of a wheel flat. The contributions of the wheelset flexibility are demonstrated by comparing the dynamic responses obtained with rigid wheelsets. Substantial effects of wheelset flexibility were observed on the peak wheel/rail creepage, peak axle box acceleration and dynamic stress developed in the wheelset axle shaft, when compared to those obtained with rigid wheelsets. The deformations of the flexible wheelset, however, revealed slightly lower magnitudes of peak wheel/rail contact force compared to the rigid wheelsets. It is further shown that the dynamic stress developed in the flexible wheelset axle shaft can be directly obtained from the deflection responses using the modal stress recovery method. The responses obtained for the flexible wheelset revealed high amplitude oscillations at relatively higher frequencies attributed to third bending mode of the axle shaft, and out-of-phase motions of the right- and left-side wheels. Very good correlation was observed between the peak contact force and peak axle box acceleration for the rigid wheelset, which was considerably lower for the flexible wheelset. The reliability of the axle box acceleration as a measure of wheel defects thus needs to be further examined in the presence of wheelset deformations.

CHAPTER 3: DYNAMIC RESPONSES OF A HIGH-SPEED RAILWAY CAR DUE TO WHEEL POLYGONALIZATION

3.1 Introduction

Wheel polygonalization, regarded as periodic radial irregularities along the wheel circumference, has been associated with high magnitudes of high frequency loads at the wheel/rail interface. The wheel-rail contact forces contribute to undesired dynamic responses and reduced fatigue lives of the vehicle/track sub-structures, especially under high speed operations [33,61,62]. Considerable measurements and simulation efforts have been made in identifying various contributory factors leading to growth in high-order wheel polygonalization. Such efforts, however, have been limited to lower order wheel polygonalization and wheel-rail interactions in the lower frequency range [1,21-26]. High order wheel polygonalization, characterized by variations in wheel radius occurring in the 18~24 harmonic orders, has been observed in a number of high-speed trains due to frequent in-service fatigue failures [33,34,65,68]. Such high order wheel polygonalization can result in high magnitudes of high frequency contact forces under high-speed operations. The exact mechanism leading to formation of high-order wheel polygonalization has not yet been identified. Although the investigations on high order wheel polygonalization have been reported in a few studies, many gaps are evident due to the limitations in the simple vehicle and track models considered in the reported studies.

This Chapter presents a more comprehensive investigation on the effects of the high order wheel polygonalization under high-speed operations using the vehicle/track dynamic model presented in Chapter 2. On the basis of the proposed model, the axle box is further modelled as a flexible body using the modal approach. The validity of the model in estimating the axle box acceleration is demonstrated by comparing the model response with the field-measured data in terms of the axle box acceleration in the presence of the 18th order wheel polygonalization. Using this model, the effects of amplitude and harmonic order of wheel polygonal wear are subsequently investigated in terms of wheel/rail contact forces, axle box acceleration and dynamic stresses developed in the wheelset axle.

3.2 Coupled vehicle/track dynamic model

A coupled vehicle/track dynamic model is formulated to investigate effects of amplitude and harmonic order of the polygonal wheel wear on dynamic responses at the wheel-rail interface and those of the wheelset. The simulation model integrates the dynamic model of a high-speed rail vehicle coupled with a slab track dynamic model via the flexible wheelsets. The interactions between the vehicle and the track are described through the wheel/rail contact model. Figure 3.1 illustrates the simulation scheme of the proposed coupled vehicle/track dynamic model. The high-speed rail vehicle considering the flexibility of the wheelset and the axle box is modelled in the SIMPACK platform, while the slab track model is formulated in the SIMULINK platform. In the simulation scheme, the wheel/rail contact forces are initially evaluated using the wheel/rail contact model, which subsequently serve as external excitations to the slab track model to determine its deflection responses, as described in [29]. The resulting track deflections at the discrete wheel/rail contact point are subsequently integrated to the vehicle dynamic model via the SIMAT (SIMPACK-MATLAB) co-simulation interface to investigate dynamic responses of the coupled system in the presence of wheel polygonalization.
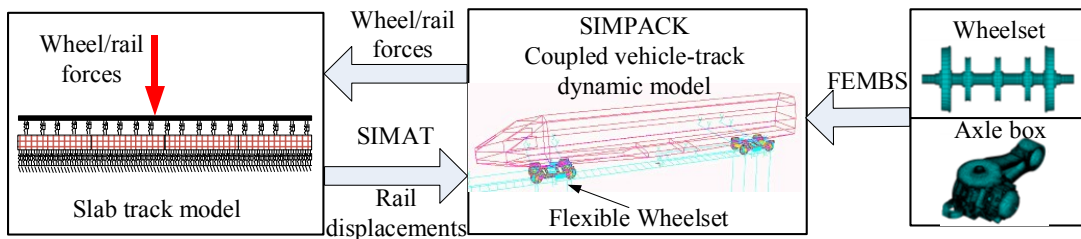
Figure 3.1: Simulation scheme for the coupled flexible wheelset-vehicle-track model.

3.2.1 Vehicle and track model

The vehicle is modeled as a multi-body dynamic system consisting of a car body supported on two bogie frames via air springs. Each wheelset is coupled to the bogie frame via coil springs in the vertical direction. In the longitudinal direction, the wheelset is connected to the bogie frame through two axle boxes, supported on elastic mounts. The wheelsets and axle boxes are modeled as flexible bodies, since a typical 20th wheel polygonalization can give rise to a fundamental excitation frequency of approximate 580 *Hz* for a nominal speed of about 300 *km/h* and its multiples, namely, 1160 *Hz* and 1740 *Hz*. The wheel-rail contact forces at such high frequencies may excite some of the vibration modes of the wheelset and the axle boxes [29,33,62]. For this purpose, the

modal approach is used to account for various deformation modes up to 2533 *Hz*. The displacement at any given point on the wheelset or axle box can be expressed by [159]:

$$\mathbf{d}(\mathbf{c}, t) = \mathbf{c} + \mathbf{u}(\mathbf{c}, t) \tag{1}$$

where $\mathbf{c}$ is the position vector and $\mathbf{u}(\mathbf{c}, t)$ is elastic deformation at the given point, which is obtained using the modal method, such that:

$$\mathbf{u}(\mathbf{c}, t) = \mathbf{\Phi}\, \mathbf{q}_w(t) \tag{2}$$

where $\mathbf{\Phi}$ denotes the modal matrix and $\mathbf{q}_w(t)$ is the generalized modal coordinates vector. Using the modal stress recovery approach, the stress $\mathbf{\sigma}$ at a point in the wheelset axle can be obtained from wheelset deformations [155], such that:

$$\mathbf{\sigma} = \mathbf{D\varepsilon} = \mathbf{DL\Phi q} \tag{3}$$

where $\mathbf{D}$ is the elasticity matrix, and $\mathbf{L}$ is the linear operator relating to strain $\mathbf{\varepsilon}$ and displacement $\mathbf{u}$.

The modal matrices for the wheelset and axle box are obtained using the finite element (FE) models formulated and analyzed in the ANSYS platform, as seen in Figs. 3.2(a) and 3.2(b), respectively. For this purpose, a total of 256 master nodes located on 16 cross sections of the wheelset along the axle direction are selected. These include two cross sections at the extreme left- and right-ends of axle shaft, and each side of the wheels and brake discs. Additional four cross sections are selected at the axle shaft sections between the wheel and the brake discs, and between the consecutive discs. For the axle box model, 140 master nodes located on the surface of the axle box are taken into consideration. The vehicle model is analyzed considering lower 34 and 10 vibration modes of the wheelset and the axle box, respectively, occurring at frequencies up to 2533 *Hz*.

The track is modelled as a slab track, where the rail is discretely supported on the slab via the fasteners, while the slab is continuously supported on the ground via the CAM (cement asphalt mortar) layer. The Timoshenko beam theory is used to describe flexibility of the rail, which is considered more realistic up to frequencies of 2500 *Hz* [80]. The deformation responses of the flexible slab are described using the finite element method, as described in [29].

The vehicle and track system models are coupled via the wheel/rail contact model. The tangential forces and moments at the wheel/rail contact points are evaluated using the FASTSIM algorithm considering the S1002CN wheel tread profile coupled with the Rail 60 profile, while the normal forces are determined via the Hertz contact theory [160].
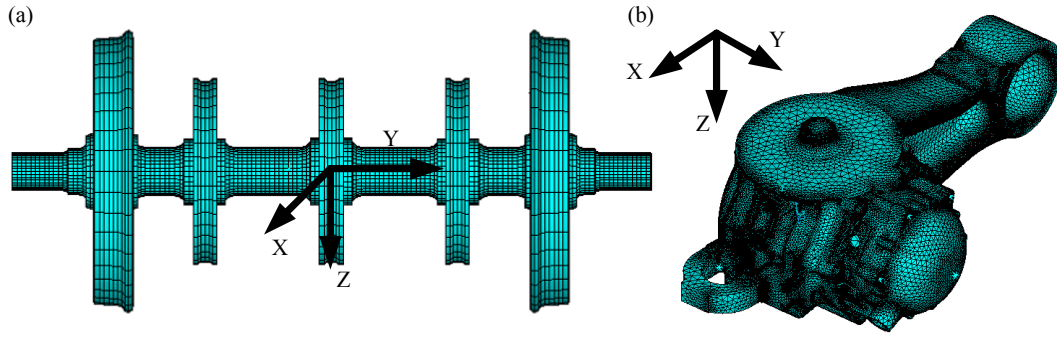
Figure 3.2: Finite element models of: (a) the wheelset; and (b) the axle box.

3.2.2 Wheel polygonalization

The wheel polygonalization is described by variations in the wheel radius as a function of angular position of the wheel φ. Figure 3.3(a) illustrates the OOR deformities measured on a wheel, which suggests nearly periodic variations or wheel polygonalization. The measured wear profile is idealized by a periodic waveform superimposed on the wheel circumference, as seen in Fig.3.3 (b).

(a)   (b)
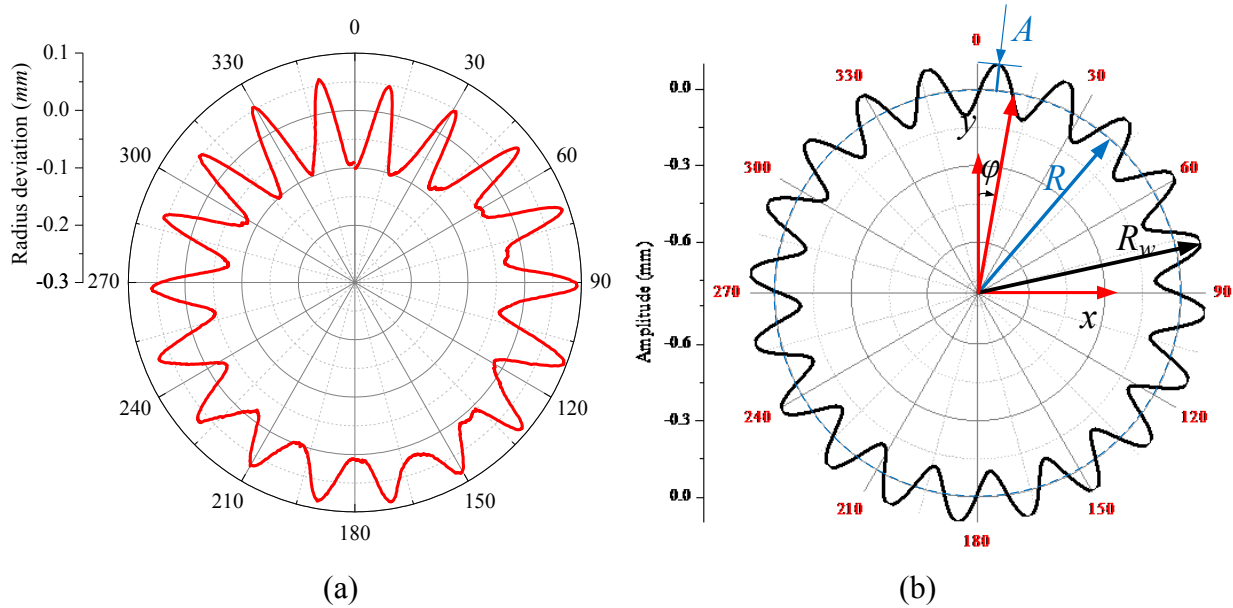
Figure 3.3: (a) Measured circumferential polygonal wear; and (b) polygonal wear idealized by a harmonic waveform.

The coordinates of a point on the circumference or the contact point can thus be expressed as:

$$x = (R + A \sin N\varphi) \sin \varphi ; \quad y = (R + A \sin N\varphi) \cos \varphi ; \quad \varphi = \in [0, 2\pi] \qquad (4)$$

where x and y are the coordinates of a point on the wheel circumference, A denotes amplitude of the polygonal wear, N is the order of harmonic of the polygonal wear and R is nominal wheel radius. The radius of the wheel at a given point on the wheel circumference can be given by $R_w = R +$

$A \sin N\varphi$. The variation in the wheel radius ΔR of the polygonal wheel at the wheel/rail contact is thus expressed as a function of the angular position φ, as:

$$\Delta R = A \sin N \varphi \qquad (5)$$

The polygonal wear of the wheel, shown in Fig.3.3 (a), may be more accurately characterized by a random waviness with a few dominant spectral components. The roughness of the measured polygonal wear has also been expressed by its root mean square value corresponding to center frequency of the third-octave bands [22].

3.3 Field Measurements and model validation

The field measurements were performed on a high-speed train operating at a nominal speed of 300 *km/h* on the nearly 1000 *km* long Wu-Guang (Wuhan to Guangzhou in China) railway line. The vertical acceleration response of one of the axle box mounted on a wheelset with wheels exhibiting typical polygonal wear was measured using an accelerometer during the route. The accelerometer signal was recorded on an on-board data acquisition system at a sampling rate of 5000 *Hz*. The circumferential profiles of wheels, in the order of 80,000 *km* following the re-profiling, were measured prior to the route. The selected wheels revealed consistent wear of polygonal nature. While the order of the polygonal wear was consistent across the wheels, the amplitudes of wear differed. Figure 3.4(a) illustrates variations in radii of the left- and right-wheels of one of the selected wheelsets. The measured variations of the two wheels over one complete revolution are analyzed using Discrete Fourier Transform (DFT) in order to identify the dominant harmonic orders. Figure 3.4(b) illustrates *rms* spectra of the roughness corresponding to each harmonic order ranging from 1 to 40. Both, the left- and right-wheels show presence of periodic wear with predominant wavelength in the order of 145 *mm*. For the operating speed of 300 *km/h*, this represents the dominance near 574 *Hz* or approximately 18th order of the fundamental wheel rotation speed. This is also evident from the *rms* spectra of the wheels' profile variations in Fig. 3.4(b), which clearly show dominance of the roughness of both wheels near the 1st, and 17th and 18th harmonics. The spectra also show a peak in the vicinity of multiple of the 18th order, near the 36th harmonic order.

The validity of the proposed coupled vehicle/track system model was examined by comparing the axle box acceleration response with the measured data acquired during field measurements. For this purpose, the model simulations are conducted under excitations due to measured polygonal wear profiles of the left- and right-wheels, shown in Fig. 3.4(a). As an example, Figure 3.5(a)

illustrates time-histories of left axle box vertical acceleration obtained from the field tests and the simulation model over a period of 0.5 *s* at an operating speed of 300 *km/h*. Both, the measured as well as simulation results show substantially high magnitudes of axle box vertical acceleration, with peaks exceeding 150 *g*. Such high magnitude acceleration response of the axle-box is attributable to high magnitude impact loads caused by wheel polygonalization at the wheel/rail interface. Moreover, the acceleration response shows high frequency components, which are due to higher order of the OOR deformities, and bending and torsional deformations of the wheelset. Fast Fourier Transforms (FFT) of the measured and model responses are also compared in Fig. 3.5 (b) considering a 0.5 s duration sample. The figure also illustrates the spectra zoomed in the 400 to 600 *Hz* frequency range. The spectra of the measured and model responses are quite comparable. Both the measured and model response spectra exhibit two dominant peaks occurring at identical frequencies of 532 *Hz* and 563 *Hz*. These frequencies corresponds to 17th and 18th orders of the measured wheel polygonalization (Fig. 3.4(b)) considering the fundamental wheel rotation frequency of 31.2 *Hz*.
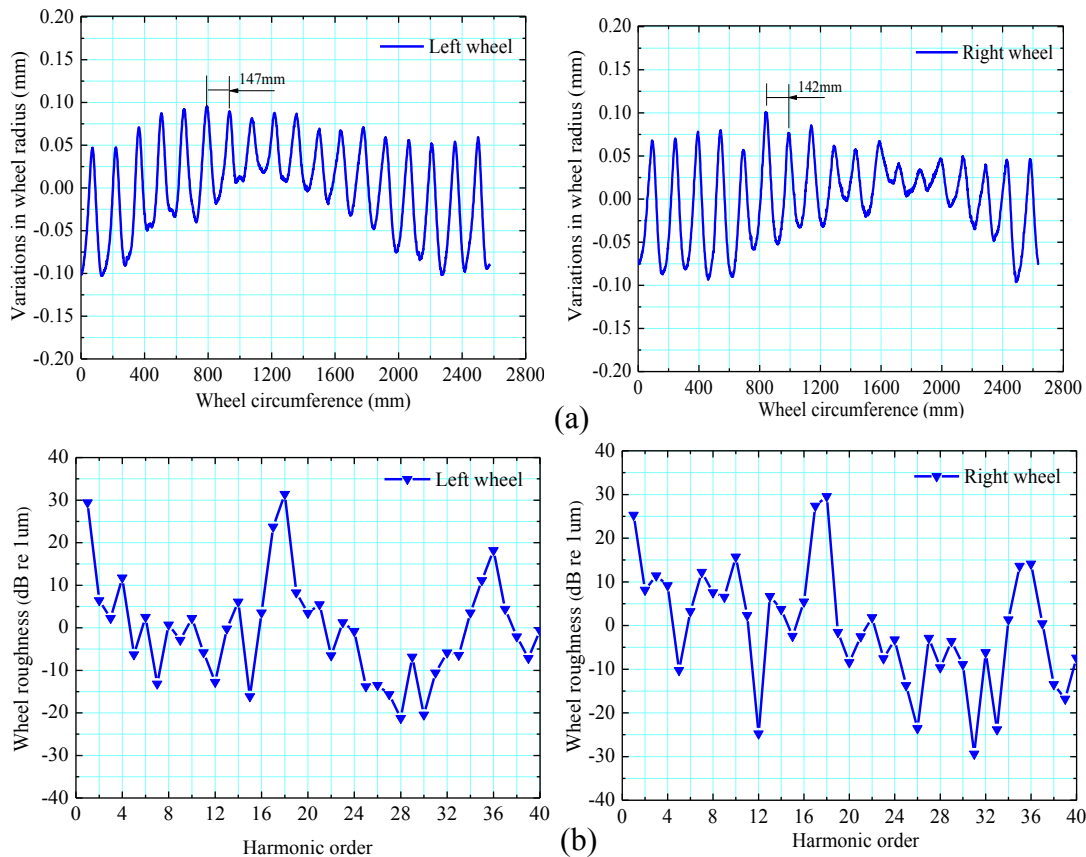
Figure 3.4: (a) Variations in radii of the left- and right-wheels; and (b) spectra of *rms* roughness of the left- and right-wheels as a function of the harmonic order.
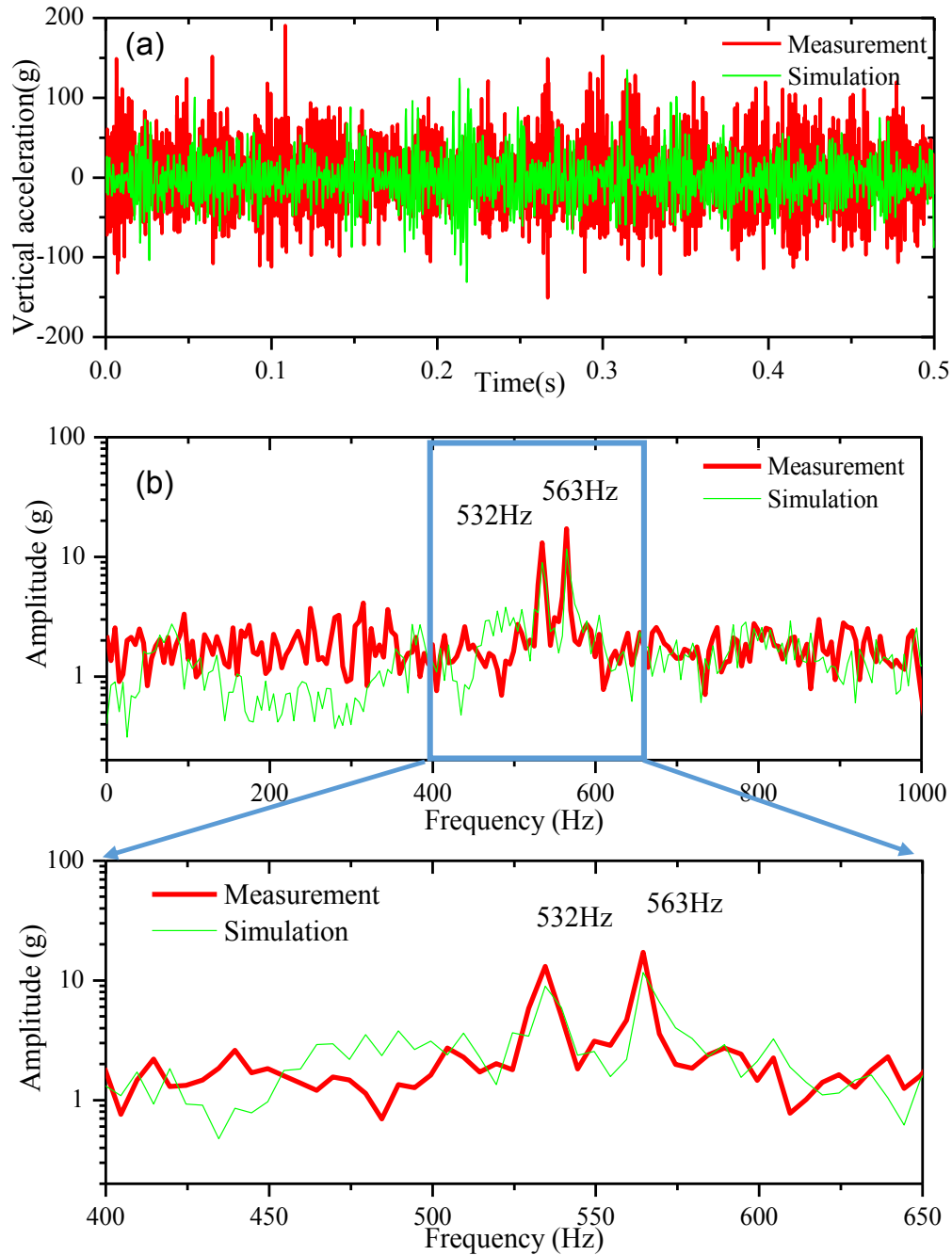
Figure 3.5: (a) Time-histories of the left- axle box acceleration obtained from the model and the measured data; and (b) comparisons of frequency spectra of measured axle box acceleration with that of the model in the 0-1000 *Hz* and 400-600 *Hz* frequency ranges (speed=300 *km/h*).

The peak response corresponding to the 18th-order frequency (563 *Hz*) is greater than that near the 17th-order frequency. While both the measured and model results show nearly identical dominant frequencies of the axle box acceleration, the peak magnitudes differ considerably. The peak values obtained from the simulation model are nearly 25% lower than those observed from

the measured data. Besides, the analytical model underestimates the response in the 150 *Hz* ~ 400 *Hz* frequency range. This is partly due to lack of considerations of the short wavelength track irregularities, linear representation of the rail pad and in-part to consideration of limited number of vibration modes of the flexible wheelset and the axle box.

3.4 Results and Discussions

In this study, the measured polygonal wear is idealized by a harmonic variation in the wheel radius, as described in section 3.2.2. The vehicle/track model simulations are subsequently performed to evaluate dynamic responses of the vehicle system under excitations caused by polygonal wear described by its dominant harmonic order. The effect of harmonic order of the polygonal deformations on the dynamic responses are further investigated. The simulation results in each case are obtained under excitations due to polygonal wear of both the left- and right-wheels of the leading wheelset of the front bogie, and a constant forward speed of 300 *km/h*, assuming negligible phase difference between the two wheels' deformities.

3.4.1 Wheel/rail impact loads

Figure 3.6 illustrates the vertical contact forces developed at the wheel/rail interface of the leading bogie due to identical polygonal wear of both the right- and left-wheels at the speed of 300 *km/h*. The polygonal wear is described by the 18*th* harmonic order with wear amplitude, $A = 0.05$ *mm*, and wheel radius, $R = 0.424$ *m*. Owing to the polygonal wear, the leading wheelset exhibits substantially higher magnitude oscillations in the wheel/rail contact force about the static wheel load of 60 *kN*. The peak contact force approaches 117.1 *kN*, while the peak-to-peak magnitude is 109.5 *kN* with oscillation period, $\tau=0.00177$ *s*. The oscillation period is related to the vehicle speed *v*, the wheel radius *R*, and the order of polygonal wear *N*, such that $\tau=2\pi R/Nv$. Relatively smaller variations, however, are observed in the wheel/rail contact forces of the rear wheelset, which is likely due to dynamic responses of the bogie and the rail resulting from high magnitude variations in the leading wheels contact forces. The results show considerable phase delay between the leading and trailing wheelsets contact forces, which can be attributed to the wheelbase, a forward speed, and propagation speed of the vibration wave along the flexible track.
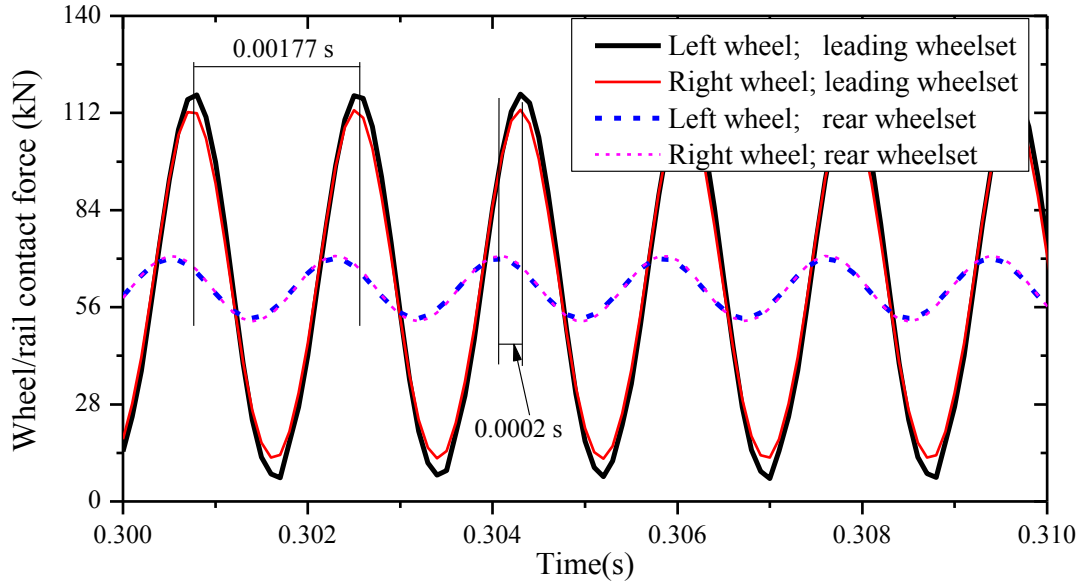
Figure 3.6: Variations in the wheel/rail contact forces developed at the front and rear wheelsets due to 18th harmonic order polygonal wear of the left- and right-wheels of the leading wheelset of the front bogie (speed = 300 *km/h*).
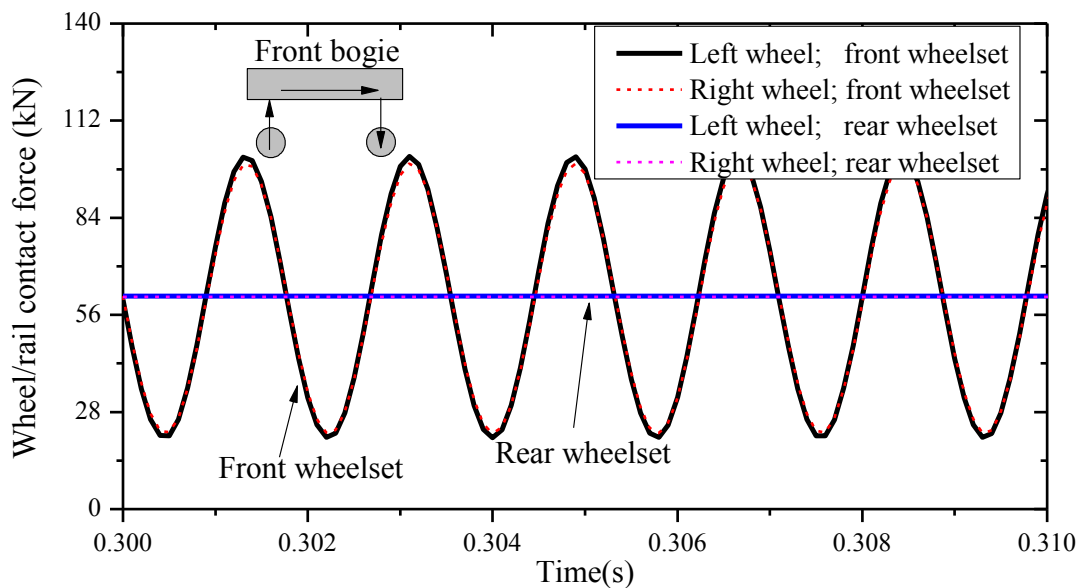
Figure 3.7: Variations in wheel/rail contact forces developed at the front and rear wheelsets on a rigid track due to 18th harmonic order polygonal wear of the left- and right-wheels of the leading wheelset (speed = 300 *km/h*).

The contribution of dynamic responses of the bogie alone to the rear wheelset contact forces is further investigated by replacing the flexible slab track model with a rigid track model. The results show only negligible rear wheels contact forces suggesting negligible contributions of the bogie dynamics (Fig. 3.7). It may thus be deduced that the contact forces developed at the rear

wheelset (Fig. 3.6) are attributable to oscillatory motions of the flexible slab track, caused by polygonal wear of the front wheelset.

During operation, the polygonal wear may be limited to only one of the wheels of a wheelset. Simulations are performed to study the dynamic responses caused by 18th order polygonal wear of the left wheel alone. The results in Fig. 3.8 show dominant contact force limited only to the wheel-rail contact of the left wheel of the leading wheelset. The forces developed at the other wheels are substantially smaller. The results also show intermittent separation of the affected left wheel from the rail. Moreover, the peak magnitude of the contact force developed at the left wheel is slightly higher than that obtained with polygonal wear of both the wheels (Fig. 3.6). The results suggest that the presence of polygonal wear in only one wheel could cause more severe impacts at the wheel/rail interface. The right wheel also exhibits fluctuations in the wheel/rail contact force with relatively small amplitudes, which are believed to be caused by dynamic deformations of the flexible slab track, and roll motion and bending deformations of the flexible wheelset due to polygonal wear-induced impacts.
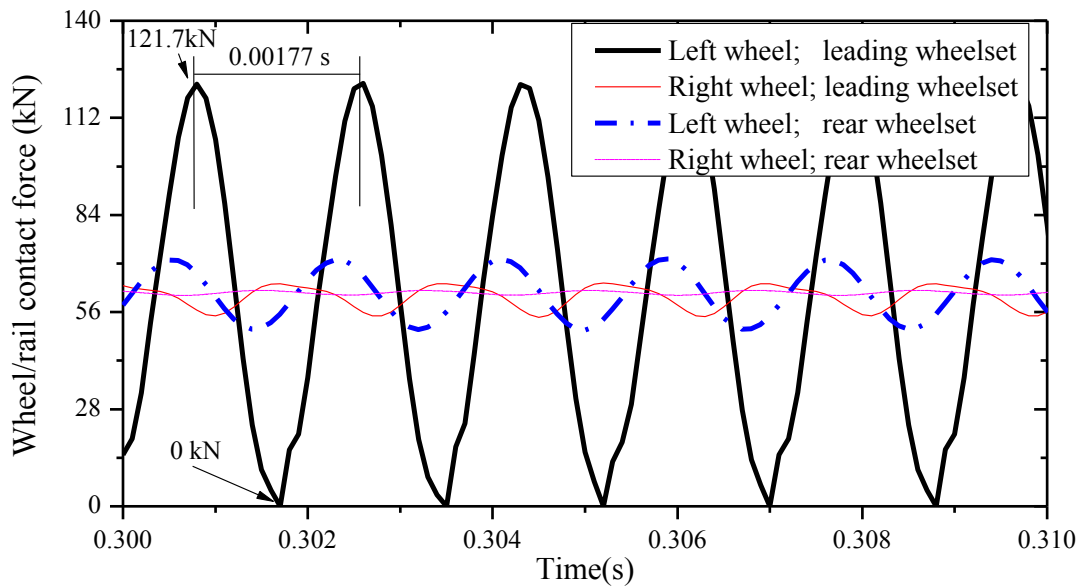
Figure 3.8: Variations in the wheel/rail contact forces developed at the front- and rear- wheelsets on a flexible track due to 18th harmonic order polygonal wear of the left-wheel alone of the leading wheelset (speed = 300 *km/h*).

3.4.2 Axle box acceleration

The high magnitude impact loads at the wheel/rail interface coupled with high frequency vibration of the flexible wheelset cause considerable magnitude of the axle box acceleration, which could further serve as an indicator of the wheel polygonalization or OOR defect. Figure 3.9(a) illustrates variations in the axle box vertical acceleration under excitations arising from the 18th order polygonal wear of both the wheels of the leading wheelset, while operating at two different speeds: 200 and 300 *km/h* (*A*= 0.05 *mm*). Owing to the idealized circumferential polygonal wear of the wheels, the axle box acceleration exhibits periodic oscillations at the wheel polygonalization passing frequencies of 375.6 *Hz* and 562.7 *Hz* at the speeds of 200 and 300 *km/h*, respectively, which correspond to 18 times the wheel rotation frequencies. This is further evident from the frequency spectrum of the acceleration responses, shown in Fig. 3.9(b). The results clearly show substantial effect of forward speed on the axle box acceleration response. The spectra also show presence of secondary peaks near 750 *Hz* and 1127 *Hz*, respectively, for the 200 and 300 *km/h* speeds. These are approximately second multiple of the passing frequency of the polygonal wear. While the magnitude of the secondary peak is negligibly small at the lower speed, it is significantly higher at the higher speed of 300 *km/h*. The frequency of the second peak is likely due to elastic deformations of the flexible wheelset. The fifth bending mode frequency of the free-free wheelset axle resulting in considerable deflection at the ends of the axle shaft, illustrated in Fig. 3.9(b), has been reported as 1169 *Hz* [29].

Figure 3.10 illustrates the frequency spectrum of the axle box acceleration response obtained with the rigid wheelset model. Comparison with the acceleration spectra in Fig. 3.9(b) shows considerably lower axle box acceleration response with the rigid wheelset than that with the flexible wheelset model at the primary frequency of 562.7 *Hz*. Furthermore, the secondary acceleration peak near 1126.9 *Hz* vanishes for the rigid wheelset, which further suggests that the wheel-rail interactions near 1126.9 *Hz* excite a deformation mode of the flexible wheelset.
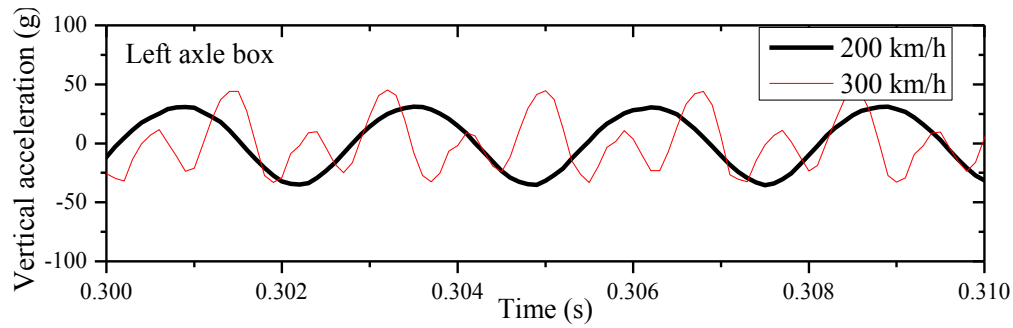
(a)
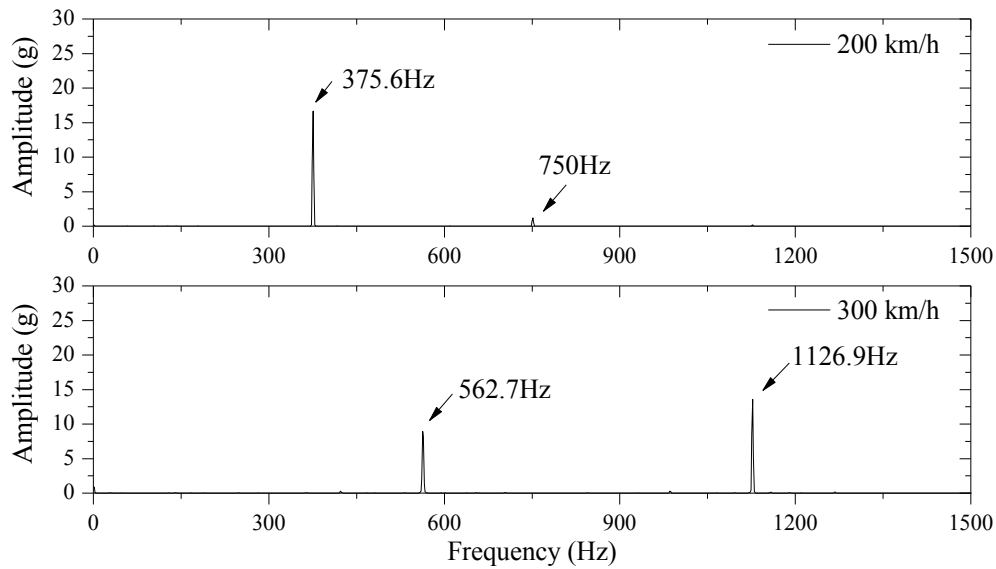
(b)

Figure 3.9: Axle box acceleration responses due to 18th-order polygonal wear obtained at forward speeds of 200 and 300 *km/h*: (a) time- histories, (b) frequency spectra.
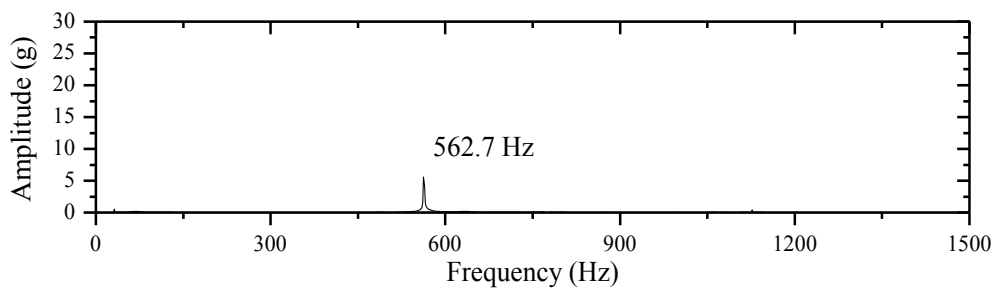
Figure 3.10: Frequency spectrum of the axle box acceleration response obtained with the rigid wheelset model under excitation due to 18th-order polygonal wear: (speed = 300 *km/h*).

3.4.3 Bending stress in the axle shaft

The elastic deformations of the wheelset shaft due to high frequency impact forces at the wheel/rail interface may contribute to dynamic bending stress in the axle shaft. The bending stress developed

in the axle shaft under impact loads caused by the 18th order polygonal wheels' wear is evaluated using the modal stress recovery method [29]. The results obtained under identical wear of the both the wheels and forward speed of 300 *km/h* are compared with those in the absence of the polygonal wear-induced excitations in Fig. 3.11(a). The figure illustrates the stress in the bearing section of the shaft. In the absence of polygonal wear, the bending stress is primarily due to the static load, while its oscillations frequency corresponds to the wheel rotation (about 31.3 *Hz*). The mean magnitude of the bending stress under polygonal wear-induced excitation is comparable to that obtained in the absence of the excitation. The polygonal wear, however, yields high frequency variations in the bending stress. The magnitude of this high frequency stress is subsequently obtained by subtracting the steady state stress from the total bending stress, as shown in Figure 3.11(b). The results show that wheel polygonalization-induced wheel/rail contact forces yield notable magnitude of high frequency bending stress in the axle shaft, which can adversely affect fatigue life of the wheelset.
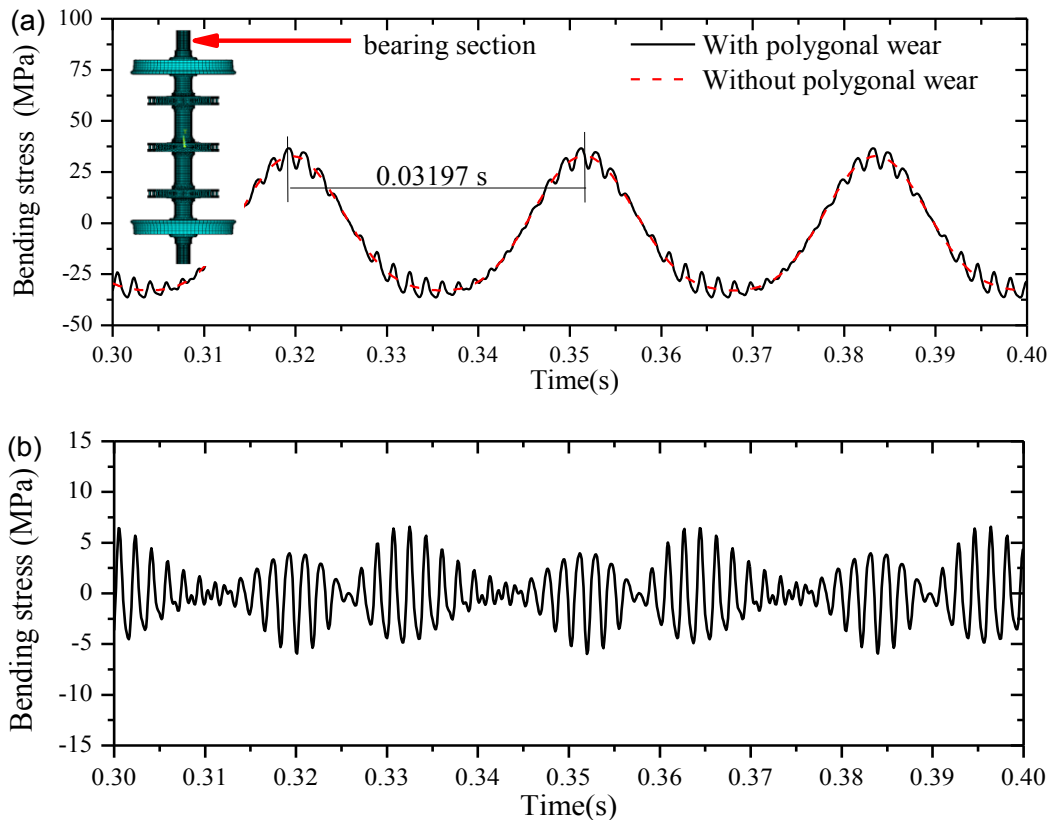
Figure 3.11: (a) Comparison of bending stresses developed in the axle shaft with and without the excitation due to 18th-order wheel polygonalization; and (b) variation in bending stress with respect to the steady-state stress.

3.4.4 Influences of vehicle speed and wear amplitude

The wheel/rail contact force, axle box acceleration and axle shaft bending stress responses are strongly related to vehicle speed, and wear amplitude apart from the order of the polygonal wear. Figure 3.12 illustrates the effect of forward speed on the resulting maximum and minimum wheel/rail contact force magnitudes considering 0.1 *mm* amplitude 18th order polygonal wear on both the wheels of the leading wheelset. The results show relatively small magnitude peak at the speed of 30 *km/h*. The maximum and minimum contact forces at this speed show small bias. This is likely caused by the wheel/rail coupled vertical vibration mode near 60 *Hz*, as reported in [36,161]. This relatively low frequency mode is also referred to as 'P2 force' or 'P2 resonance' [80], and is related to effective masses of the wheelset and the rail, and stiffness of the primary suspension and the rail supports. In the 50-310 *km/h* speed range, the maxima of the contact force increase with vehicle speed. The maximum contact force tends to decrease at speeds exceeding 310 *km/h*. The minimum contact force at the wheel/rail contact decreases with increasing vehicle speed, with the exception of the peak at 30 *km/h*. The wheel/rail separation is evidenced at speeds exceeding 240 *km/h*, which contributes to more rapid increase in the maximum contact force in the 240-310 *km/h* range. This trend is also similar to that obtained in the presence of a wheel flat considering different vehicle speeds [12].
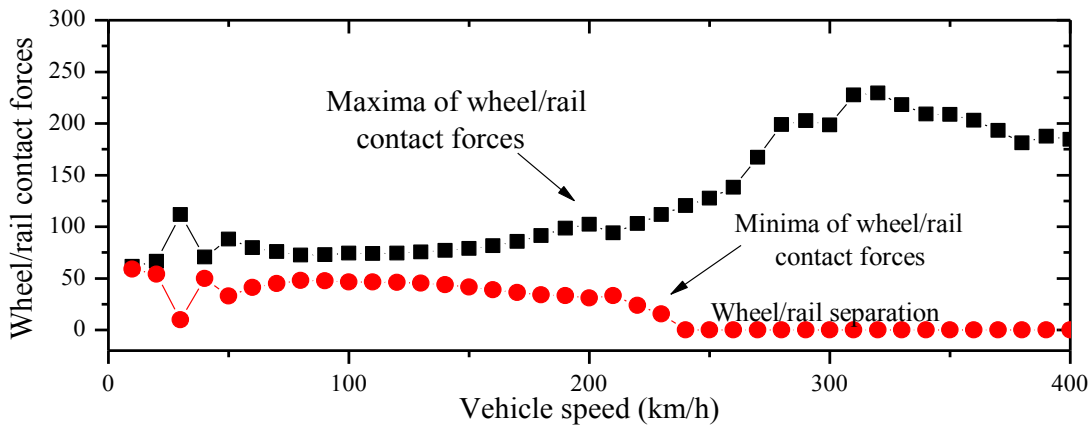
Figure 3.12: Influence of vehicle speed on the maximum and minimum wheel/rail contact force under 18th-order polygonal wear in both wheels of the leading wheelset (Amplitude=0.1 *mm*).

Apart from the forward speed, the magnitude of the wheel/rail contact force is strongly dependent on the amplitude of the polygonal wear. Figure 3.13 illustrates the effect of wear amplitude on maxima and minima of the wheel/rail contact force caused by the 18th-order

polygonal wear at the speed of 200 *km/h*. The results clearly show nearly linear increase and decrease in maximum and minimum contact force, respectively, with increasing wear amplitude up to 0.18 *mm*, when the wheel/rail separation initiates. The wheel/rail separation contributes to rapid increase in the maximum contact force as the wear amplitude exceeds 0.18 *mm*. Figures 3.14(a) and 3.14(b) further illustrate the influence of wear amplitude on the maximum and minimum contact forces, respectively, in the 10-400 *km/h* speed range. The results generally show trends similar to those observed for 0.1 *mm* wear amplitude in Fig. 3.13, while higher wear amplitudes yield substantially higher maximum contact force and wheel/rail separation at a relatively lower speed. Higher wheel wear amplitude thus adversely affects the critical speed of the vehicle at which wheel/rail separation may occur. Moreover, higher amplitude of polygonal wear leads to more pronounced effect of the coupled wheel/track vibration mode on the contact forces in the 30~50 *km/h* speed range.
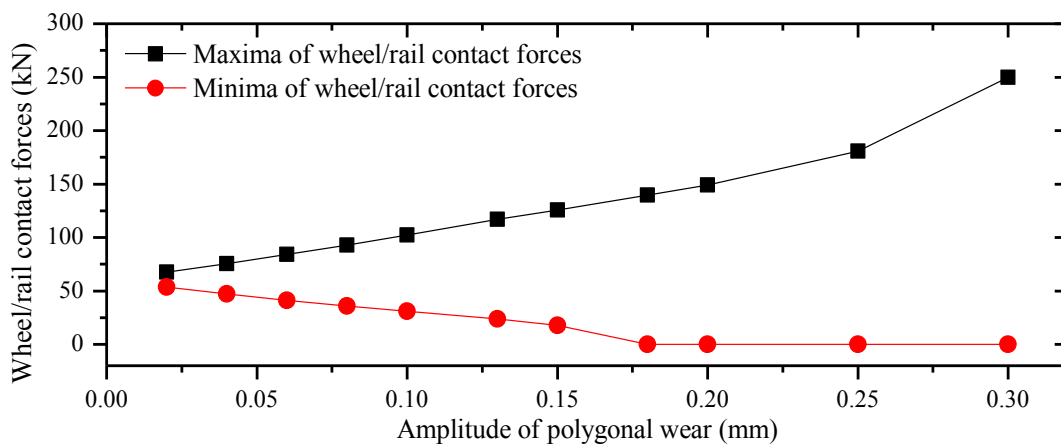
Figure 3.13: Influence of polygonal wear amplitude on the maxima and minima of the wheel/rail contact forces at the speed of 200 *km/h*.

Figure 3.15(a) illustrates the influence of variations in polygonal wear amplitude and vehicle speed on the peak axle box vertical acceleration response. The results show that greater wear amplitude yields considerably higher peak acceleration in the entire speed range. Higher polygonal wear, however, causes rapid increase in the peak acceleration around the speed of 210 *km/h*. For the 0.3 *mm* wear amplitude, the peak acceleration approaches 138 *g* at the speed of 210 *km/h*. The passing frequency of the 18th-order polygonal wear at 210 *km/h* is approximately 393 *Hz*, which is in the vicinity of the second bending mode frequency of the wheelset [29]. The large magnitude acceleration peak at 210 *km/h* is thus believed to be caused by the wheelset bending vibration mode.

Although the peak acceleration magnitude decreases with further increase in the vehicle speed, the higher wear amplitude cause substantial levels of axle box acceleration, especially in the 275-350 *km/h* speed range, which is due to wheel/rail separation and higher maximum impact force in this speed range (Fig. 3.14) together with deformations of the axle shaft.

Figure 3.15(b) illustrates the frequency spectra of the axle box acceleration for 0.1 *mm* amplitude 18th polygonal wear in the 100-400 *km/h* speed range. The results suggest that the passing frequency of wheel polygonalization (f_{oor}) increases with the vehicle speed and occurs in the 180-750 *Hz* frequency range. The spectra also revealed acceleration peaks corresponding to multiples of f_{oor}, namely, $2f_{oor}$, $3f_{oor}$ and $4f_{oor}$, for speeds above 250 *km/h*. These are likely due to wheel/rail separation-induced elastic deformations of the wheelset at higher speeds.
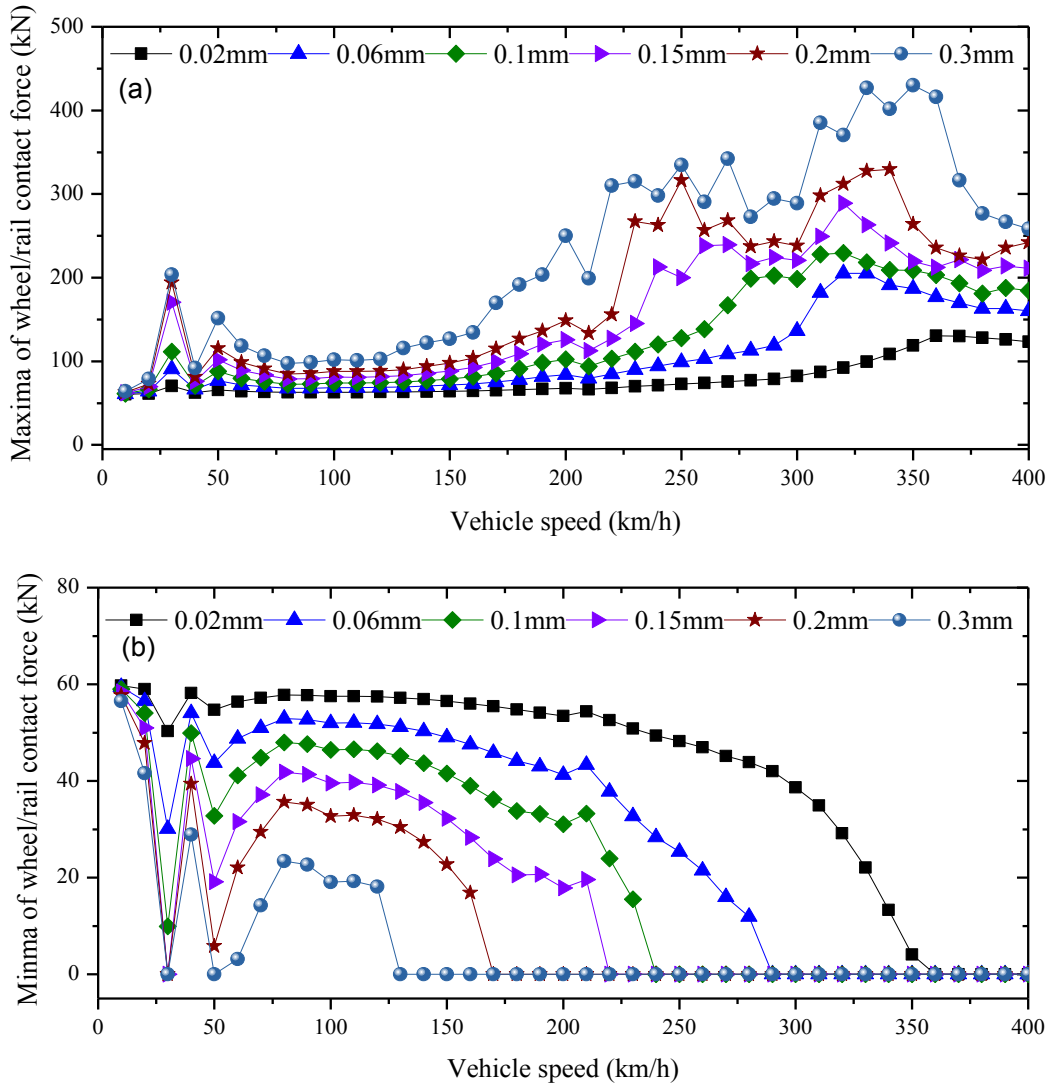
Figure 3.14: Influence of polygonal wear amplitude and forward speed on (a) maxima and (b) minima of the wheel/rail contact forces.
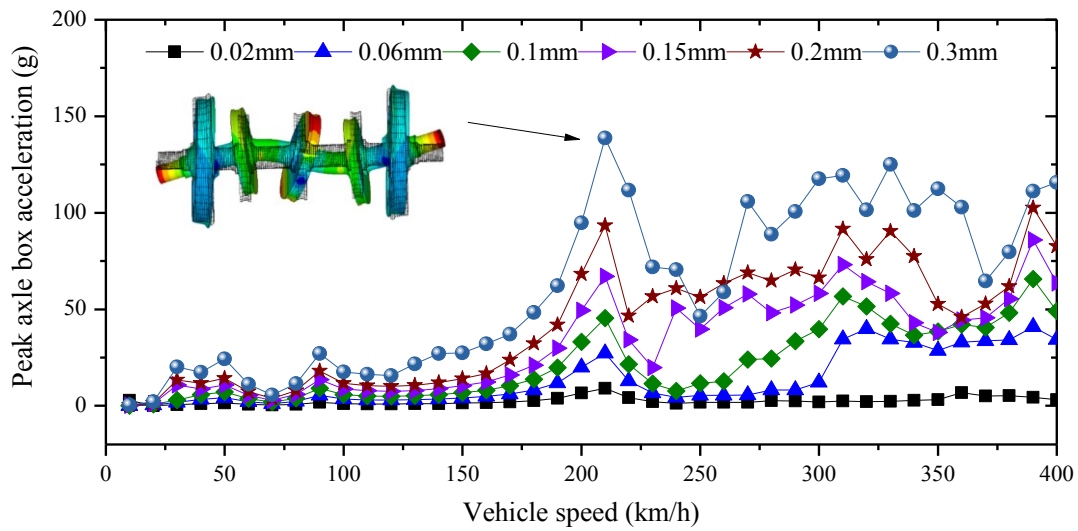
(a)
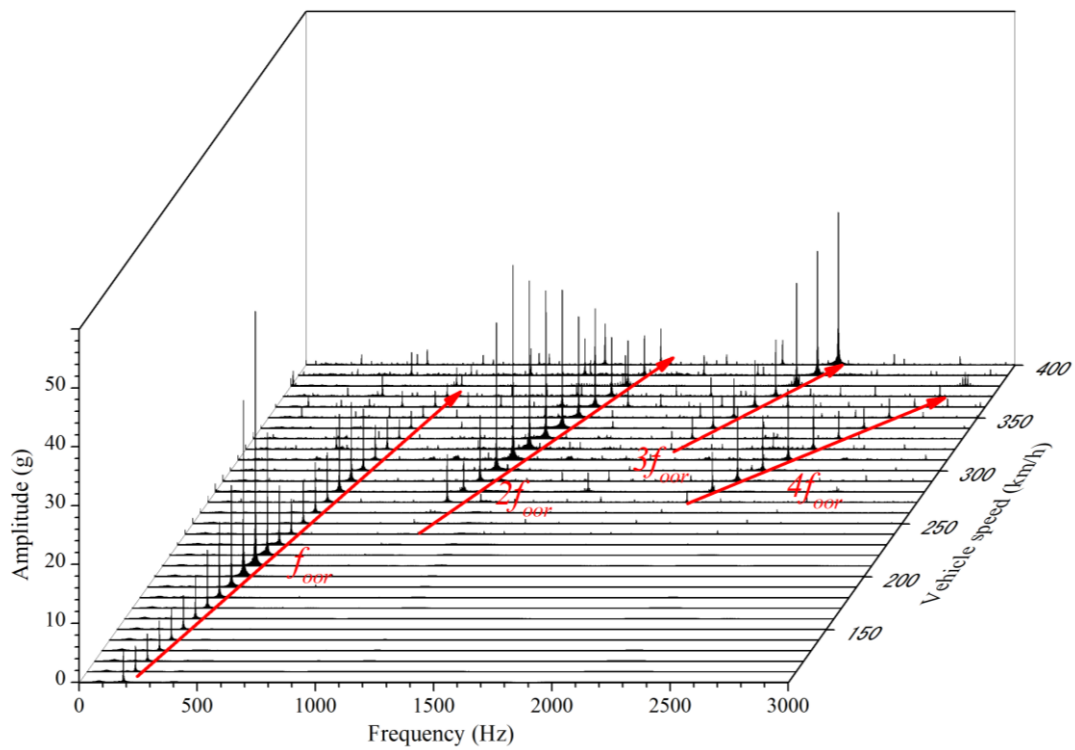
(b)

Figure 3.15: (a) Effect of vehicle speed and wear amplitude on the peak axle box acceleration; and (b) spectra of axle box acceleration in the 100-400 *km/h* speed range (Amplitude= 0.1 *mm*).

Figure 3.16 illustrates the effect of polygonal wear amplitude on the peak bending stress in the bearing section of the axle shaft in the 0-400 *km/h* speed range. The results show trends similar

to those in the axle box peak acceleration (Fig. 3.15(a)). The results show peak stress near the speed of 210 *km/h*, irrespective of the wear amplitude, as observed in the peak axle box acceleration. The peak stress at this speed is attributable to bending vibration mode of the wheelset axle (393 *Hz*) in the vicinity of the passing frequency of 18th order wheel polygonalization. The higher peak stress is also observed in the 270-350 *km/h* speed range, which is caused by the wheel/rail separation-induced high magnitude impact loads, as observed in Fig. 3.14.
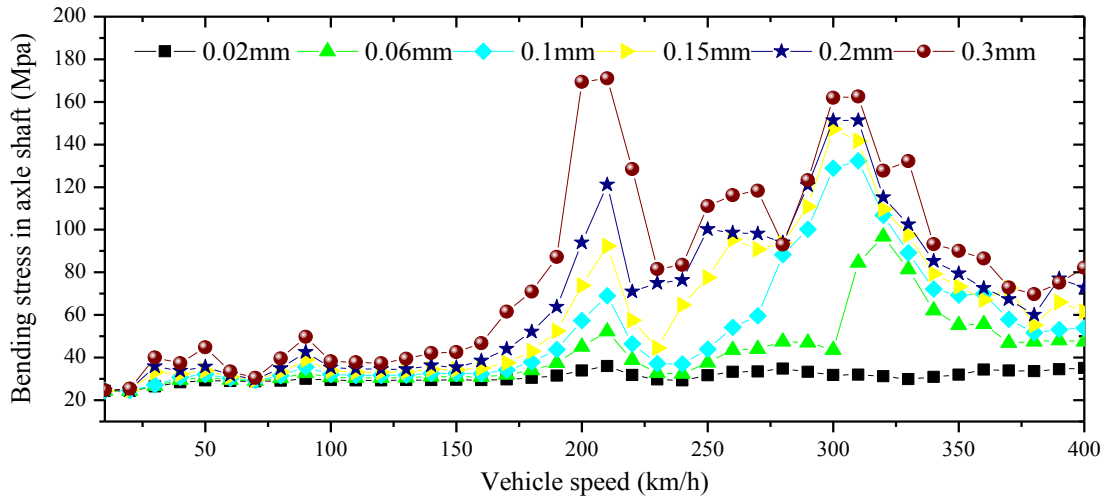
Figure 3.16: Effect of 18th-order polygonal wear amplitude on the peak bending stress developed in the bearing section of the axle shaft in the 0-400 *km/h* speed range.

3.4.5 Influence of order of the polygonal wear

Figure 3.17 illustrates the influence of order of the polygonal wear on the maxima and minima of the wheel-rail contact force in the 100-400 *km/h* speed range. The results are obtained for 0.1 *mm* wear amplitude on both wheels of the wheelset and the order ranging from 10 to 28. For the considered speed range, the maxima of the wheel/rail contact force increase with increasing order of the wear until the wheel/rail separation occurs. The order of polygonal wear corresponding to the peak contact force decreases with increasing speed. The results obtained at different speeds show maximum contact force near the passing frequency of 580 *Hz*, irrespective of the order and amplitude of the polygonal wear. This is likely due to a bending mode of the rail section between the two wheelsets, as reported in [162,163]. Saturation or only small variations in the maximum contact force are observed with further increase in the order of the polygonal wear, irrespective of the speed. This is due to separation of the wheel and the rail.
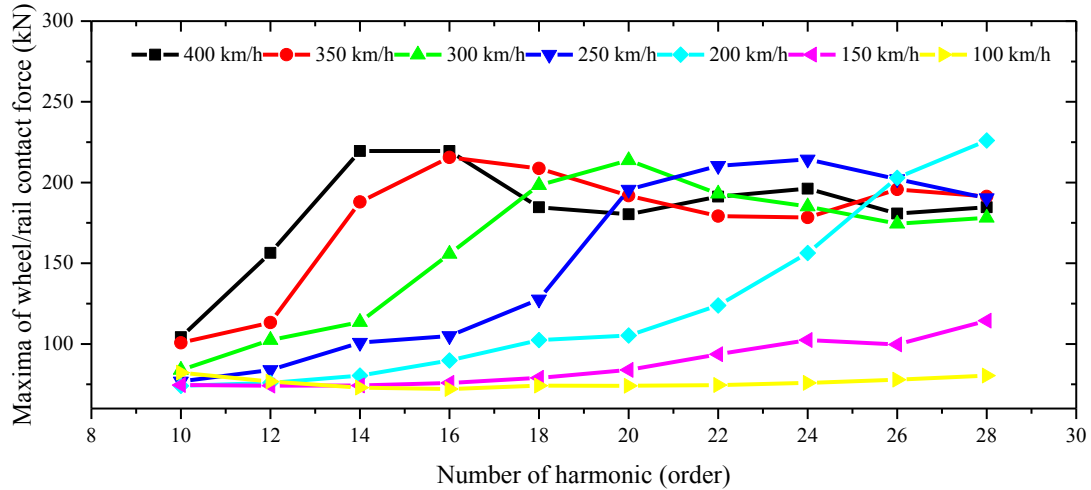
(a)
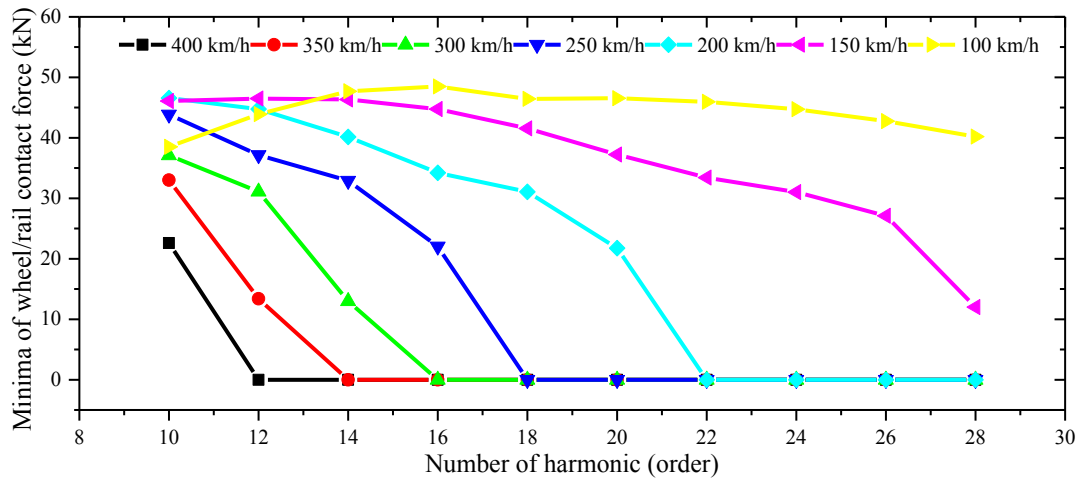
(b)

Figure 3.17: Effect of order of polygonal wear on (a) maxima and (b) minima of the wheel-rail contact force in the 100-400 *km/h* speed range (amplitude =0.1 *mm*).

3.5 Conclusions

The results suggest that the wheel polygonalization in high-speed operations can lead to substantially higher magnitudes of wheel-rail contact force and wheel-rail separation at relatively lower speeds. The impact loads caused by the affected wheels also contribute to higher contact forces to the adjacent wheels, which may lead to rapid growth in polygonal wear of the adjacent wheels. The wheel/rail separation-induced impacts together with elastic deformations of the wheelset and the flexible slab track contribute to high magnitudes of high frequency axle box acceleration and bending stress in the wheelset axle, which may adversely affect service life of the

wheelset. At the forward speed of 300 *km/h*, the peaks in the axle box acceleration and bending stress responses were evident near 562 *Hz*, the passing frequency of polygonal wear. Highest magnitudes of axle box acceleration and dynamic stress in the axle shaft were observed near the speed of 210 *km/h*, which was attributed to the corresponding passing frequency (393 *Hz*) in the vicinity of the second bending mode frequency of the wheelset. Apart from the passing frequency, the axle box acceleration peaks occurred near 2nd, 3rd and 4th multiples of the passing frequency at higher speeds, which were attributed to wheel/rail separation-induced elastic deformations of the wheelset at higher speeds. It is shown that magnitudes of the wheel-rail contact force and thereby the dynamic deformations of the wheelset and the rail are strongly dependent upon the vehicle speed, and amplitude and order of the polygonal wear. The results obtained at different speeds showed maximum contact force near the passing frequency of about 580 *Hz*, irrespective of the order and amplitude of the polygonal wear. This was attributed to a bending mode of the rail section between the two wheelsets.

CHAPTER 4: A STUDY OF POLYGONAL WHEEL WEAR THROUGH A FIELD TEST PROGRAM

4.1 Introduction

The earlies studies [30-33,68] have invariably suggested highly adverse effects of high-order wheel polygonalization on the vehicle and the track system. These have shown that the adverse effects of polygonal wheel wear are strongly related to the vehicle speed, and amplitude and harmonic order of the wheel polygonal wear. The reported studies, however, have been mostly limited to lower speeds. The results presented in Chapter 3 also illustrate similar trends, while the magnitudes of contact forces were substantially higher at higher operating speeds, in the order of 300 *km/h*. The reliability of the simulation results, however, strongly relies on accurate characterization of the wheel wear patterns. It is thus desirable to characterize the high-order wheel polygonalization and resulting dynamic responses through experimental measurements.

This Chapter presents the results obtained from a six months long field measurement campaign of a typical high-speed rail car. The selected test car, travelling on Wu-Guang (Wuhan-Guangzhou) high-speed railway line at a nominal speed of 300 *km/h*, has reported frequent loosening of bolts and failures of structural components, which are believed to be caused by the wheel polygonalization-induced high frequency dynamic loads. The test program thus included continuous measurements of the axle box vibration, apart from monitoring of the wheel irregularities. The wheel profiles were repeatedly measured during the campaign, whenever an opportunity existed. The data, acquired during the campaign, were analyzed to define patterns of wheel wear, rate of growth of polygonal wear and its correlation with the axle box acceleration response.

4.2 Field Test Program

4.2.1 Brief description of the test car

Operators of high-speed railways have reported frequent service failures of various components including bolt fractures in the axle box and cracks in the gearbox apart from loosening of the bolted connections. These have been believed to be caused by high frequency components of impact loads due to high-order polygonal wear of the wheels. A long-term field test program was undertaken on a high-speed train to gain an understanding of evolution and patterns of wheel wear, and its impact

on the resulting axle box acceleration. The field measurements were conducted on the 1069 *km* long Wu-Guang (Wuhan-Guangzhou) high-speed railway line with 17 railway depots, as shown in Figure 4.1. The line represents the earliest high-speed slab track design in China. The nominal operating speed of the train on this line is 300 *km/h*.

Figure 4.1: The 1069 *km* long Wu-Guang high speed railway line comprising the slab track.

The high speed train operating on this particular line was considered for the study due to frequently reported failures of bolts on the axle box. Preliminary examinations of the wheel irregularities suggested presence of notable wear around the circumference, which could be characterized by 18th-order harmonic variation. It was speculated that the axle box bolt failures might be caused by high magnitude and high frequency vibration of the axle box attributed to high frequency excitations (wheel-rail contact forces) arising from interactions of the polygonal wheel and the rail. The long-term field test program was motivated by the need to gain a better understanding of development of the high-order wheel polygonalization and the resulting influences on the axle box responses.
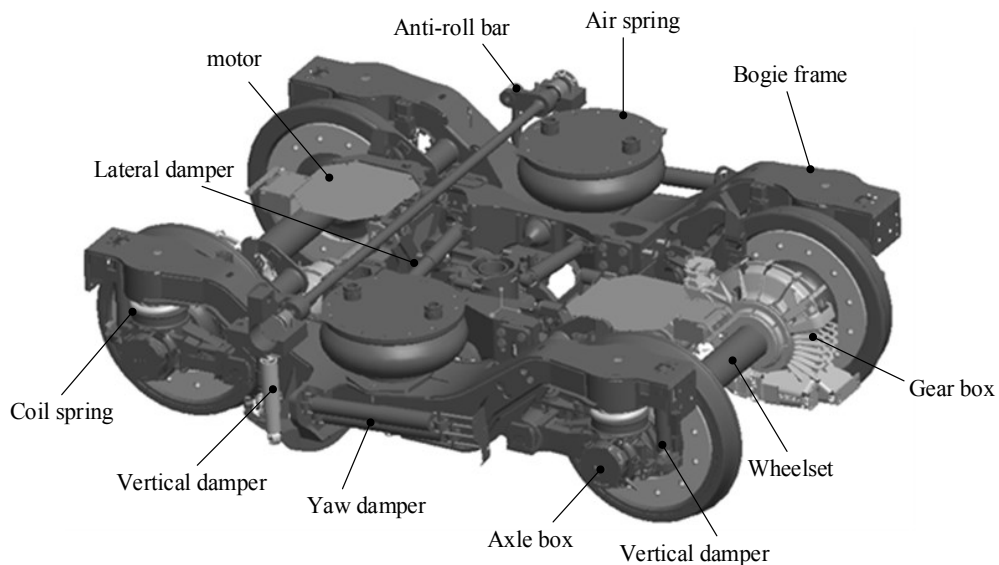
Figure 4.2: A pictorial view of the motor bogie employed in the selected test car.

The vibration response of the axle box of the last wheelset of the leading car (car # 1) was measured. The leading car comprised two motor bogies with pneumatic secondary suspension. The suspension system for each bogie included two vertical air bags and dampers, an anti-roll bar, two lateral dampers and four yaw dampers. Two motors were mounted on each bogie frame in a diagonal arrangement via elastic mounts, and coupled to the wheelset through gear boxes, as shown in Figure 4.2. The bogie frame was coupled with two wheelsets through vertical dampers and coil springs. Two axle boxes, mounted at the ends of each wheelset, were also integrated to the bogie frame via elastic mounts in the longitudinal direction.

4.2.2 Test Methods

Prior to the six months long measurement campaign, the wheels of the entire train were re-profiled so as to monitor the evolution of polygonal wear of the wheels during service. The usage history of the wheels of the leading car was also acquired from the operator, which revealed that the wheels had been in service for about 3200 *Mm* before the field tests. The radii of the wheels of this car ranged from 0.415 *m* to 0.455 *m*, with mean radius of 0.433 *m* compared to the nominal radius of 0.46 *m* for the new wheels. The noise emitted in the car was continuously monitored and the wheels were re-profiled when the noise level exceeded 80 *dB*. During the measurement period, the wheels of the leading car underwent additional re-profiling 3 times. The spans of service between successive re-profiling were 56, 19 and 82 days, which corresponding to 98, 33 and 130 *Mm* of service, respectively (Table 4.1). Apart from this, the wheels of all the cars were re-profiled twice during the measurement period after the service spans of 75 and 82 days, which corresponded to 131 and 130 *Mm* of service, respectively.

Attempts were made to measure the wheel profiles at frequent intervals. This was, however, not possible since the operator did not permit service interruptions. The wheels' surface profiles were thus measured whenever an opportunity arose. Apart from the initial measurements of the profiles, the measurements were performed after 88, 98 and 131 *Mm* of service during the first re-profiling cycle (with the exception of the leading car wheels, which were re-profiled after 98 *Mm* of service). The measurements were also obtained after 14, 19, 67, 87 and 130 *Mm* of service during the third re-profiling cycle (second cycle for the entire train wheels). The measurements during the second cycle of re-profiling were conducted after 33 *Mm* of service. A total of 586 wheel profile measurements were thus acquired during the field test program. Table 4.1 summarizes the intervals between different wheel-profiling and measurements during the campaign, while the re-profiling

cycle refers to that for the leading car wheels. The wheel profiles were measured using the BBM wheel roughness measuring device (Muller-BBM GMBH) at the rolling circle of the wheel with 0.1 μm accuracy, as shown in Fig. 4.3. The data were acquired over the wheel circumference with a resolution of 1 mm.

Figure 4.3: The BBM wheel roughness measuring device.

Table 4.1: Wheels' re-profiling and roughness measurements performed during the field tests.

Wheel re-profiling (month/day)	1st cycle (07/04 to 08/29)			2nd cycle (08/30 to 09/20)	3rd cycle (09/20 to 12/22)					
Wheels of car(s)	1-8			1	1-8					
Wheel Profile Measurements										
Date (month-day)	7-4	8-20	8-30	9-19*	9-19	10-8	10-25	11-9	11-27	12-22
Number of days after re-profiling	0	46	56	75*	19†	8	16	39	57	82
Mileage after re-profiling (*Mm*)	0	88	98	131*	33†	14	19	67	87	130
Mean wheel radius, car 1 (*m*)#	.435	-	-	-	0.431	0.428	-	-	-	-

*Measurements include re-profiled wheels of car 1 (2nd cycle) and initially profiled wheels of cars 2 to 8 (first cycle); †number of service days and mileage after second re-profiling of wheels of car 1 alone; # mean radius of the leading car's wheels measured after re-profiling.

Apart from the wheels' profiles, the acceleration response of the axle box mounted on left-hand side of the last wheelset of the leading car was acquired continuously during the test program. For this purpose, a single-axis accelerometer (B&K 4507) was mounted on the axle box to measure its acceleration along the vertical axis. The measurements were limited to vertical axis alone since it has shown good correlation with the wheel-rail impact force in the presence of a wheel defect [29]. The accelerometer signal was acquired in the on-board data acquisition system (HBM Inc., Model: Somat eDAQ) at a sampling rate of 5000 *Hz*. The forward speed of the train was also recorded in the HBM data acquisition using the GPS signal.

4.2.3 Data Analysis

The wheel surface irregularities data acquired during the 6 months long campaign were analyzed to identify the order of wheel polygonalization and its growth. The vertical axle box acceleration data were analyzed in both the time- and frequency-domains to study a relationship between the acceleration, and the magnitude and order of the polygonal wheel wear. The wheel roughness data, acquired as a function of the wheel circumference coordinate, *x*, was analyzed to determine the wheel surface waviness or pattern. The mean radius of each wheel R_0 was obtained from the measured circumference. The discrete Fourier transform (DFT) of the data acquired for each wheel was performed with a spatial frequency resolution of $1/2\pi R_0$ and bandwidth of 0.5 *cycle/mm*. The spectrum of roughness of each wheel was expressed in terms of its harmonic order, $\theta = 2\pi R_0 \Omega$, up to order 30, where Ω is the spatial frequency. The root mean square (*rms*) roughness of the wheel corresponding to each harmonic order was also expressed in terms of dB considering the reference value of 1 *μm* [22], such that:

$$L_\theta = 10log_{10}\{\tilde{r}_\theta{}^2\} \tag{1}$$

Where $\tilde{r}_\theta$ is *rms* value of the wheel surface roughness corresponding to the order θ and L_θ is roughness in dB.

The axle box acceleration data, acquired during a 16.8 *km* long tangent run between two consecutive depots during each south-bound run, were extracted for the analysis. The duration of the extracted data was nearly 200 *s*. The data were analyzed in both the time- and frequency-domains to study correlations between the wheel wear and the axle box acceleration. The data, acquired, during the first and initial portion of the second re-profiling cycle alone were considered for the analyses, since the accelerometer cable connector was found to be damaged towards the end

of the second cycle, likely due to very high magnitude acceleration. In the time-domain, the moving *rms* values of acceleration were evaluated considering windows of 2 *s* duration. The *rms* acceleration response of the axle box was subsequently quantified considering probability of 99.85% from the cumulative probability distribution of the moving *rms* data. The spectral components of the acceleration signal were also evaluated via FFT of the data. The FFT was obtained for each 2 *s* window of the data, which were subsequently averaged to represent frequency spectrum of the axle box acceleration response.

4.3 Results and discussions

4.3.1 Identifications of polygonal wear and dominant harmonic orders

The initial measurements of wheels' surface irregularities prior to the measurement campaign revealed notable irregularities of 1st and 3rd harmonic orders, which is likely caused by fixed clamping during re-profiling, as reported by Rode [21]. The roughness corresponding to the first harmonic order ranged from a low value of 5 *dB* to as high as 23 *dB*, while that of the 3rd order varied from -5 to 23 *dB*. The magnitudes of roughness of orders above three were very small.

Owing to the high noise level in the first and last cars, the irregularities in surfaces of all the wheels were measured after 88 *Mm* of service following the initial re-profiling process (Table 4.1). The wheel surface data, acquired for the wheels were analyzed to identify the order of polygonal wear and growth in the wheel wear. Considerable growth in higher-order surface wear of the wheels was observed through comparisons of wheel profiles with the initial profiles. As an example, Figure 4.4(a) compares the roughness profile of left wheel of the last wheelset of the leading car (# 1) measured after 88 *Mm* of service with the initial profile over the entire wheel circumference. The spectra of the roughness are further compared in Fig. 4.4(b). It is evident that the maximum roughness of the wheel after the initial profiling is about 5 *dB* occurring near the 2nd harmonic order. The results show substantial growth in roughness amplitudes near the 1st and 18th harmonic orders after 88 *Mm* of service. The respective roughness amplitudes corresponding to these orders are 26.8 *dB* and 30.5 *dB*.

The dominance near the 1st and 18th harmonic orders were also observed for all the wheels. Figure 4.5(a) compares the spectra of surface variations of wheels of the first and last (car # 8) cars together with the mean spectrum (indicated by the bold line). The results show that irregularities of most of the wheels predominate within the 17th to 19th harmonic orders, apart from the 1st

harmonic order. Three of the wheels also showed dominant surface variations near the 10th order, while the peak irregularity of 9th order was observed for one of the wheels. Figure 4.5(b) presents box plot of variations in roughness of the wheels. Apart from the 1st order, the peak wear amplitudes occurred in the 17th to 19th orders, which contributed to substantial standard deviations of high-order wheel wear. The results show mean roughness of 22 *dB* and 14 *dB* corresponding to the 1st and 18th harmonic orders, respectively, with standard deviations of 4.8 *dB* and 11.7 *dB*. The polygonal wear of the wheels could thus be characterized by a combination of the 1st and a higher order harmonic function, ranging from 17th to 19th. The fundamental order for the nominal speed of 300 *km/h* corresponds to about 31 *Hz*. The wear in the 17th to 19th orders could thus yield high frequency wheel-rail contact forces and excite wheelset and rail bending modes [33,163,164].
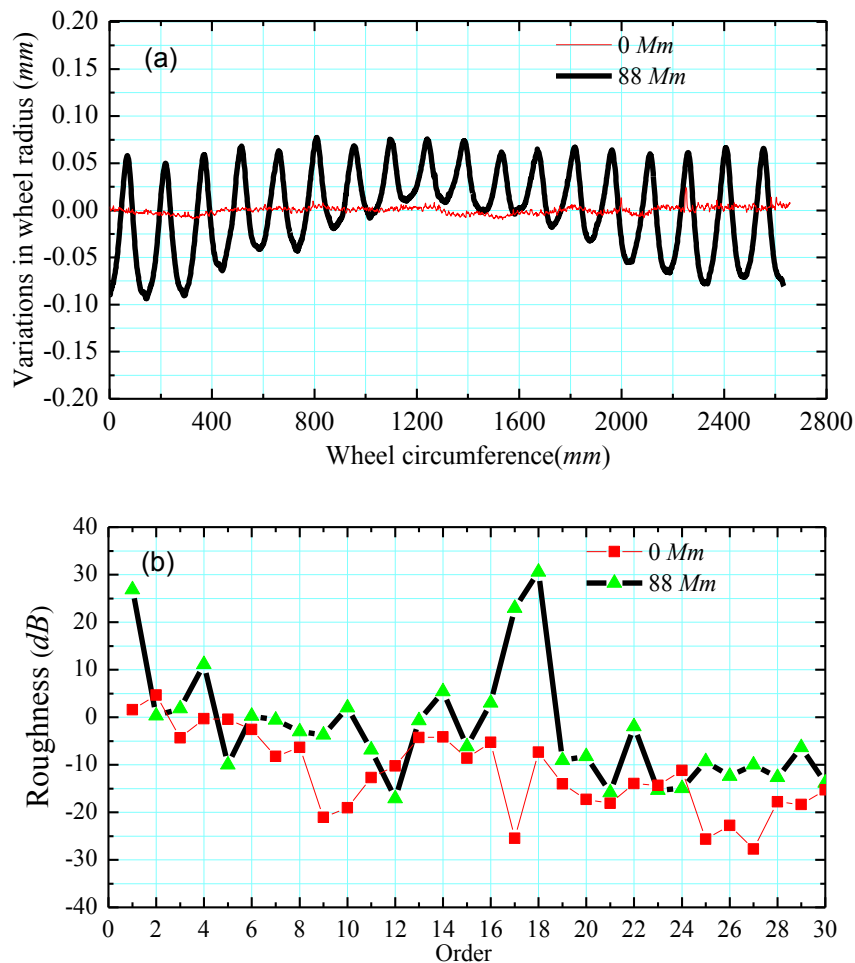
Figure 4.4: Comparison of irregularities of left wheel of last wheelset of the leading car obtained after initial re-profiling and after 88 *Mm* service: (a) wheel irregularities in the spatial coordinate; and (b) roughness as a function of the harmonic order.
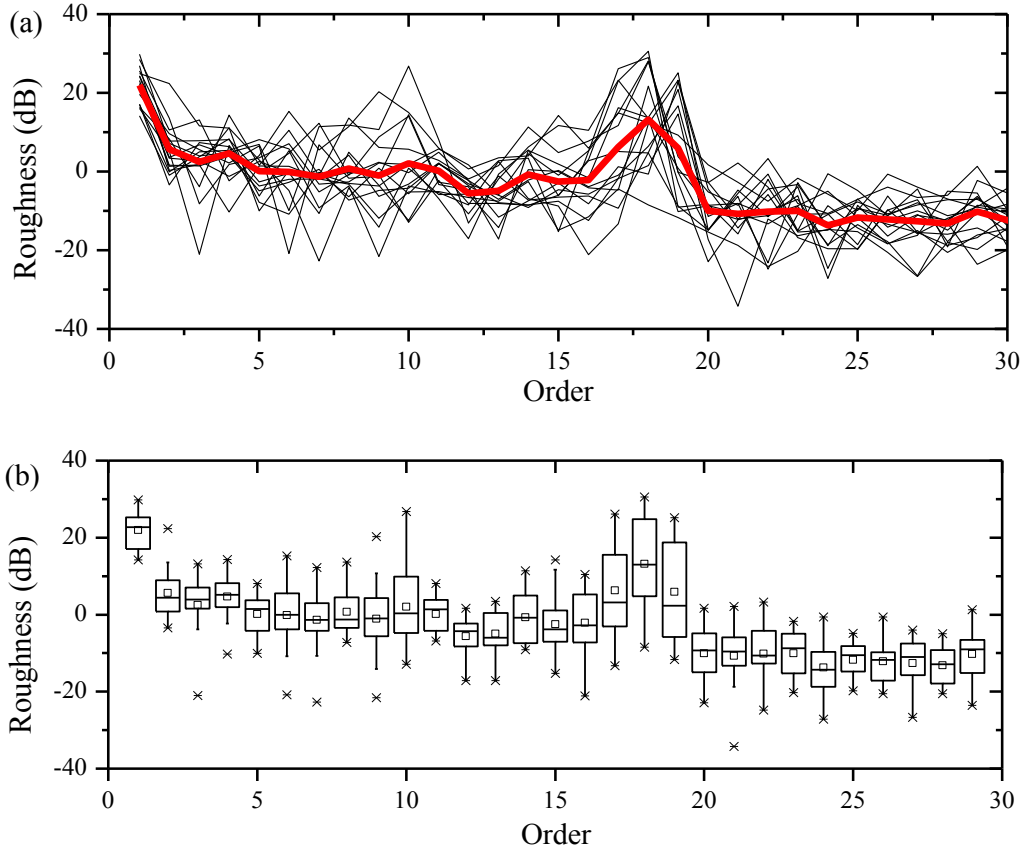
Figure 4.5: (a) Comparisons of spectra of roughness of wheels of the first and last cars, and the mean spectrum; and (b) box plot of wheels' roughness corresponding to different harmonic orders.

A few studies have also reported high-order polygonal wear of the railway wheels. For instance, Jin *et al.* [30] reported 9th order wear in wheels of subway cars that operate at a considerably lower speed, which was attributed to first bending mode of the wheelset. Chen [68] observed the presence of 20th-order polygonal wear in wheels of a high-speed train, while Wu *et al.* [34] measured polygonal wheel wear dominant near 14th and 23rd-orders, apart from the 1st order, in a train operating at a nominal speed of 250 *km/h*.

The variations in roughness of the left- and right-side wheels of the entire train are further investigated to study correlation between them, if any. Figures 5.6(a) and 5.6(b) illustrate box plots of roughness of the left- and right-wheels, respectively. The results show comparable levels of roughness of the left- as well as right-wheels, which predominate near the 1st and 18th harmonic orders. The results suggest comparable degree of polygonalization of the left- and right- wheels, which is evident from good correlation shown in Fig. 5.6(c) with correlation coefficient, r^2=0.97.
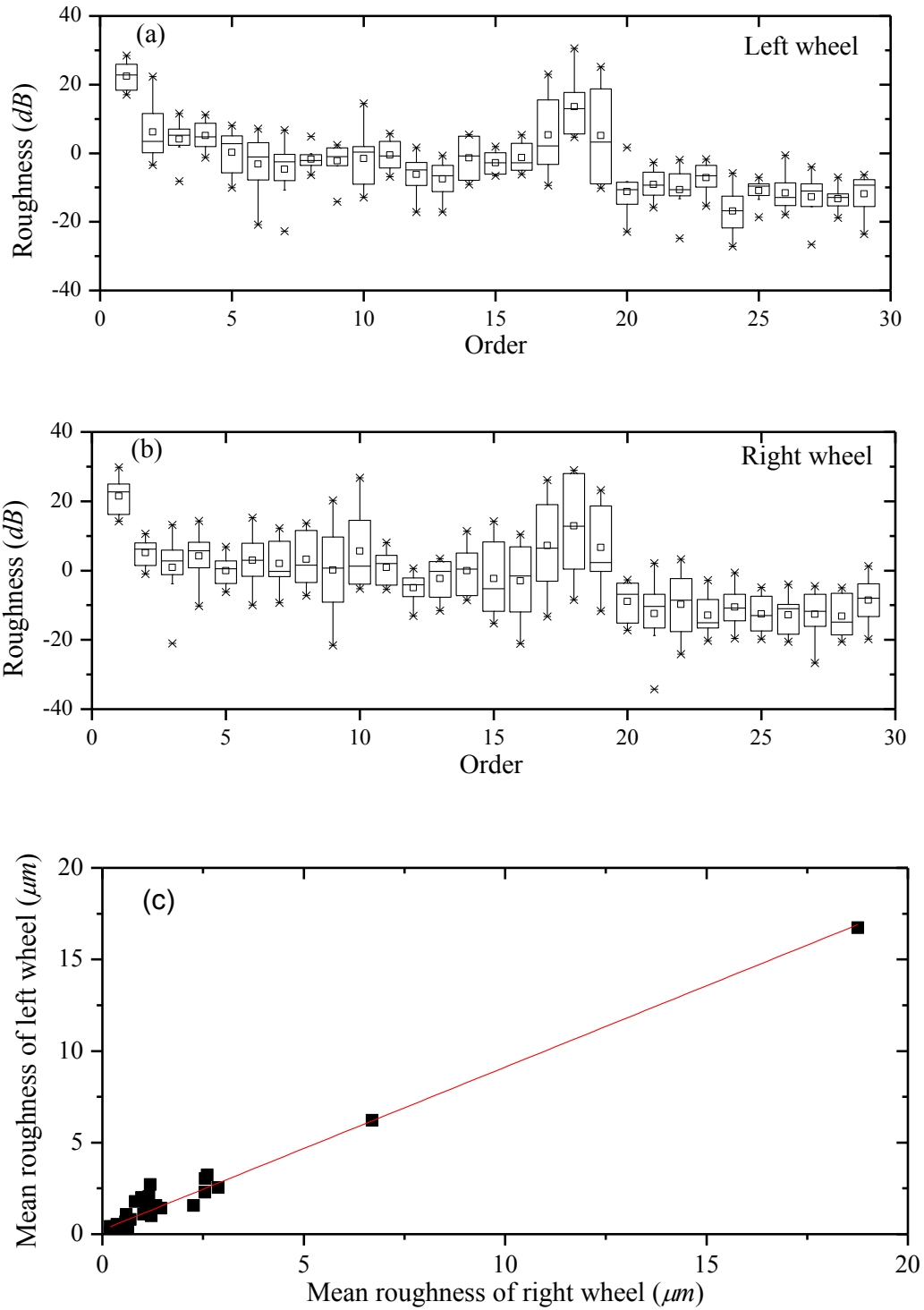
Figure 4.6: (a, b) Box plots of spectra of roughness of the left- and right- wheels, and (c) correlation between mean roughness of the left- and right-wheels.

4.3.2 Progression of polygonal wheel wear

The data acquired for the first and last cars are analyzed to evaluate progression of the polygonal wear magnitude. For this purpose, changes in the roughness magnitudes of selected wheels corresponding to different harmonic orders were examined with increasing service mileage. As an example, Figures 4.7 illustrates variations in roughness magnitudes of left wheel of the last wheelset of the last car (car # 8). The results are presented to illustrate variations in wheel roughness during the initial re-profiling cycle, involving measurements after 88 and 131 *Mm* in addition to the initial measurement, and during the third cycle with measurements after 14, 66, 86 and 130 *Mm*. The results are limited only to magnitudes corresponding to 1st, 3rd, 10th, 17th, 18th and 19th harmonic orders, where the variations were notable.
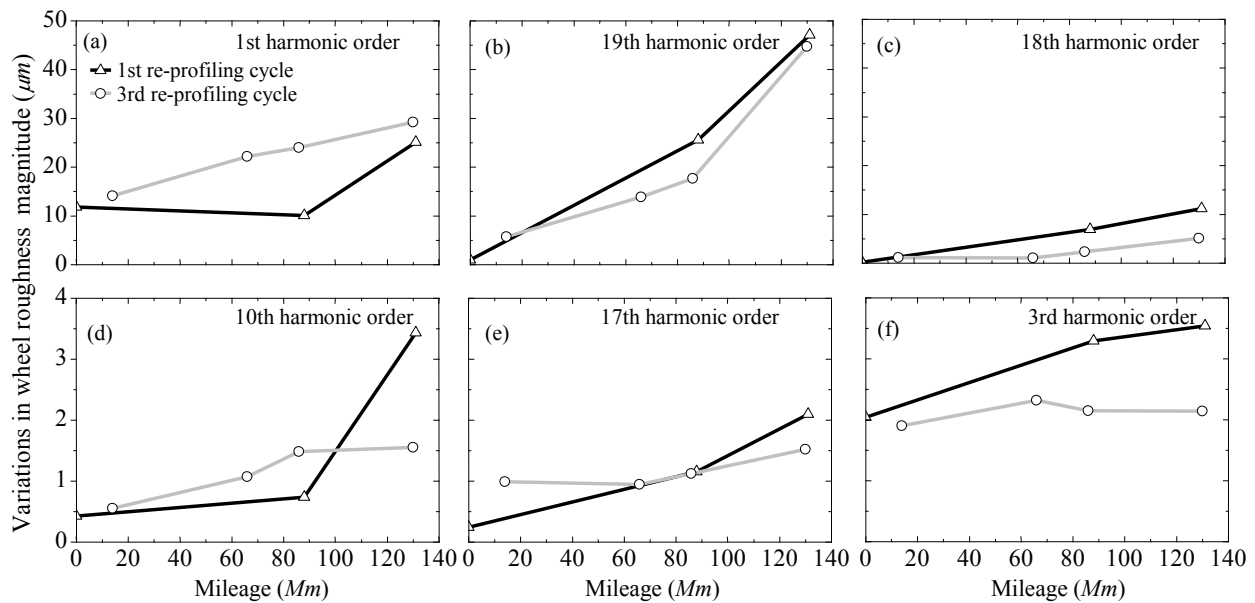
Figure 4.7: Variations in roughness magnitudes of left wheel of the last wheelset of the last car (car #8) corresponding to different harmonic orders: (a) 1st order; (b) 19th order; (c) 18th order; (d) 10th order; (e) 17th order; and (f) 3rd order.

The results show substantial growth in the wear magnitude corresponding to the 1st and 19th harmonic orders, while those corresponding to the 3rd, 10th, and 17th orders remain very small (below 4μm). The results generally show increase in wear magnitudes with increasing service mileage, and comparable trends during both cycles of measurements. Greatest growth is observed in the 19th order during both the measurement cycles. The wear magnitude corresponding to this order increased from less than 1 μm to nearly 47 μm during the first cycle, and from 5.7 μm *to* 44.7 μm in the third cycle. The results also show greater rate of growth after 88 *Mm* of service, which

ranges from 0.5 to 0.6 *μm/Mm* and is likely caused by intensified interactions between the polygonal wheel and the rail. This is followed by the growth in magnitude of wear corresponding to the 1st harmonic order (from 11.8 *μm* to *25 μm* in the first cycle and from 14 *μm* to 29 *μm* in the third cycle). The growth in magnitude of wheel roughness corresponding to the 18th harmonic order is observed to be relatively small compared to those of the 1st and 19th orders. The peak magnitudes increased nearly linearly to about 11 and 5 *μm* at rates of nearly 0.1 and 0.06 *μm/Mm* during the two cycles.
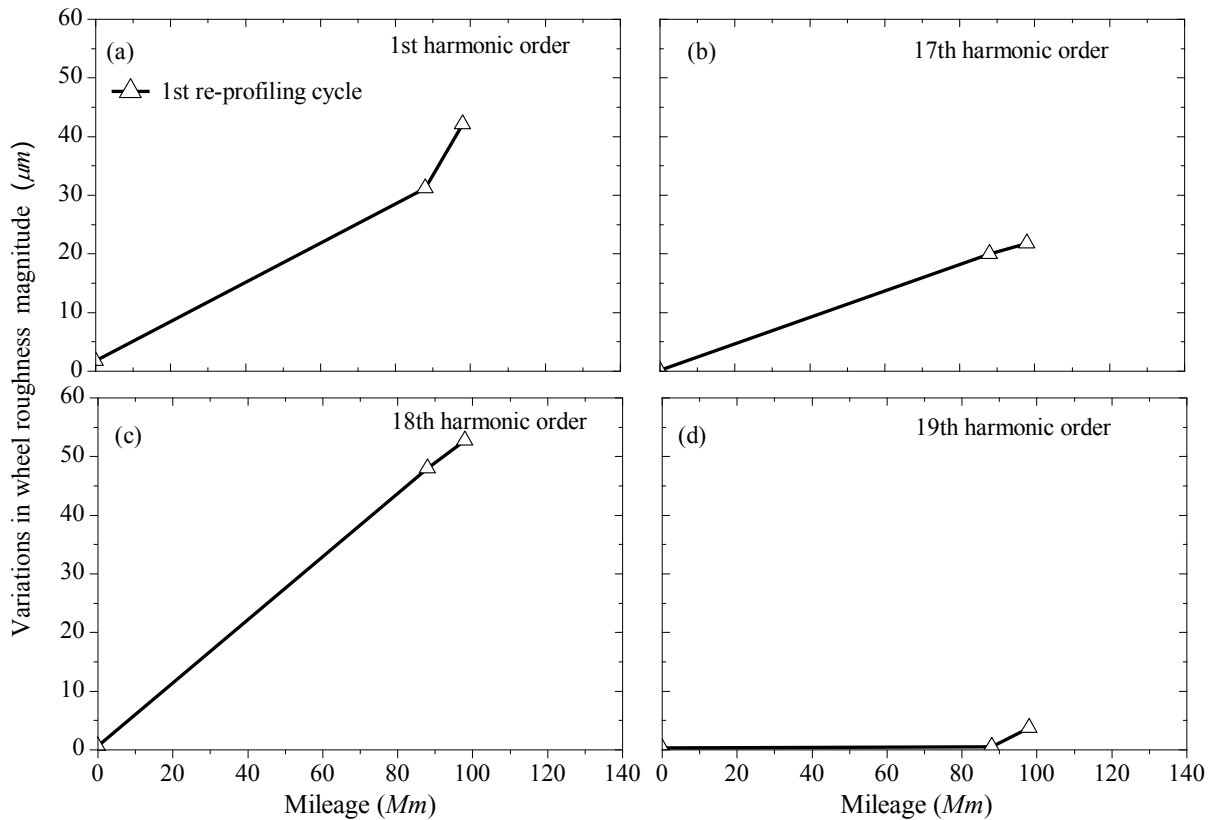
Figure 4.8: Variations in roughness magnitudes of left wheel of the last wheelset of the leading car (car #1) corresponding to different harmonic orders: (a) 1st order; (b) 17th order; (c) 18th order; and (d) 19th order.

A few studies have observed dominance of 18th order wear in wheels of the leading car of a high speed train [33], while the results obtained for the wheels of the last car in this study consistently showed strong dominance of the 19th harmonic order. This suggests that the harmonic order of the wear may vary slightly among the wheels of different cars. As an example, Figure 4.8 shows the changes in the 1st, 17th, 18th and 19th order wear magnitudes of the left wheel of last wheelset of the leading car measured during the first cycle. Unlike the last car's wheel, the results

for the leading car show significant growth in wear magnitude corresponding to the 18th order. The results show more rapid growth in 1st and 18th order wear magnitudes (0.43 and 0.54 $\mu m/Mm$, respectively) over the entire range of service mileage. The growth in the 19th order wear magnitude is negligibly small as seen in the figure. The magnitudes of 3rd and 10th order wear were also very small as observed in Fig. 4.7. The increase in 17th order wear magnitude is also notably higher (0.22 $\mu m/Mm$) compared to that observed for the last car's wheel.

The results in Figures 4.7 and 4.8 suggest that polygonal wear of wheels of the leading and last cars can be characterized by a combination of 1st and either 18th or 19th harmonic orders. The roughness data acquired for all the wheels of the train during all the profiling cycles are further analyzed to evaluate relative dominance of the 18th and 19th orders. The measurements also revealed considerable variations in the wheels' radii. It has been shown that hardness of the wheel material may decrease as the wheel radius decreases due to re-profiling [71], which may cause variations in the rate of wear. The data acquired for new or close to new wheels with radius exceeding 435 mm were thus excluded from the analyses. This was the case for 176 wheels of the 586 measurements. Figure 4.9 illustrates variations in roughness magnitudes of the remaining 410 wheels corresponding to the 1st, 18th and 19th harmonic orders in terms of box plots. The maximum values of roughness are limited to 99% probability. The results generally show increase in roughness magnitude corresponding to all the three orders with increasing mileage. Although the wheels after re-profiling revealed considerable roughness magnitudes corresponding the fundamental order (up to 18 μm), the 18th and 19th order roughness magnitudes are either comparable or higher than that of the fundamental order after 131 Mm of service. The greatest growth in wear magnitude is obtained for the 18th harmonic order, while those of the 1st and 19th harmonic orders are lower and comparable. Assuming linear growth in wear magnitude, the rate of change in the maximum and mean magnitudes, dominated by the 18th harmonic order, are obtained as 0.46 and 0.23$\mu m/Mm$, respectively. The results also show higher rates of maximum wear magnitudes corresponding to all the three orders, as the service mileage exceeds 67 Mm.
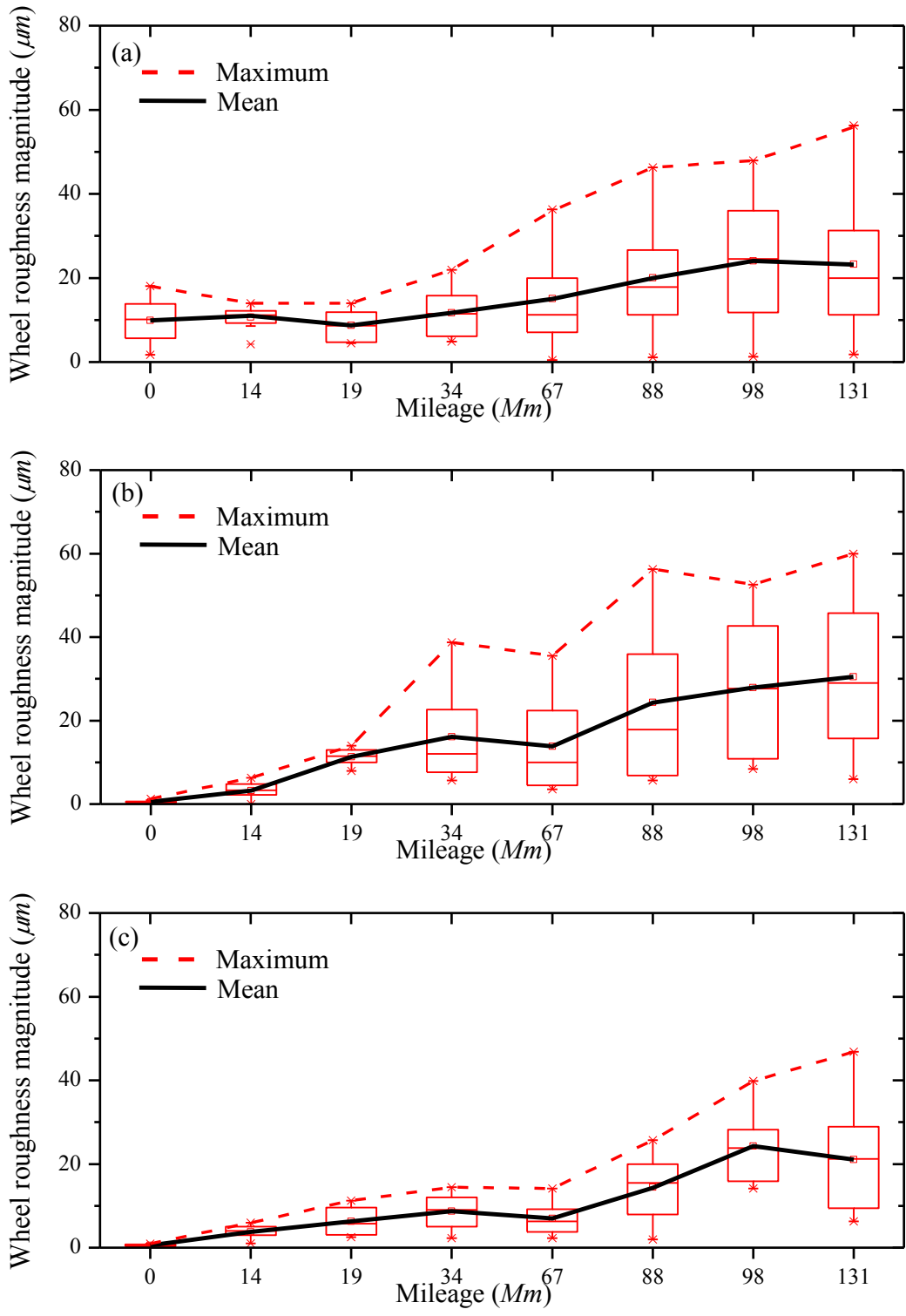
Figure 4.9: Boxplots showing variations in roughness magnitudes of wheels with radius less than 435 *mm* with the service mileage: (a) 1st harmonic order; (b) 18th harmonic order; and (c) 19th harmonic order.

4.3.3 Characterization of axle box acceleration

Figures 4.10(a) and 4.10(b) illustrate time-histories of vertical axle box acceleration measured at the end of the initial cycle (98 *Mm*) and immediately after second re-profiling of the leading car wheels (0 *Mm*) at the forward speed of *304 km/h*. The results clearly show significant effect of wheel polygonal wear on the acceleration response. After 98 *Mm* of service, the peak acceleration approaches nearly 500 *g*, which decreased to about 30 *g* after re-profiling. The axle box acceleration after re-profiling is due to irregularities of the track and roughness of the re-profiled wheels. The substantially higher acceleration at the end of the first cycle can be attributed to growth in the wear of the wheels corresponding to the 1st and 18th orders, shown in Fig. 4.8. The moving *rms* values obtained considering data windows of 2 *s* duration, presented in Fig. 4.10(c), show the mean values of about 54 *g* and 5.5 *g*, before and after re-profiling, respectively.
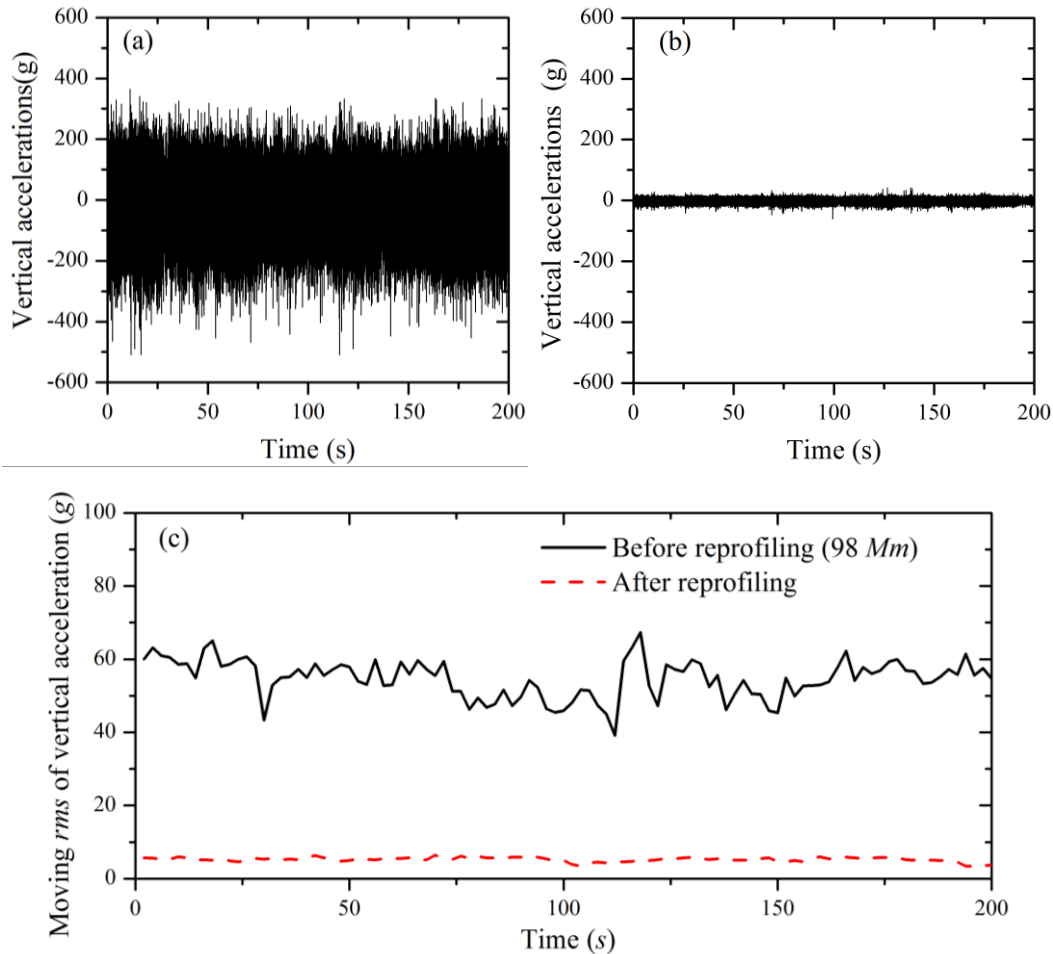
Figure 4.10: Time-histories and moving *rms* values of axle box vertical acceleration responses: (a) time history at the end of the first re-profiling cycle (98 *Mm*); (b) time history at the beginning of the second re-profiling cycle (0 *Mm*); and (c) moving *rms* acceleration.

The frequency spectra of the measured data are shown in Figures 4.11(a) and 4.11(b) in terms acceleration PSD in the 0-2000 Hz frequency range. These show substantially higher magnitude acceleration peaks prior to wheels' re-profiling when compared to that obtained after re-profiling. The data acquired before and after re-profiling, however, show comparable spectral components. The spectrum of acceleration measured at the end of the first re-profiling cycle exhibits dominant peaks near 540.2, 571.8 and 603.5 Hz, which correspond to excitations of the 17th, 18th and 19th orders of the fundamental wheel rotation frequency of 31.7 Hz. The figure also shows the spectra zoomed over the 500-600 Hz frequency ranges. The results also show peaks near the second and third multiples of the dominant frequencies, namely, 1112.2, 1144, 1175.3, 1683.5, 1716 and 1747.2 Hz. Relatively smaller magnitude peaks are also observed near 88.7 and 317 Hz, which correspond to approximately 3rd and 10th harmonic orders. Moreover, the frequency of the first peak, near 88.7 Hz, is close to the first bending mode of the wheelset [29].

The high acceleration magnitudes in the 540 to 603 Hz range are attributed to high frequency components of interactions of the wheels with high-order polygonal wear with the rail, which can excite bending modes of the rail and the wheelsets. A few studies have reported bending mode of the rail between the two wheelsets near 570 Hz, which plays an important role in the formation of rail corrugation [165,113,164,163]. The bending modes of the wheelset in the vertical and fore-aft planes have been reported to occur at 536.5 Hz and 586.7 Hz, respectively, which could contribute to high magnitude acceleration of the axle box in the 500 ~ 600 Hz frequency range [29]. Wu and Thompson [163] reported bending mode of the rail section between the two consecutive sleepers near 1100 Hz, which may contribute to high acceleration response near the second multiples of the dominant harmonic orders of polygonal wear.

The spectrum of the axle box acceleration following the wheels' re-profiling also exhibits dominate peaks near 90, 549 and 581 Hz. These correspond to about 3rd, 17th and 18th orders of the fundamental wheel rotation frequency, which increased to about 32 Hz in this case due to reduced wheel radius. The peak magnitudes at these frequencies are substantially smaller than those observed prior to re-profiling. These acceleration peaks are believed to be attributed to two factors: (i) residual wheel roughness corresponding to these orders after re-profiling, although of small magnitudes [76]; and (ii) bending modes of the rail and the wheelset, as discussed above. The spectrum also shows additional peaks and in the vicinity of 1162 Hz, corresponding to the second

multiple of dominate frequency, which is also close bending mode of the rail between the two sleepers [27].
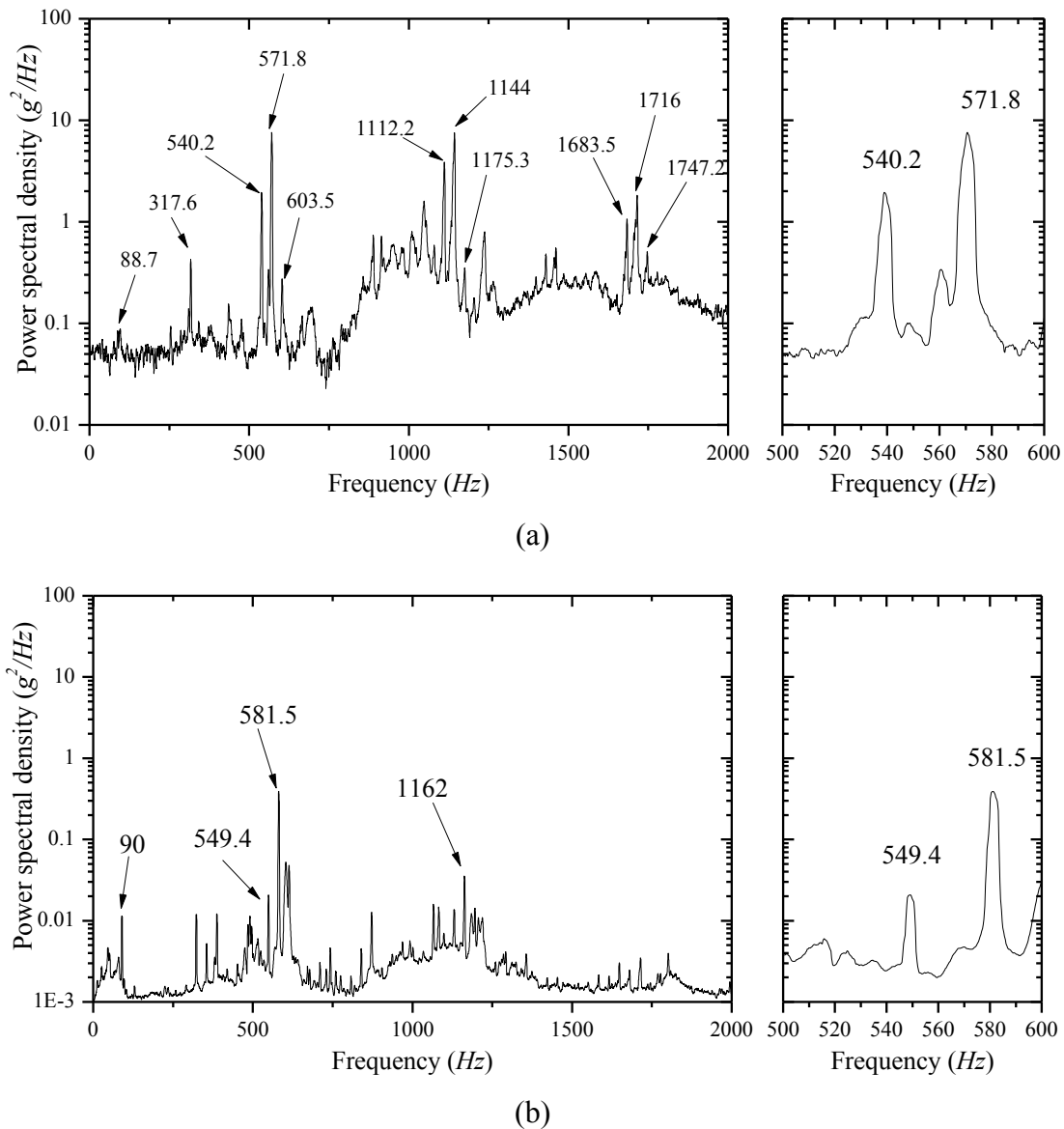
Figure 4.11: Power spectral density (PSD) of axle box vertical acceleration in the 0-2000 *Hz* and 500-600 *Hz* frequency ranges: (a) before re-profiling (98 *Mm*); and (b) after re-profiling (0 *Mm*).

The variations in *rms* values of the axle box acceleration obtained from the 2 *s* data windows are further evaluated as a function of the service mileage during the first cycle. Figure 4.12 illustrates variations in terms of box plots, where the peak values are obtained considering 99.85% probability. The peak *rms* acceleration is relatively small following the re-profiling (< 10 *g*), which is only slightly higher after 19 *Mm* of service. The axle box acceleration during the early service period is attributed to residual wheel roughness after re-profiling, and bending modes of the rail

and the wheelset, apart from the track irregularities. The mean and peak *rms* accelerations increase rapidly after 19 *Mm* mileage due to growth in high-order polygonalization of the wheels, although the rate of increase diminishes with service mileage exceeding 67 *Mm*.
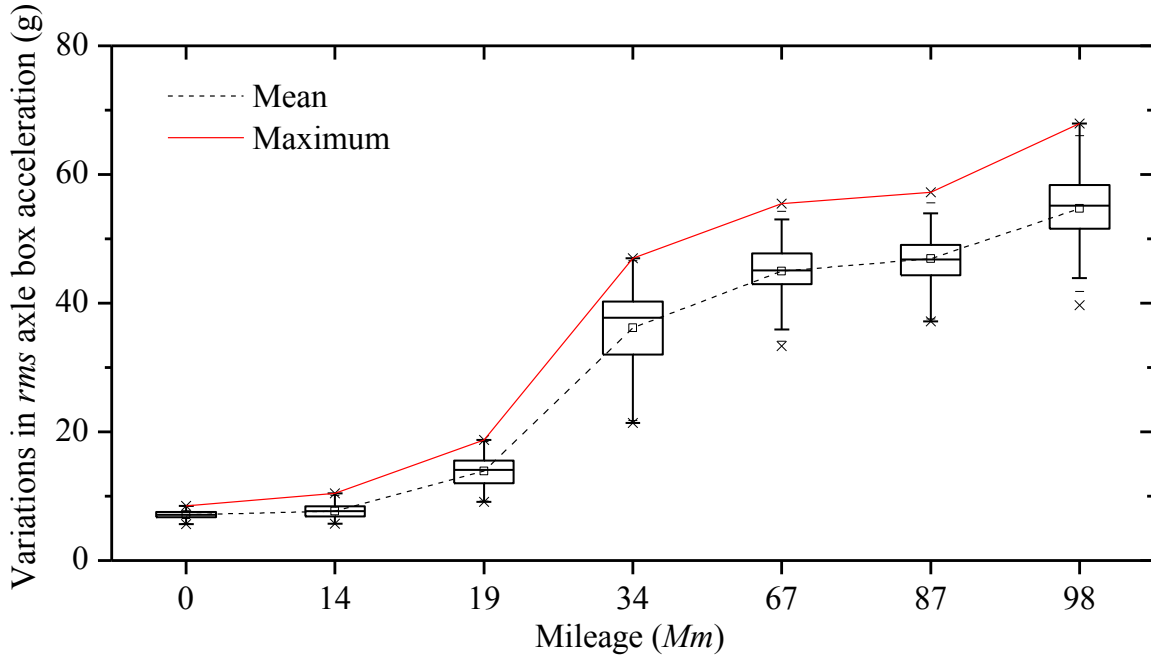
Figure 4.12：Variations in *rms* axle box acceleration with service mileage.

The magnitude of axle box acceleration is strongly related to the wheel surface roughness magnitude, as evident from Figure 4.13. The figure shows variations in peak axle box *rms* acceleration with peak magnitude of wheel roughness corresponding to harmonic orders 1, 17 and 18 during the first cycle of measurements, shown in Fig. 4.8. The study provided only three data points corresponding to 0, 89 and 98 Mm of service, which are considered insufficient to establish a reliable correlation between the axle box acceleration and the wheel roughness. The results, however, show very strong positive correlation between them with r^2 values in excess of 0.98 for all the three harmonic orders. This suggests that the axle box acceleration magnitude can serve as an important indicator of wheel deformities of the fundamental order as well as higher-order polygonal wear.
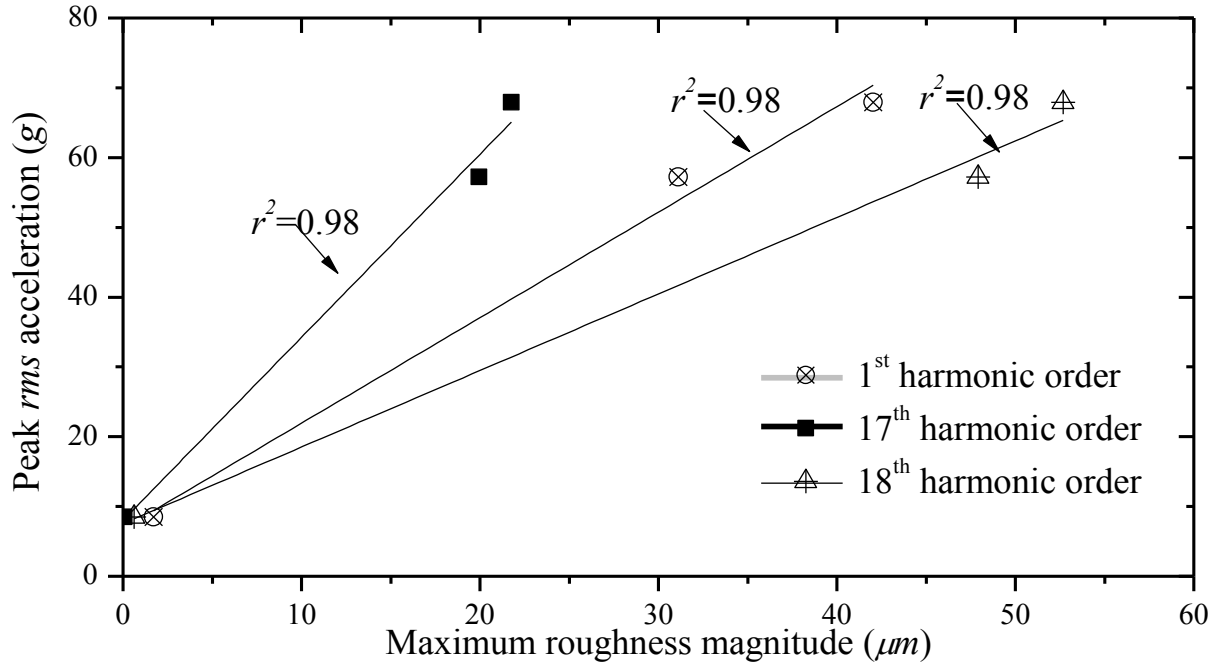
Figure 4.13: Correlation between peak *rms* acceleration and roughness magnitude corresponding to the 1st, 17th and 18th orders.

Owing to the limited number of data points acquired for the leading car wheels, the variations in peak axle box acceleration is further examined with variations in maximum and mean wheel roughness obtained across all the train wheels at different service mileage, as shown in Fig. 4.9. Figures 4.14(a) and 4.14(b) illustrate variations in peak axle box acceleration with peak and mean wheel roughness corresponding to orders 1, 18 and 19. The results show good correlation of the peak axle box *rms* acceleration with both the mean and maximum wheel roughness of all the three orders, although the correlation is not as strong as observed in Fig. 4.13. The correlation coefficients for mean roughness of orders 1, 18 and 19 are obtained as 0.66, 0.82 and 0.62, respectively, while those for maximum roughness are 0.77, 0.91 and 0.69. Relatively higher correlations of peak *rms* acceleration are obtained with the peak wheel wear magnitudes, irrespective of the order considered. The results further confirm greatest correlation of the peak *rms* axle box acceleration with the mean and peak 18th order wear magnitudes across all the train wheels (0.82 and 0.91). The correlations for the 1st and 19th order peak wear magnitudes are relatively lower but equal to or above 0.62.
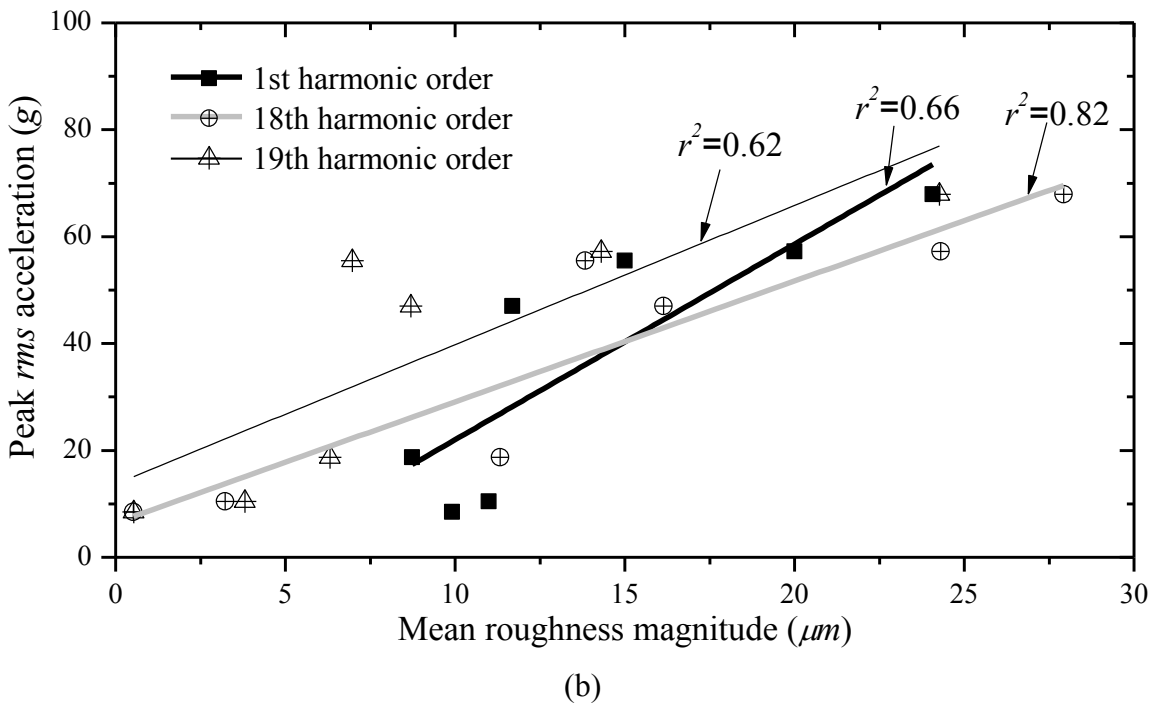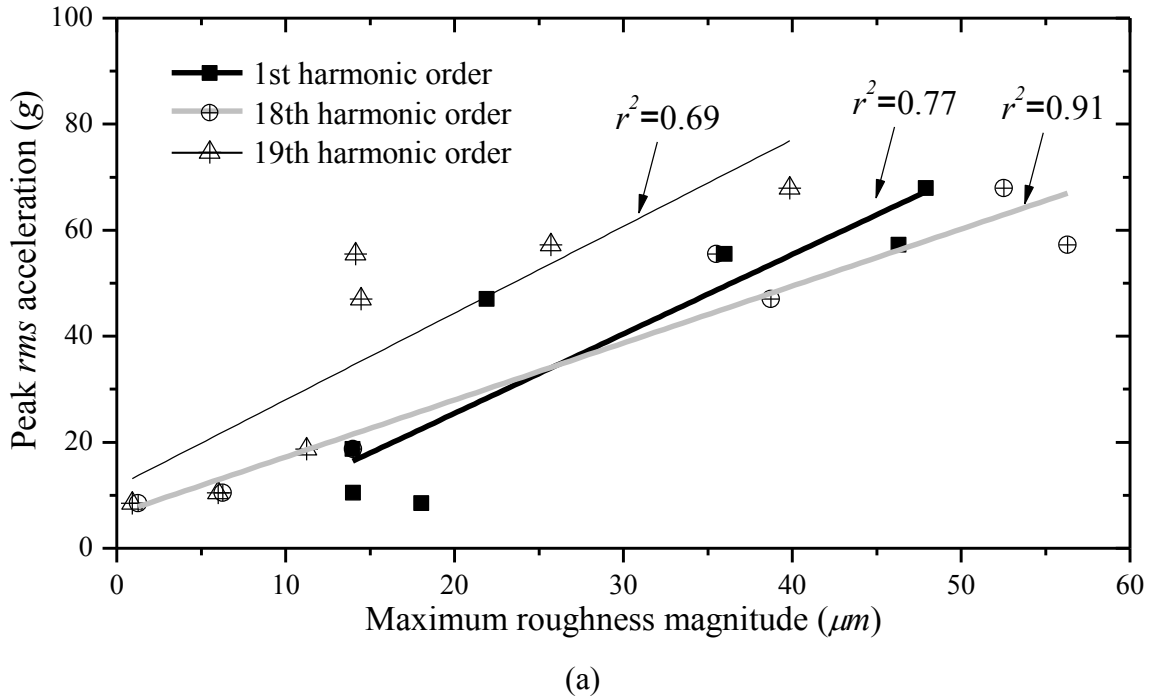
Figure 4.14: (a) Correlation of the peak *rms* acceleration with peak roughness magnitude across all the wheels, and (b) correlation of the peak *rms* acceleration with mean roughness of all the wheels.

4.4 Conclusions

A long term field test program involving measurements of wheel polygonal wear and axle box acceleration on a high speed rail vehicle operating at a nominal speed of 300 *km/h* permitted characterization of high order wheel polygonalization and its correlation with the resulting axle box acceleration. The measured data suggested that the wheel surface roughness could be characterized by a combination of the 1st and either 18th or 19th harmonic orders. The 18th order roughness magnitude increased with the service mileage compared to other harmonic orders. The results further showed comparable growth in higher order roughness magnitudes of wheels in the left- and right- tracks. Considerably higher standard deviation of the 18th order roughness was observed after the service mileage, which was due to distribution of the roughness in the 17th to 19th harmonic orders. Higher standard deviation of the roughness magnitudes corresponding to the 1st harmonic order was also observed following the re-profiling, which is attributed to the re-profiling process.

The axle box acceleration at the end of the first re-profiling cycle revealed dominant peaks near 540.2, 571.8 and 603.5 *Hz*, as well as the second and third multiples of the dominant frequencies. These dominant frequencies correspond to wheel roughness in the 17th to 19th harmonic orders, and bending modes of the rail and the wheelset. The acceleration response of the axle box decreased substantially after the wheel re-profiling. Very good correlation was observed between the peak *rms* acceleration of the axle box and peak roughness magnitudes of the dominating harmonic orders. This suggested that the axle box acceleration could serve as a good measure for detecting wheel polygonalization and thereby the wheel removal criterion.

CHAPTER 5: INVESTIGATION ON THE FORMATION MECHANISM OF WHEEL POLYGONALIZATION USING A LONG TERM WEAR MODEL

5.1 Introduction

The railway wheels are invariably subjected to wear and rolling contact fatigue, partly due to the wheel/rail interactions. These contribute to OOR (out-of-round) defects in the wheels, which have been characterized by either a local isolated defect or a continuous defect along the wheel circumference. Such defects accentuate high magnitude impact forces at the wheel-rail interface, which adversely affect the vehicle and track system performance [1,61]. The re-profiling of the wheels is undertaken frequently, especially in high-speed operations, to mitigate the OOR defects, which contribute to high maintenance cost and reduced service lives of the wheelsets. Considerable efforts have thus been made to identify the primary causal factors and to establish countermeasures for mitigating the growth of wheel OOR defects [7,21,25]. These have provided effective maintenance guidelines and wheel removal criteria, and considerable knowledge on the formation mechanisms of OOR defects.

A typical isolated OOR defect such as a wheel flat, characterized by the short wavelength defect on the wheel tread, has been attributed to sliding of the wheel on the rail [4]. The wheel sliding may be caused by poorly adjusted, frozen or defective brakes, or high level of braking force exceeding the available wheel/rail adhesion. The rail contaminants such as leaves, grease, frost and snow are also regarded as other important contributors [4]. Unlike the isolated defects, the mechanisms leading to continuous defects such as wheel corrugation and wheel polygonalization, however, have not yet been fully understood. The wheel corrugation is more likely induced by the thermo-mechanical coupling between the brake block and the wheel [13,14,15]. The wheel polygonalization has been partly attributed to the wheel re-profiling process [1], and in-part to high magnitude contact force developed at the wheel-rail interface [21,24,25,26,30].

The wheel polygonalization is a periodic radial irregularity or wear around the wheel circumference with wavelength larger than 100 *mm*, which has been widely reported in some high-speed trains [33,62]. The potential wear mechanisms resulting in lower order polygonal wear, ranging from 1 to 5, and the ensuing influences on dynamic responses of the vehicle have been reviewed by Nielsen *et al.* [1,16] together with the wheel removal criteria. The third and second order wheel polygonal wear were observed in solid and rubber wheels, respectively, in railways in

Germany. Rode *et al.* [21] pointed out that the third order polygonal irregularities of the wheels may be due to claw clamping of the wheel during the re-profiling process. In the ground lathe-based re-profiling process, a wheel is supported on its tread rather than the wheel centre, which may not completely eliminate the circumferential irregularity and thereby lead to a residual OOR [76].

This initial OOR could serve as primary contributory factor to the formation of higher order wheel polygonalization, when coupled with the fatigue wear due to high frequency and high magnitude wheel-rail contact forces. Many studies have thus focused on analyses of wheel-rail interactions through developments in comprehensive vehicle and track dynamic models [23,24, 25,26,27,141]. The flexibilities of the wheelset and the rail also cause higher lateral creepage at the wheel/rail interface, which may further contribute to enlargement of the OOR deformities [25,29,30]. The flexible wheelset and rail models are thus generally employed to account for contributions of elastic deformations to the wheel/rail interactions. Morys [25] proposed a lumped-parameter model of the wheelset comprising three-dimensional visco-elastic elements to account for lower bending and torsional modes of the wheelset axle. A few studies have integrated finite element models of the wheelsets and structural components to the vehicle/track models to investigate deformations of the axle and components [29,33,62]. The flexibility of the rail, discretely supported on rail pads, is generally described via the Euler beam or Timoshenko beam theories. The Timoshenko beam theory considering the shear deformation and rotational inertial has been reported as a more realistic representation for the rail compared to the Euler beam theory [38].

It has been suggested that wear process contributes to propagation of the initial low order polygonal wear to a higher order polygonal wear. This process, however, may involve complex combinations of different wear mechanisms such as delamination wear, oxidation or corrosive wear, abrasive wear and adhesive wear [136]. Bolton *et al.* [137] experimentally investigated wheel wear and classified it into three different wear regimes, namely, mild, severe and catastrophic. The mild wear was mainly attributed to oxidation and abrasion. The loss of material due to minor delamination of oxide layers contributed to severe wear, while further delamination lead to the catastrophic wear regime [138]. A number of wear models associated with different processes have been formulated to study wheel wear. Meng *et al.* [139] reviewed more than 180 different wear models, reported for different applications. The Archard and dissipated energy-based wear models

have been commonly used for predicting wear of the wheel and the rail due to wheel-rail interactions [140]. Johansson [141] compared the two models and concluded that both the wear models yield similar predictions of wear distribution on the wheel.

The changes in the wheel and rail profiles are primarily attributed to accumulation of wear over the service period. A long-term wear iterative scheme integrating the wear model to the vehicle-track model has been proposed to simulate wear accumulations of the wheel and the rail in the transverse and running directions [25,143,147,150]. The scheme involving several iterative steps, however, can lead to considerable accumulation of error. The method thus requires tuning of wear parameters using the measured data. Considerable efforts have been made to improve the accuracy of wear predictions in the rail and wheel profiles [143,144,148]. Since the rail corrugation and wheel polygonalization are regarded as abnormal wear at the wheel-rail interface, the predictions are more focused on their growth trends rather than the wear amplitude.

Brommundt [23] investigated interactions of a single flexible wheelset and the rail in the frequency domain using the perturbation technique together with the multiple time scale method. The study concluded that an increase in forward speed contributes to deformations dominated by the lower order harmonics. Using the 40-DOF model of a flexible wheelset axle, Meinke showed that dynamic imbalance and material inhomogeneity in the wheel may also contribute to periodic circumferential defects of the lower order [24]. Similar wear patterns due to wheel eccentricity were also observed from full-scale roller rig tests [7]. Morys [25] investigated the OOR defects through simulation of a vehicle and track model together with an energy-based wear model. In the vehicle model, each wheelset model incorporated 8 rigid bodies coupled via three-dimensional spring-damper elements to account for bending and torsional flexibility of the wheelset. The study concluded that the wheels with OOR defects could cause substantially higher impact loads at the wheel/rail interface, especially when operating on a relatively stiff substructure.

Meywerk [26] investigated the effects of varying hardness on the rate of wear using a long-term simulation model of the wheelset and the rail in the frequency domain. The results suggested that the first and second bending modes of the wheelset contribute considerably to propagation of the OOR defects, which may be further affected by phase difference between the OOR deformities of the left and right wheels. Jin et al. [30] experimentally investigated the effects and growth of polygonal wear of subway wheels, and concluded that the 9th order polygonal wear observed in the wheels was due to first bending mode vibration of the wheelset. Using a similar long-term iterative

scheme and considering the three-dimensional train-track interaction model, Johansson [27,141] suggested that the dominant wavelength of the wheel OOR is primarily related to the vertical mode resonance frequencies of the coupled train-track system and vertical anti-resonance of the track.

The aforementioned investigations are mainly focused on the low order wheel polygonalization through simulation of a long term wear iterative model. These suggest that the wheel re-profiling procedure, wheel/rail coupled vibration modes, wheelset flexibility, wheel imbalance and material inhomogeneity are the probable important causal factors leading to formation of relatively lower order wheel polygonalization. A few studies have reported wheels' polygonal wear of order as high as 24 in high-speed operations.

Zhang *et al.* [32] reported 19th and 20th order polygonal wear in wheels of high-speed trains in China, and investigated resulting interior noise in the passenger compartment using a high-speed wheel-track noise model. Wu *et al.* [33,62] investigated wheel-rail interactions in the presence of 20th order wheel polygonalization through simulation of a coupled vehicle/track dynamic model comprising a flexible wheelset model. The study concluded that high order wheel polygonalization can yield high frequency fluctuations in the wheel/rail contact force and very high axle box acceleration. The resulting high frequency and high magnitude impact forces at the wheel/rail interface could substantially reduce service life of a wheelset axle in the presence of a pre-existing crack. Wu *et al.* [34] experimentally investigated the formation of 23rd order wheel polygonalization in wheels of a high-speed train operating at a nominal speed of 250 *km/h*, and concluded that the formation of 23rd order wheel polygonalization is due to a vibration mode of the bogie subject to an external fixed-frequency excitation.

The high frequency and high magnitude impact loads arising from the wheel polygonalization are believed to be among as the primary casual factors leading to in-service failures of components of high speed railways in China. The adverse effects of wheel polygonalization on dynamic responses of the vehicle and the track together with associated high maintenance cost are the primary motivations of this investigation on identification of the primary contributors of the high order wheel polygonalization. In this study, a long term wear iterative scheme consisting of a coupled vehicle-track dynamic model and a wear model is formulated to investigate formation of the high order wheel polygonalization under high speed operations. The high order wheel polygonalization is characterized on the basis of measured data acquired on a high-speed train. The frequency response functions of the wheel-rail system are obtained and analyzed to identify

dominant excitation frequencies arising from the wheel-rail interactions. The evolution of wheel polygonalization along the wheel circumference considering different vehicle and track parameters is further investigated using the long term wear iterative scheme to determine the critical parameters affecting the formation of wheel polygonalization.

5.2 Long-term wear iteration scheme

The wheel polygonalization, known as the circumferential irregularities of the wheel, has been related to wear accumulation caused by the wheel/rail interactions over a relatively long service period [1]. A long-term wear prediction model is thus needed to investigate the growth in wheel polygonalization. Such a long-term prediction model has been used to investigate lower order wheel polygonalization [25,26,27] as well as the evolution of rail corrugation [152,166]. The long-term wear prediction model is formulated by integrating a wear model such as Archard sliding wear model to the coupled vehicle/track dynamic model, as shown in Fig.5.1. An iterative scheme is used to extend the wear prediction to relative long service periods, where each iteration describes the wear accumulation with an incremental operating distance of the wheel.
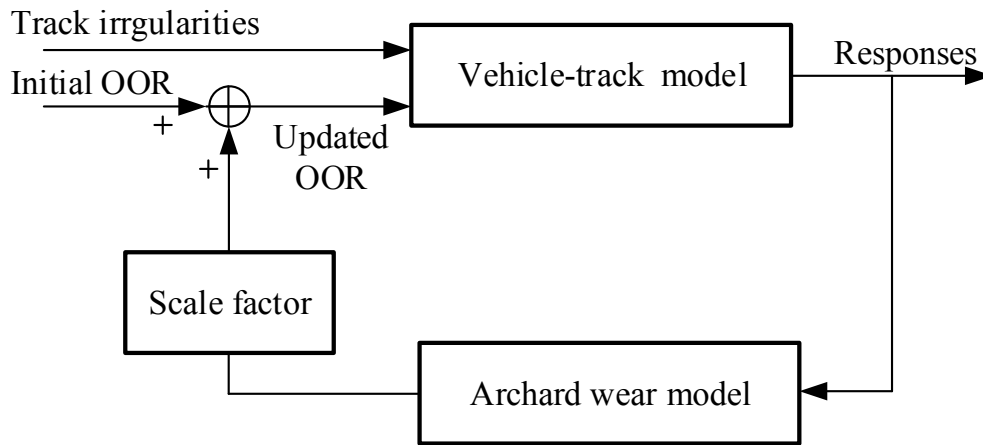
Figure 5.1: Long-term wear iteration scheme [27].

In the iterative scheme designed for predicting wheel wear, the initial OOR wheel irregularity measured after the re-profiling process together with the track irregularities are taken as inputs to the vehicle/track simulation model to determine resulting dynamic responses at the wheel-rail interface such as wheel/rail contact forces, creepage and slip region of the contact patch. The wear at each discrete point on the wheel circumference is subsequently predicted from the Archard wear model, which is taken as the short-term wear. The resulting short-term wear is manipulated via a scale factor to predict wear accumulation over a relatively longer operating distance in a

computationally efficient manner [27]. The wheel profile is updated using the predicted wear response, which serves as the input to the vehicle/track model in the subsequent iteration, as seen in Fig.5.1. The iterative scheme thus permits prediction of evolution of wheel OOR over a relatively long period.

5.2.1 Coupled vehicle-track dynamic model

The vehicle/track system model is formulated for a typical high-speed railway car with flexible wheelsets coupled to the flexible slab track model through the wheel/rail contact model. The coupled model has been described in details in [29]. Briefly, the model comprises a car body supported on two bogies through the secondary suspensions. Each bogie frame is coupled with two wheelsets through the primary suspension and the axle box oriented along the longitudinal direction. Each wheelset is modelled as a flexible body. Modal approach is used to integrate both the flexible slab track and wheelset models to the car body and bogie, which are modeled as rigid bodies with 6 DOFs (degrees-of-freedom). The axle box, however, is only permitted to pitch about the axis of the wheelset axle shaft. The primary and secondary suspensions are modelled as parallel linear springs and viscous dampers along the three translational directions.

The track system is modelled as a flexible slab track, while the rail is described by the Timoshenko beam discretely supported on a slab segment via rail pads. Each slab segment, continuously supported on the cement asphalt mortar (CAM) layer, is modelled using finite element method. Each rail pad is modelled as a parallel combination of a linear spring and a viscous damper. The elasticity of the CAM layer is represented through discretely distributed spring-damper elements. The vehicle and track models are coupled through the wheel/rail contact model considering the S1002CN wheel and Rail 60 profiles [167]. The normal force distributed over the wheel-rail contact patch is determined through the Hertzian contact theory as a function of the penetration between the wheel and the rail. The tangential force developed in the contact patch is also calculated using the FASTSIM algorithm [124]. The model is limited to constant forward speed neglecting the contributions due to variations in longitudinal (braking/acceleration) forces. The wheel-rail contact force in the normal direction alone arising from excitations from a wheel with OOR defect is thus considered for wear prediction.

5.2.2 Wheel wear model

The effect of dynamic wheel-rail contact force on the wheel wear is evaluated considering the slip region of the contact patch, which is determined from the FASTSIM algorithm [124]. For this purpose, the wheel is discretized into a total of 3600 points over its circumference with a resolution of 0.1° or 0.8 *mm*. The wear of each circumferential point within the slip region due to distributed contact force response is obtained using the Archard wear model. The model predicts the wear volume V_{wear} at each contact point within the slip region as a function of the material hardness H, a wear coefficient k_w, normal force N and the sliding distance d [138], such that:

$$V_{wear} = k_w \frac{Nd}{H} \tag{1}$$

The normal force developed at a point within the contact patch can be determined from the wheel/rail contact pressure distribution, given by [168,169]:

$$p_z(x,y) = \frac{3N}{2\pi ab}\sqrt{1 - \left(\frac{x}{a}\right)^2 - \left(\frac{y}{b}\right)^2} \tag{2}$$

where $p_z(x,y)$ is the contact pressure at a point within the contact patch with coordinates (x,y), and a and b are semi-axes of the elliptical contact patch, determined from the FASTSIM algorithm, as shown in Fig.5.2. The contact patch is further discretized into $m \times n$ elements with m strips along the y axes, each containing n elements. The number of elements is selected so as to obtain accurate prediction of the localized contact force. Polach [170] suggested that consideration of a 10×10 elements grid in the contact patch in the FASTSIM algorithm can yield reasonably accurate predictions of the contact force distribution. Johansson [141] showed that the accuracy of prediction increases with greater grid size, and a dense discretization can provide a continuous wear distribution. In this study, a grid of 30×30 elements is considered, which can yield an accuracy of about 95% in the estimation of creep forces according to the relationship between the number of elements and the estimation accuracy reported in [141].

Upon substituting Eq. (2) into Eq. (1), the wear depth $\Delta z(x_{ij}, y_{ij})$ for each element can be obtained as:

$$\Delta z(x_{ij}, y_{ij}) = k_w \frac{p_z(x_{ij},y_{ij})\Delta d(x_{ij},y_{ij})}{H}, \; i = 1 \cdots n, \; j = 1 \cdots m \tag{3}$$

where (x_{ij}, y_{ij}) is coordinate of center of the i_{th} element within the j_{th} strip and $\Delta d(x_{ij}, y_{ij}) = |s(x_{ij}, y_{ij})|\Delta t$ represents the sliding distance of the same element. The time increment Δt is the time duration that a material point on the wheel remains within one element of the contact

patch, $\Delta t = \Delta x_j / v_0$, where v_0 is the vehicle speed and Δx_j is the element length. The resultant slip velocity $S(x_{ij}, y_{ij})$ for each element is determined in the slip region of the contact patch via the FASTSIM algorithm. The wear depth $\Delta z(x_{ij}, y_{ij})$ for each element can thus be expressed as a function of the slip velocities in x- and y-directions, S_x and S_y, as:

$$\Delta z(x_{ij}, y_{ij}) = \frac{3Nk_w}{2\pi abH} \sqrt{1 - \left(\frac{x_{ij}}{a}\right)^2 - \left(\frac{y_{ij}}{b}\right)^2} \sqrt{s_x^2(x_{ij}, y_{ij}) + s_y^2(x_{ij}, y_{ij})} \frac{\Delta x_j}{v_0} \tag{4}$$
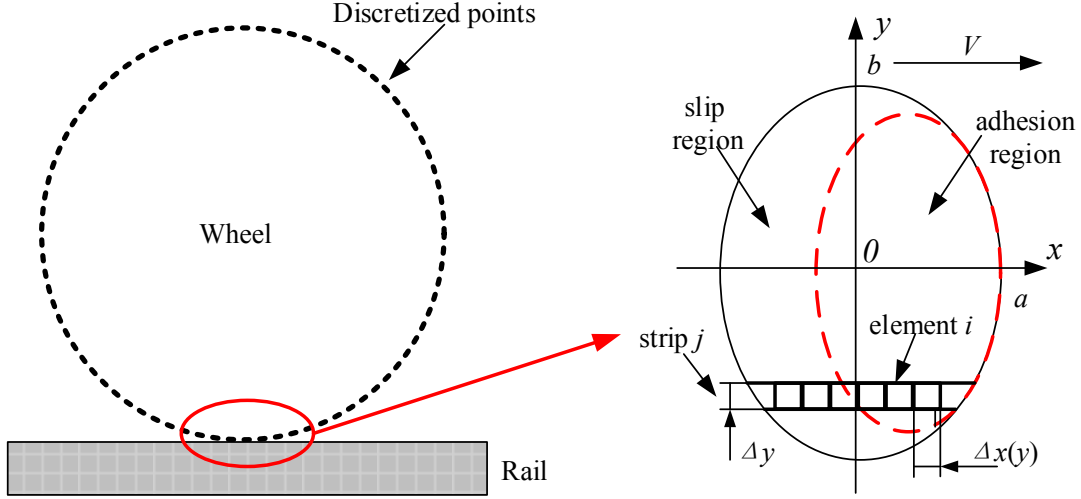
Figure 5. 2: Contact patch at the wheel/rail interface together with the slip region.

The total wheel wear within a strip j, Δz_j, is obtained by summing the wear depth of the elements along the strip [143]. Since the 2-dimensional wear distribution along the wheel circumference is of interest, the maximum wear depth $\Delta z = \max(\Delta z_j)$ across all the strips is taken as the wear depth of each discrete point in the wheel circumference.

Owing to strong nonlinearities in the wear process, the wear coefficient k_w in the Archard model may vary considerably. The variations in the coefficient are generally presented by a wear chart in terms of the normal contact pressure p and the slip velocity S on the basis of measurements [143]. In the present study, the growth trend of wheel polygonalization is the primary focus and the simulations of dynamic wheel/rail contact forces are limited only to the tangent track at a constant forward speed rather than the curved track. Since the sliding region within the contact patch is expected to be very small, a constant value of the wear coefficient is assumed as, $k_w = 1 \times 10^{-4}$ [27,141].

5.2.3 Long term wear prediction

Owing to the large computational demand of the coupled vehicle-track dynamic model together with the wear calculations, the simulations during each iteration were limited to a small operating distance considering only 15 wheel revolutions, as suggested in [27,141]. The wheel wear obtained from responses at the wheel-rail interface, namely, the wheel-rail contact forces, creepage and size of the sliding region, is thus regarded as the short term wear. The wear accumulation over long operating distances is predicted through repeated iterations, as shown in Fig.5.1. The measurements of the wheel profiles as a function of the distance suggest nearly linear growth in wheel polygonalization during the initial travel distances following the wheel re-profiling [173]. The rate of growth, however, increases more rapidly with further increase in the travel distance. It is assumed that the wear accumulation varies nearly linearly with the operating distance over a relatively short distance of 550 *km* considered during a given iteration. This approach has also been suggested in [171] on the basis of measurements obtained in the wheels of a Amfleet vehicle. The short term wear predicted from the Archard model is thus scaled by a factor (550 *km*/distance traveled in 15 wheel revolutions at a given forward speed) to estimate the wear depth accumulation over the operating distance of 550 *km*. This process serves as one iterative step in the long-term wear iterative scheme, and the wear accumulation in a relative long period can be obtained by repeating this process for each 550 *km* distance, assuming piece-wise linear growth in wear with increasing distance.

Furthermore, in each of the subsequent iterative step, the position of the wheel with respect to the rail is altered, and the direction of motion of the vehicle is reversed alternatively. This approach is considered to more realistically represent the routine operation of a train [25,27,141]. Moreover, the simulations are limited to the tangent track alone, as in the case of various reported studies [23,24,25,26,27,141], and the minimum wear depth is subtracted from the total wear to obtain wear magnitude, which is superimposed to the wheel circumference.

5.3 Method of analysis

The coupled vehicle/track model is initially analyzed under excitations arising from: (i) initial circumferential irregularity in the rear left wheel of the leading bogie; and (ii) track irregularities. Figures 5.3(a) and 5.3(b) illustrate measured deviations in the radius of the rear left wheel and its harmonic distribution following its re-profiling [172], while the nominal wheel radius is taken as

0.43 *m*. On the basis of the measured data, the wheel irregularity is characterized by the 2nd harmonic order with amplitude of 7.1 *dB*. The measured variations in the vertical and lateral profiles of a high-speed track, shown in Figs. 5.3(c) and 5.3(d), respectively, are taken as the excitation due to track. Table 5.1 summarizes the primary simulation parameters. The resulting responses at the wheel-rail contact, including the slip velocities within the slip region, are used to obtain short-term wheel wear using the Archard wear model considering a nominal forward speed of 300 *km/h*. The wear accumulation over the travel distance of 550 *km* is subsequently obtained assuming linear growth in the wheel wear. The wear accumulations are obtained for all the wheels of the leading bogie using an identical scale factor. The circumferential variations in the wheel profiles are updated to determine the responses at the wheel-rail interface during the successive iteration, as seen in Fig.5.1, while the track profile remains unaltered. The accumulation of wear of all the wheels of the leading bogie over the long distances is subsequently obtained through repeated iterations, while the number of iterations is limited to 50. The results are used to identify the patterns of wheel wear, which are discussed in relation to the reported measured data. The frequency spectra of the vertical wheel-rail contact force and lateral creepage are further obtained to identify dominant excitation frequencies that may contribute to the formation of wheel polygonalization.

Table 5. 1: Primary simulation model parameters.

Parameters	Values
Material hardness of wheel tread	3.2 *GPa*
Wear coefficient	1×10^{-4}
Friction coefficient	0.3
Discretization of contact patch	30×30
Number of iterations	50
Wheelbase of the bogie	2.5 *m*
Vertical stiffness of the primary suspension	0.9 *MN/m*
Support stiffness of the rail pad	20 *MN/m*
Damping coefficient of the rail pad	30 *kNs/m*
Sleeper bay	0.63 *m*
Wheel radius	0.43 *m*
Wheel profile	S1002CN
Rail profile	Rail 60
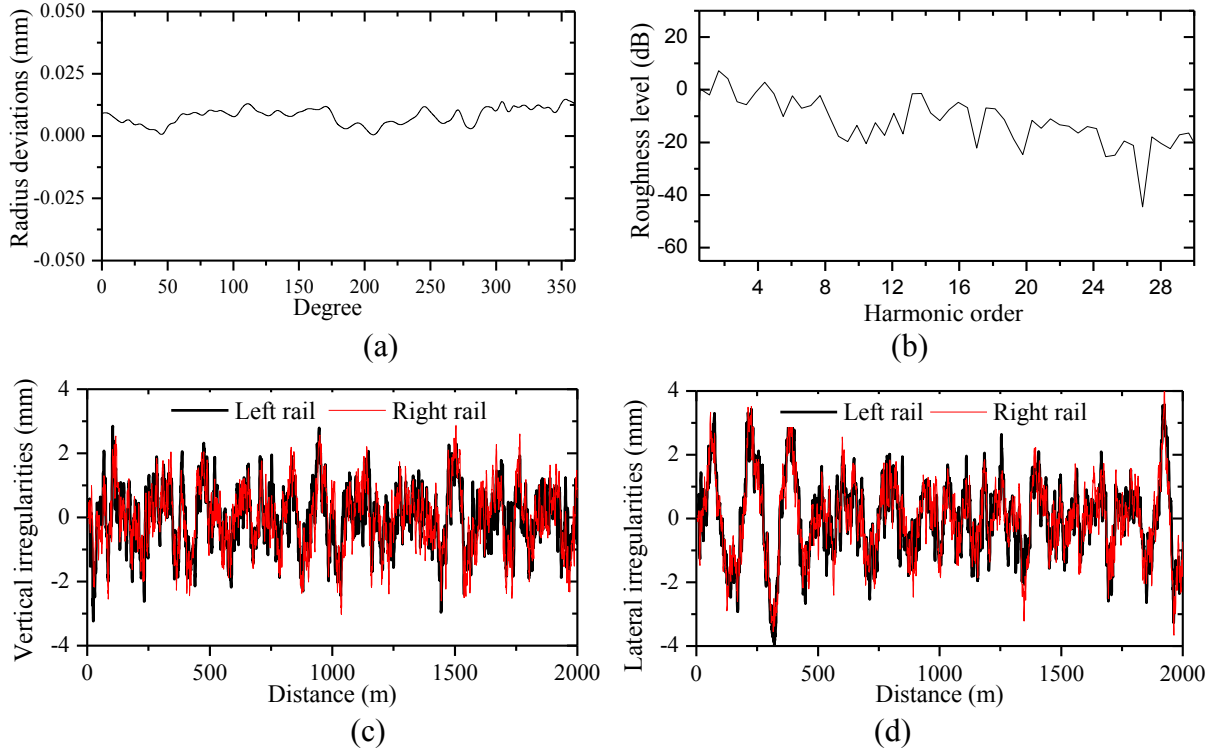
Figure 5. 3: (a) Measured variations in radius of a wheel following re-profiling; (b) harmonic order of the wheel irregularity; (c) vertical profiles of the left- and right rails; and (d) lateral profiles of the left- and right rails.

5.4 Results and discussions

5.4.1 Prediction of wheel polygonal wear

Figures 5.4(a) to 5.4(d) illustrate growth in wear of the wheels of the front bogie, obtained after each iteration considering the initial 2nd order polygonal wear of the rear left wheel alone (Fig. 5.3(a)) and a forward speed of 300 *km/h*. The figure shows the distribution of wear magnitude around the wheel circumference, obtained after adjusting for the minimum wear depth. Owing to small changes in the wear amplitude, the results obtained after each iteration are slightly shifted along the y-axis by 0.00005 *mm* for each iteration step to illustrate the growth trend more clearly. The results show notable growth in circumferential irregularities following each iteration, and evolve into polygonal wear dominant around the 18th harmonic order after about 12 iterations, as seen in Fig. 5.4(e). The polygonal wear is evident in all the wheels, although more pronounced in the left wheels.

The resulting wheel wear pattern is comparable with the trends observed from the measurements reported by Wu *et al.* [172] for the wheels in a high-speed train running at a speed of 300 *km/h*. The measured data showed wheel wear dominated by the 18th order wheel

polygonalization, where the nominal wheel radius was 0.428 m. The rate of growth of wheel polygonalization in a high-speed train has also been reported in a recent long-term field measurement study [173]. The measurements were performed at a nominal forward of 300 km/h with nominal wheel radius of 0.43 m. The study reported evolution of notable polygonal wheel wear within travel distance of 131 Mm, which could be characterized by the 18th to 19th harmonic order.

The simulation results in Fig. 5.4 further show substantially higher roughness magnitudes of the left wheels compared to the right wheels. This is due to relatively higher magnitudes of contact forces developed at the rear left wheel with initial OOR. The rapid growth in polygonal wear of the front left wheel is also attributable to contributions of the rear left-wheel contact forces through the rail. The wear patterns of the right wheels also show dominance of 18th order polygonalization, although the roughness magnitudes are considerably smaller than those of the left wheels. The formation of wheel polygonalization in the right wheels can be attributed to the coupled dynamic motions of the wheelsets and transmission of contact forces from the left wheels. The roughness magnitudes of both the left wheels corresponding to the 18th harmonic order, obtained after 50 iterations, however, are comparable, as seen in Fig. 5.4(e).

Figure 5.5 further illustrates the growth in wear magnitudes of the wheels corresponding to the 18th harmonic order over 50 iteration steps considered in the study. The variations in wear magnitudes of all the wheels are quite small up to about 30 iterations, which correspond to travel distance of 16,500 km. A rapid growth in the wear magnitudes, however, is observed during subsequent iterations. Both the left wheels exhibit comparable rate of growth in wear, which is substantially greater than that of the right wheels. This is due to intensified interactions of the rear left wheel with initial OOR with the rail. The wear accumulation or roughness magnitude (RM) of the wheels can be related to the travel distance by the following power law:

$$RM_{dB} = \alpha\beta^d \tag{5}$$

Where α and β are the regression constants, which for the rear left wheel are obtained as 0.312 and 1.167, respectively, and d is distance in Mm (correlation coefficient, $r^2 \approx 0.99$). Similar trends have also been reported from the measurements reported by Tao $et\ al.$ [174], Wu $et\ al.$ [172] and Wu $et\ al.$ [173]. Tao $et\ al.$ [174] measured the profiles of wheels of an electric locomotive and observed development of polygonal wheel after 27,400 km service following the re-profiling process. Wu $et\ al.$ [173] reported development in 18th and 19th order polygonal wear of the re-

profiled wheels of a high-speed train (nominal speed = 300 *km/h*) after a travel distance of about 14 *Mm*. Wu *et al.* [172] also reported growth in 18th order wheel polygonalization in high speed train wheels (nominal speed = 300 *km/h*) after relatively short operating distances.
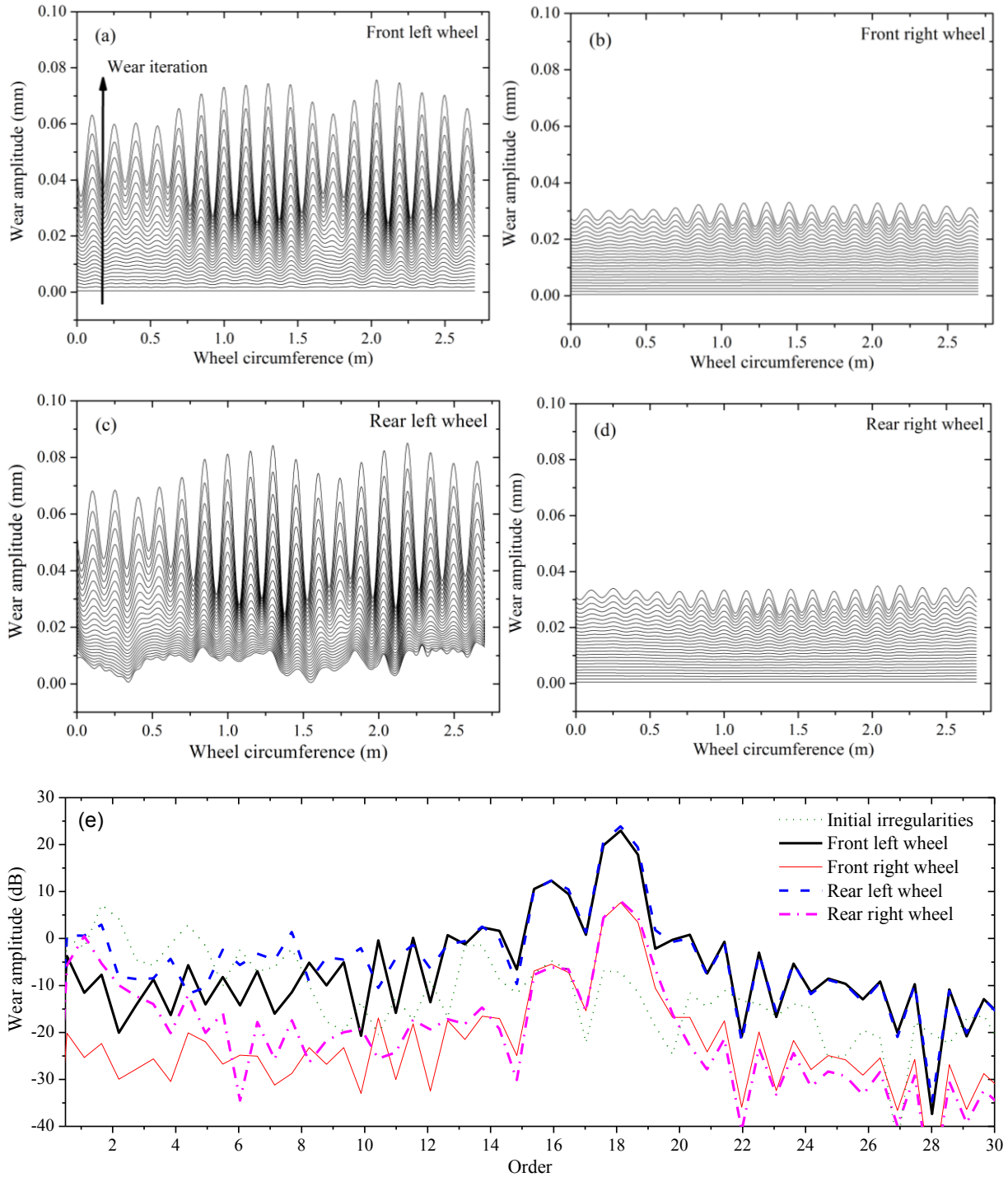
Figure 5.4: Variations in wear patterns of wheels of the front bogie following each iteration: (a) front left wheel; (b) front right wheel; (c) rear left wheel; (d) rear right wheel; and (e) harmonic order distribution of wear of all wheels after 50 iterations.
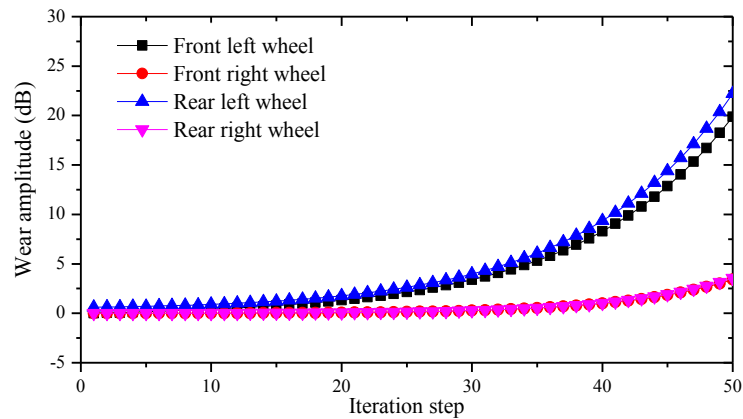
Figure 5.5: Increase in roughness magnitudes of the front bogie wheels corresponding to the 18th harmonic order with increasing iterations.

The increasing wear magnitude contributes to rapid increase in the peak normal force and creepage at the wheel-rail contact, as seen in Figs. 5.6(a) and 5.6(b). Owing to comparable wear magnitudes of the left and right wheels of the two wheelsets, the results are presented only for the front wheelset. Exponential-like growth in the peak normal force and lateral creepage with increasing iterations is observed; as in the case of 18th harmonic order wear magnitude shown in Fig. 5.5. Strong positive correlations of both the normal force and lateral creepage with the wheel wear magnitude corresponding to the 18th harmonic order were observed (r^2>0.99). The frequency spectra of the normal force and lateral creepage developed at the front-left wheel-rail contact after each iteration are further shown in Figs. 5.6(c) and 5.6(d), respectively. The frequency spectra of contact forces obtained after each iteration are slightly shifted along the y-axis so as to emphasize the magnitude variations. Both the frequency show dominant peaks around 555 *Hz*, which corresponds to 18th order of the wheel rotation frequency at 300 *km/h* (30.84 *Hz*), and is denoted as passing frequency of the polygonal wheel.

The results in Figs. 5.4 to 5.6 suggest that the wheel/rail interactions caused by initial irregularities in a wheel of a bogie can accelerate the formation of wheel polygonalization in all the wheels of the bogie. A more accurate re-profiling process is thus needed to reduce the magnitude of initial/residual irregularities on the wheel surface.
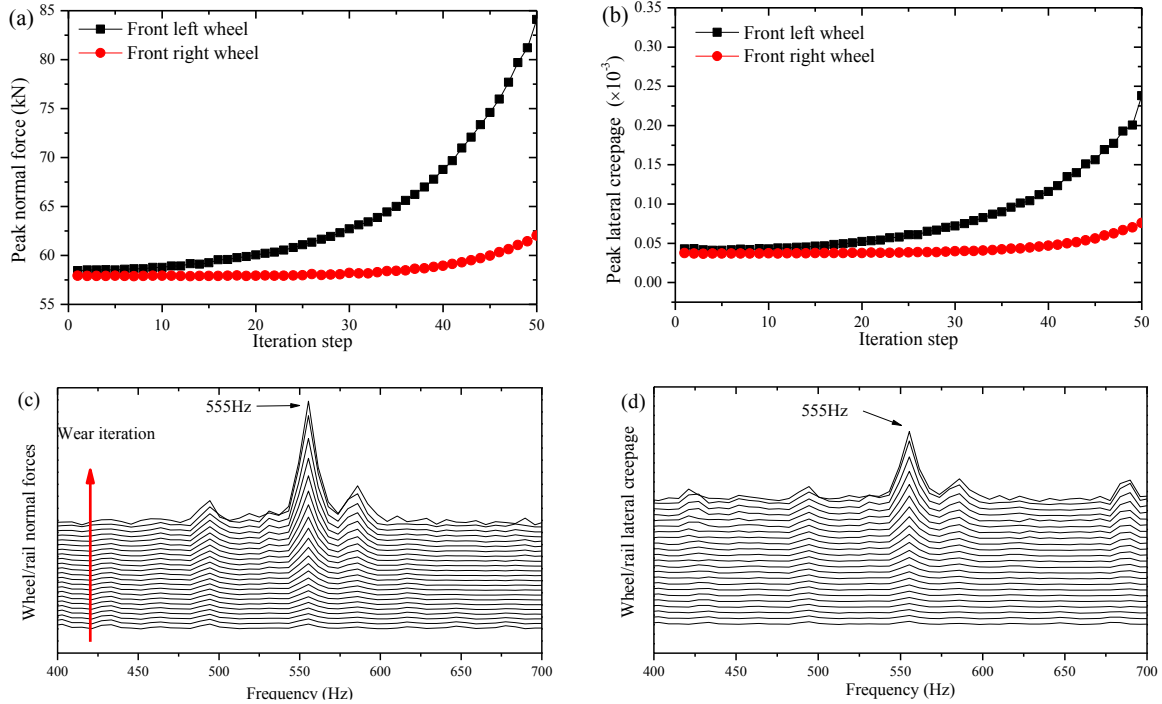
Figure 5.6: (a,b) Peak normal force and lateral creepage observed at the wheels of the front wheelset; and (c,d) variations in frequency spectra of the normal force and lateral creepage developed at the front left wheel after each iteration.

5.4.2 Frequency response characteristics of wheel/rail interactions

The vibration modes of the vehicle system contribute to the components' deformations and magnitudes of contact forces development at the wheel-rail interface and thereby the wheel wear. The normal force and lateral creepage responses of the coupled vehicle/track model are evaluated under harmonic excitations in the 1-1400 *Hz* frequency range to obtain the frequency response characteristics. Although the frequency response behavior of the nonlinear system model may depend strongly upon the magnitude as well as phase difference of excitations applied at the wheel-rail interface, the frequency responses are obtained considering 0.01 *mm* vertical displacement excitation applied to each wheel/rail interface. Moreover, the wheelsets are assumed to be rigid.

The frequency responses show two distinct peaks in the normal contact force and lateral creepage, near 650 *Hz* and 1300 *Hz*, as seen in Figs. 5.7(a) and 5.7(b). The peak near 1300 *Hz* is likely associated with a high-order bending mode of the rail. The peak near 650 *Hz* has been associated with localized bending mode of the rail segment between the front and rear wheelsets, also denoted as three half wavelength rail bending mode [113,152,165]. This is also evident from vertical deflection pattern of the rail section at the excitation frequency of 650 *Hz,* shown in Fig.

5.8. The deflection pattern, zoomed around the positions of the two wheelsets, revealed two nodes, where the rail deflection is identical to that corresponding to the static wheel load. A few studies have reported that this rail deflection mode yields dominant magnitudes of normal force and lateral creepage at the wheel-rail interface in the 500~800 *Hz* frequency range, and is among the main contributors to the formation of rail corrugation [113,152,165].
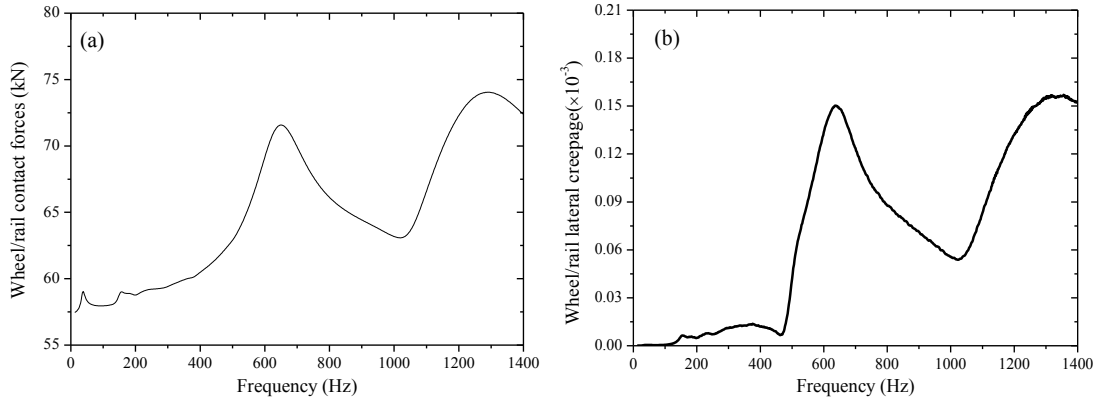
Figure 5.7: Frequency response characteristics of the wheel/rail contact forces: (a) normal force, and (b) lateral creepage.
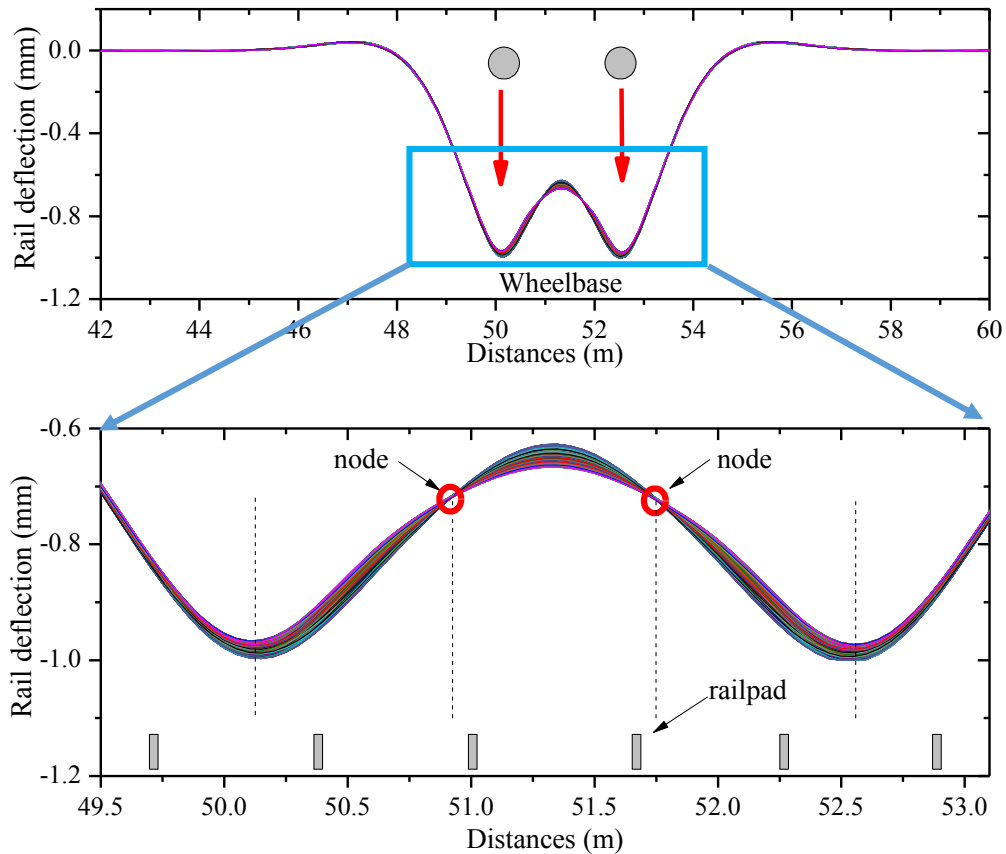
Figure 5.8: Deflection response of the rail under 650 Hz excitation.

This dominant frequency is also in the proximity of the passing frequency of a wheel with 18th order polygonal wear, as observed in Fig. 5.6. It may thus be speculated that this bending mode frequency of the rail segment is also a likely contributor to formation of wheel polygonalization, although the passing frequency of the wheel (555 *Hz*) differs from the rail bending mode frequency (650 *Hz*). These could further suggest that the formation of wheel polygonalization is also related to the wear process rather than the wheel/rail interaction alone. The responses below 100 *Hz* have been widely associated with coupled wheel/rail vertical mode, which is related to the wheelset mass, the stiffness of primary suspension and the stiffness of rail pads [36,161]. In the simulations, relatively soft rail pads (stiffness =20 *MN/m*) are considered, which are commonly used in the high-speed tracks in China. These yield the wheel/rail coupled vibration mode near 40 *Hz*, as seen in Fig. 5.7(a).

5.4.3 Influences of operating parameters on the formation of wheel polygonalization

The rail bending mode near 650 *Hz* constitutes a fixed frequency excitation to the wheel-track system, and lies in the vicinity of the wheel passing frequency when operating at the speed of 300 *km/h*. Two approaches may be considered promising for limiting the rate of growth in the 18th-order polygonal wear. Firstly, the operations at varying speeds, as opposed to a fixed nominal speed, can help distribute the wheel wear across different harmonic orders. In the second approach, the growth in wear could be reduced by limiting the normal force and lateral creepage at the wheel-rail interface, which are strongly and positively correlated with the wheel wear, as seen in Figs. 5.5 and 5.6. The magnitudes of wheel-rail interactions are strongly related to operating speed and vehicle/track design factors such as wheelset flexibility, wheelbase, and viscous and elastic properties of the rail pad. The variations in the wheelbase and rail pad properties can also alter the rail bending mode frequency, and thereby the rate of growth in wheel polygonalization. Influences of variations in these parameters on the resulting amplitude and order of wheel wear is thus investigated to identify the favorable design and operating factors in view of evolutions in wheel polygonalization.

5.4.3.1 Flexibility of wheelset

The high magnitude and high frequency wheel-rail contact forces are known to excite various deflection modes of the wheelset. The deformations of the wheelset also cause higher magnitude lateral creepage at the wheel/rail interface, which may accelerates the formation of wheel

polygonalization [25,26,29,33]. Figures 5.9(a) and 5.9(b) compare the peak contact normal force and lateral creepage, respectively, developed at the front left wheel-rail contact considering both the rigid and flexible wheelsets in the simulation model. The results show comparable peak normal force response of the rigid and flexible wheelsets, which suggest small or negligible contributions of the wheelset defection modes. This tendency has also been reported in [40,58], which suggested that the wheelset flexibility may affect the normal force response at frequencies above 1500 *Hz*. The wheelset flexibility, however, yields notable effect on peak lateral creepage at frequencies below 300 *Hz*, as seen in Fig. 5.9(b), which is not evident in case of the rigid wheelset. The peak response of the flexible wheelset near 200 *Hz* has been related to a bending vibration mode of the wheelset leading to out-of-phase lateral deflections of the right and left wheels [29]. Furthermore, Morys [25] showed that the bending mode of the wheelset below 200 *Hz* can contribute considerably to the lateral creepage at the wheel-rail interface.
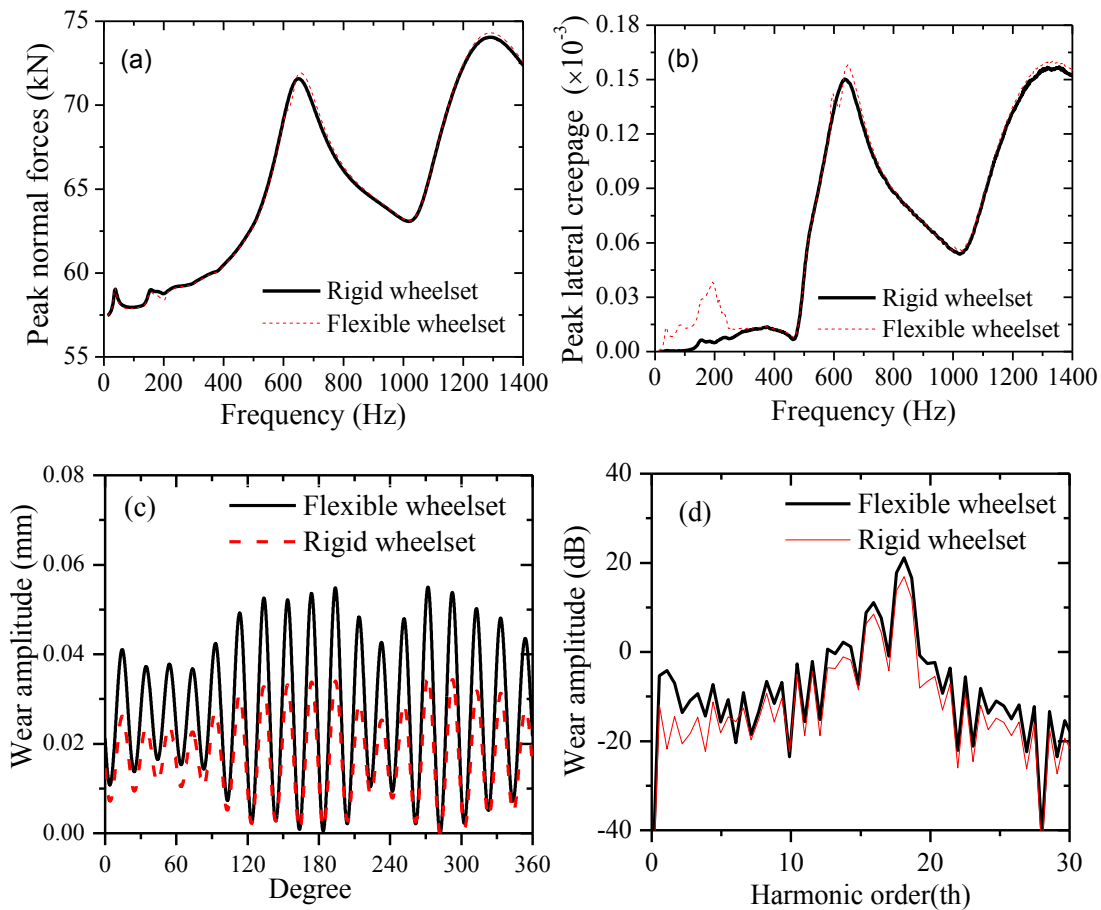
Figure 5.9: Influence of the wheelset flexibility on the wheel-rail interactions and wheel wear: (a) frequency spectrum of the peak normal force; (b) frequency spectrum of peak lateral creepage; (c) wheel wear pattern; and (d) harmonic orders of the polygonal wheel wear.

Figure 5.9(c) compares the cumulative wear of the left wheel of the front wheelset obtained after 50 iterations, while considering rigid as well as flexible wheelsets. The wheel wear is dominant near the 18th harmonic order in both cases, as seen in Fig. 5.9(d). The magnitude of wheel wear, however, is substantially higher for the flexible wheelset compared to the rigid wheelset, which suggests that the flexibility of the wheelset contributes to higher rate of growth in wheel polygonalization. Although, both the wheelsets yield dominant wheel wear near the 18th harmonic order, the wear magnitude is more pronounced in case of the flexible wheelset. Apart from the high-order wheel polygonalization, the flexible wheelset also yields notable higher wear magnitudes corresponding to the lower harmonic orders. This is likely due to higher low frequency lateral creepage of the flexible wheelset, as seen in Fig. 5.9(b).

5.4.3.2 Vehicle speeds

Studies reporting measured wheel wear patterns have shown important effects of operating speed on the magnitude and harmonic order of wheel polygonalization [34,172]. Owing to the large computational demand of the model with flexible wheelset and nearly negligible effect of wheelset flexibility on the dominant harmonic order of the wheel wear, the effect of vehicle speed on the wheel wear is investigated only for the rigid wheelset. Figures 5.10(a) and 5.10(b) illustrate patterns of cumulative wheel wear and the harmonic distributions obtained for two different speeds: 300 and 250 *km/h*. The wheels in both simulation scenarios show the high order polygonal wear along the wheel circumference. The results show that dominant harmonic order of polygonal wheel wear increases from 18 to 22, when the operating speed decreases from 300 to 250 *km/h*. The observed 22nd order wheel polygonalization is comparable with that reported by Wu *et al.* [34] for a high-speed train running at 250 *km/h* with nominal wheel radius of 0.43 *m*. The frequency spectra of the wheel-rail contact normal force developed by the front-left wheel with cumulative wear are further obtained via Fast Fourier Transform (FFT). The frequency spectra, illustrated in Fig. 5.10(c), show primary peaks in the narrow frequency range of 555 to 565 *Hz* for both the operating speeds. This is due to the fact that reduced speed coupled with higher harmonic order yield similar wheel passing frequency. This constitutes a nearly fixed frequency excitation to the vehicle, which likely is a primary contributor to the formation of high-order wheel polygonalization.
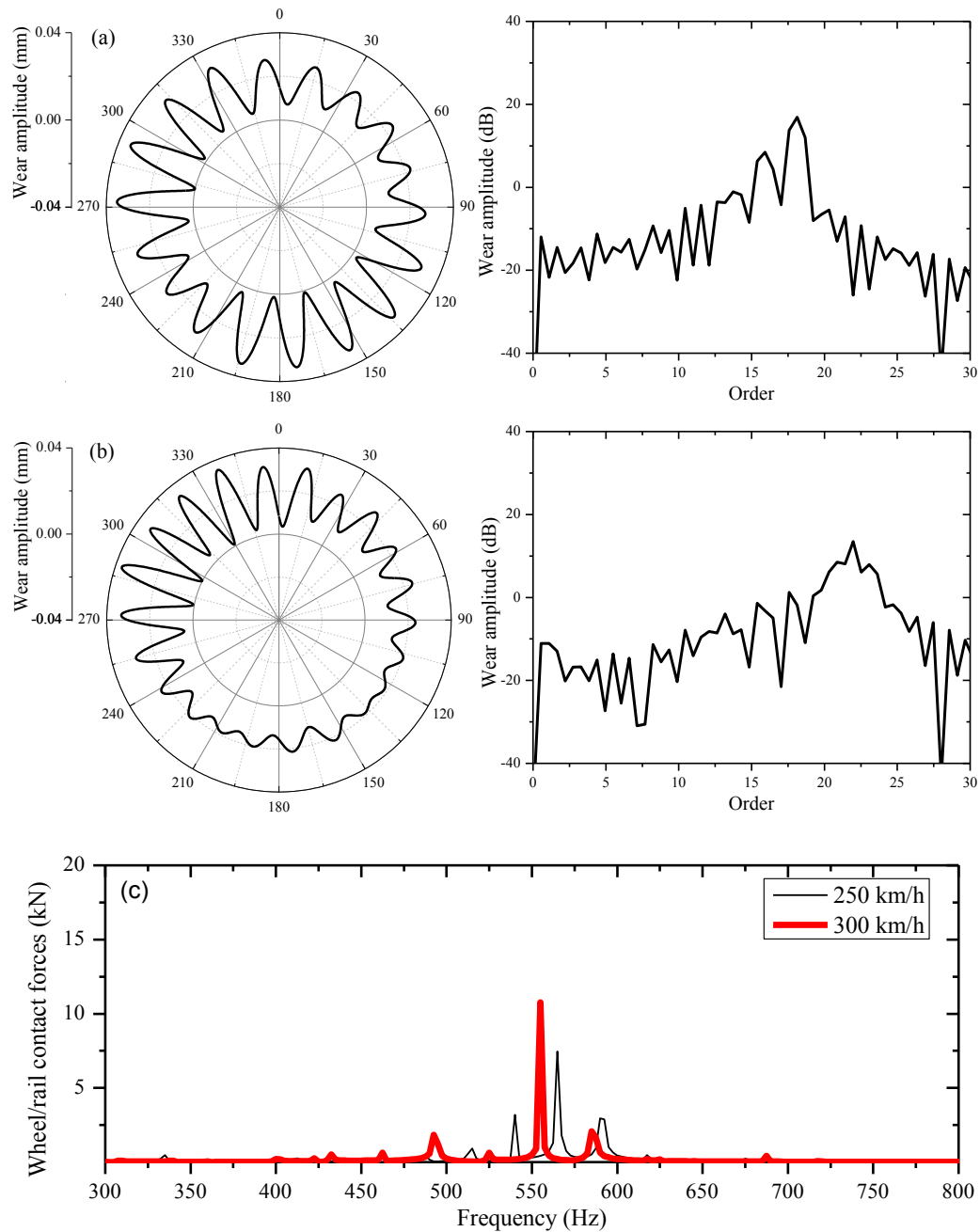
Figure 5.10: (a) Pattern and harmonic order distribution of wheel wear at 300 *km/h*; (b) pattern and harmonic order distribution of wheel wear at 250 *km/h*, and (c) frequency spectra of wheel/rail contact normal force at 250 and 300 *km/h*.

5.4.3.3 Wheelbase

The occurrence of primary peak in the frequency spectra of the wheel-rail contact forces in the vicinity of the bending mode frequency of the rail segment between the two wheelsets is the likely contributor to rapid growth in high-order wheel polygonalization. The bending mode frequency,

however, can be varied substantially by varying the wheelbase, as shown in Fig. 5.11. Fig. 5.11 (a) illustrates the frequency response characteristics of the peak normal contact force considering two different wheelbase values: 2.5 and 3 *m*. The frequency corresponding to the primary peak corresponding to the rail bending mode frequency, and it decreases from 650 *Hz* to near 530 *Hz*, when the wheelbase is increased from 2.5 to 3 *m*. Increasing the wheelbase, however, does not affect the coupled wheel-rail vertical deflection mode, occurring near 40 *Hz*. The reduction in the dominant frequency yields substantial reduction in the 18th-order wear magnitude, as seen in Fig. 5.11(b). Increasing the wheelbase, however, leads to dominant order of wheel wear near 14 due to lower rail bending mode frequency, while the wear magnitude is considerably smaller. The results confirm the correlation of the high-order wheel polygonalization with the localized rail bending mode frequency.
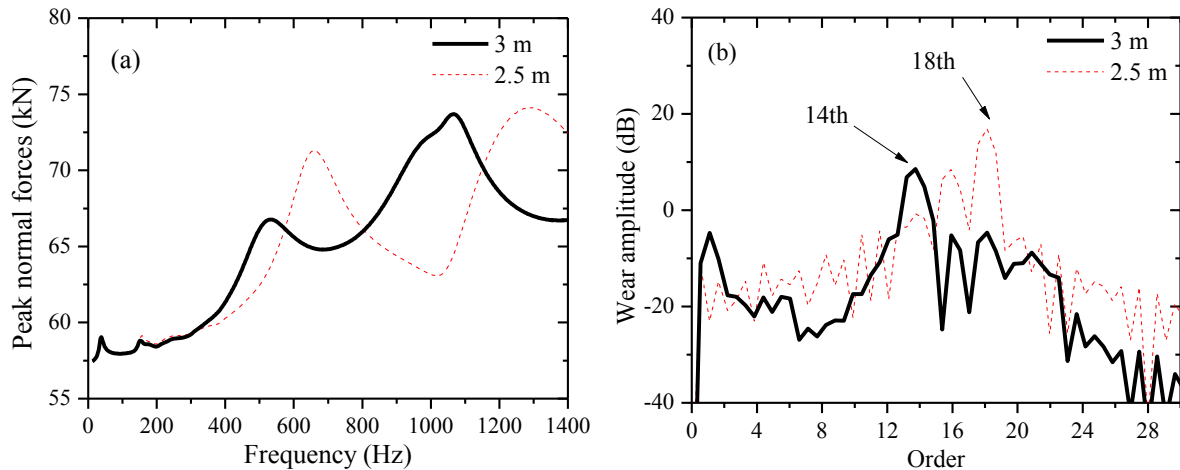
Figure 5.11: Effects of the wheelbase on: (a) frequency response characteristics of the peak wheel-rail normal force; and (b) magnitude and harmonic-order distribution of wheel wear.

5.4.3.4 Rail pad properties

The localized rail bending mode is also dependent on the elastic properties of the rail pad supports. Moreover, the peak wheel-rail contact force and the lateral creepage, and thereby the growth in high-order wheel polygonalization may be affected by visco-elastic properties of the rail pad. The effects of rail pad properties on the resulting responses are thus evaluated considering two different values of stiffness (20 and 120 *MN/m*) and viscous damping (30 and 130 *kNs/m*) constants. Figure 5.12(a) illustrates the effects of variations in stiffness constant of the rail pad on the frequency response characteristics of the wheel-rail normal force and lateral creepage. Increasing the rail pad support stiffness yields higher rail bending and coupled wheel-rail deflection mode frequencies.

The peak contact force and lateral creepage near the coupled wheel-rail deflection mode frequency, however, increase substantially with higher rail pad stiffness. It should be noted that the results are obtained considering nominal rail pad damping (30 *kNs/m*). The peak force and creepage in the vicinity of the rail bending mode frequency, however, decrease with increasing rail pad stiffness. Nearly negligible effect of rail pad stiffness is evident on the responses near the higher-order rail bending mode (≈1300 *Hz*).

Increasing the rail pad damping effectively suppresses the high frequency oscillations in the wheel-rail contact force and creepage, as seen in Fig. 5.12(b). Higher damping thus yields substantial reductions in peak magnitudes of the normal force and lateral creepage, especially at frequencies above 500 *Hz*. Higher damping, however, yields slightly higher normal force and creepage at frequencies below 500 *Hz*. The dynamic responses corresponding to the three half wavelength rail bending mode could thus be suppressed considerably by increasing the damping property of the rail pads.

The effects of rail pad stiffness and damping constants on the amplitude and harmonic order of cumulative wheel wear are illustrated in Fig. 5.13(a) and 5.13(b), respectively. The results show notably beneficial effects of damping on the growth of high-order wheel polygonalization. Increasing the damping yields substantial reductions in the magnitudes of high-order wheel wear, while it emphasizes the wear near the 1st and 8th harmonic orders. This is likely due to higher wheel-rail contact force and lateral creepage in the lower frequency range, as seen in Fig. 5.12(b). Increasing the rail pad stiffness also suppresses the 18th-order wear magnitude, while the magnitudes of lower order OOR increase substantially. Higher magnitudes of low-harmonic orders are attributable to high contact force and creepage in the vicinity of the coupled wheel/rail deflection mode, as seen in Fig. 5.12(a). Higher rail pad stiffness also yields relatively higher magnitudes of wear corresponding to harmonic orders exceeding 24. This is due to higher three half wavelength rail bending mode frequency. From the results, it may be deduced that relatively stiff rail pad supports would accelerate the formation of lower order wheel polygonalization, while the softer supports can lead to high-order wheel polygonalization. Increasing the support damping can substantially reduce the growth in high-order wheel polygonalization with only slight growth in the lower-order polygonalization.
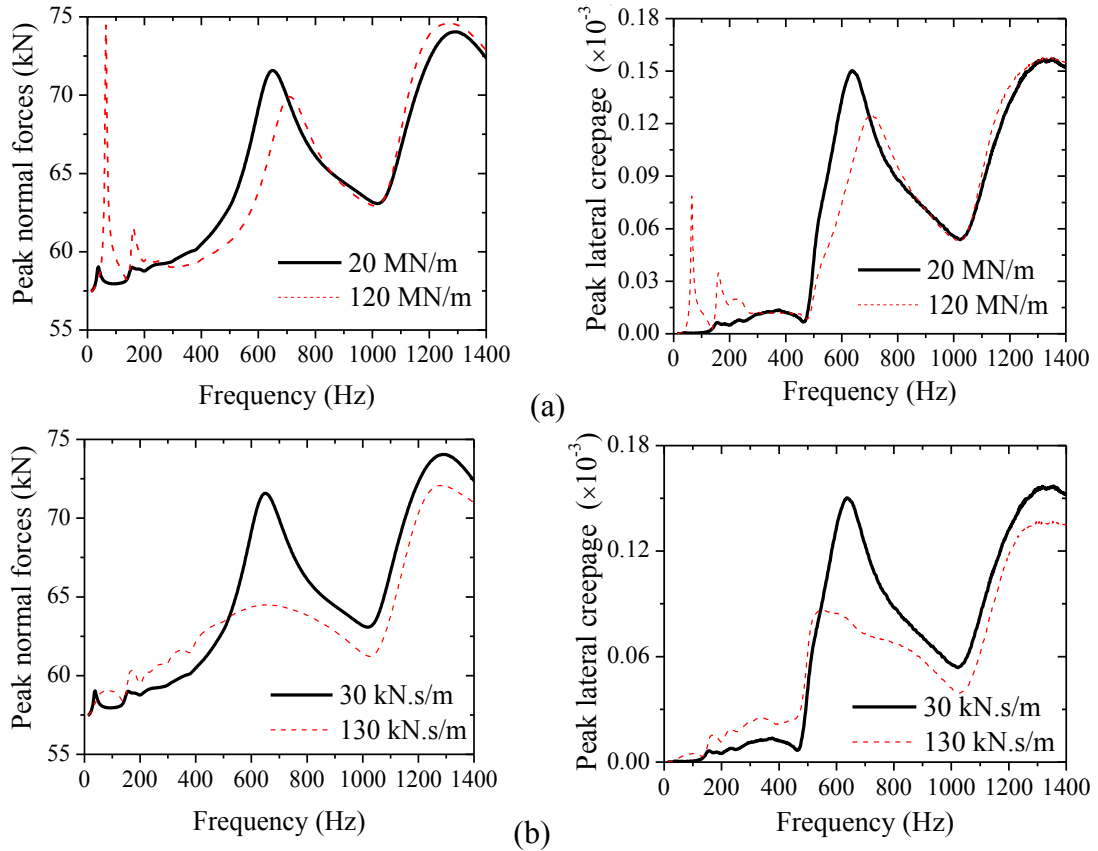
Figure 5.12: Effects of variations in rail pad properties on frequency response characteristics of peak wheel-rail contact force and lateral creepage: (a) rail pad stiffness; and (b) rail pad damping.
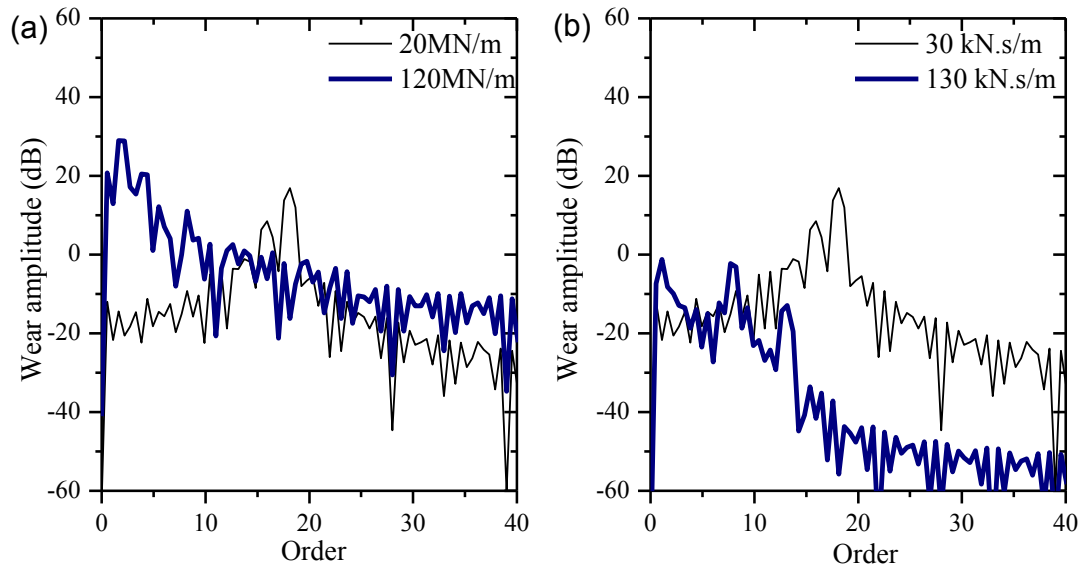
Figure 5. 13: Influence of rail pad stiffness and damping on the wheel wear magnitude and harmonic order: (a) rail pad stiffness; and (b) rail pad damping.

5.5 Conclusions

A long-term wear iterative scheme, integrating a coupled vehicle/track dynamic model and the Archard sliding wear model, was formulated to study the propagation of wheel polygonalization. The results show that wheel/rail interactions due to initial wheel irregularities accelerate the formation of high-order wheel polygonalization. A comprehensive wheel re-profiling process is thus vital for limiting the growth of high-order polygonal wear of the wheels. The evolution of wheel wear at forward speed of 300 *km/h* was observed to dominate around the 18th harmonic order, while this dominant order increased with reduction in the vehicle speed. The lower speed coupled with increased polygonal order resulted in comparable frequency of dominant wheel-rail contact force (wheel passing frequency), irrespective of the vehicle speed. This frequency (near 555 *Hz*) was observed to lie in the vicinity of the bending mode frequency of the rail segment between the two wheelsets. Furthermore, this frequency constituted a fixed-frequency excitation to the vehicle/track system and is believed as the primary contributor to the formation of high-order wheel polygonalization. The flexibility of the wheelset emphasized the wheel/rail lateral creepage in the lower frequency range, which could accelerate the formation of lower-order wheel polygonalization. The growth in higher-order wheel polygonalization, attributed to the local rail bending mode, could be limited by varying the rail bending mode frequency. It is shown that increasing the wheelbase and rail pad damping could significantly inhibit the growth in high-order wheel polygonalization. Opearions at varying forward speeds can help reduce the dominance of a particular harmonic order. Increasing the rail pad stiffness can enhance the low-frequency coupled wheel/rail vibration mode and lead to significantly higher wear of low harmonic orders. Increasing the rail pad damping is most beneficial in limiting the growth in high-order wheel polygonalization by reducing the magnitude of wheel-rail contact force and lateral creepage.

CHAPTER 6: CONCLUSIONS AND RECOMMENDATIONS

6.1 Major contributions and highlights of the dissertation research

This dissertation research presents systematic analytical and experimental studies on the high order polygonal wear of railway wheels and their effects on dynamic responses of the high-speed rail vehicle. A coupled vehicle/track dynamic model, considering the flexibility of the wheelset, the axle box, and the slab track, was formulated to study the effects of the discrete as well as continuous wheel defects on the wheel/rail contact forces, axle box acceleration, and dynamic stresses developed in the axle shaft. A long-term field test program on a high-speed rail vehicle was undertaken to characterize wheel surface irregularities and their evolution in addition to the axle box acceleration. The data were used to demonstrate the evolution of high order wheel polygonalization and its correlation with the axle box acceleration. A possible mechanism of formation of wheel polygonalization was further explored using a long-term wear iteration scheme by integrating the coupled vehicle/track dynamic model with the Archard sliding wear model. The major highlights/contributions of the dissertation research are summarized below:

- A comprehensive coupled vehicle/track dynamic model considering the flexibility of wheelset, axle box, and slab track was developed. The model permitted the effects of wheel-rail contact forces on deflections of the wheelset, track and the axle box. The model results showed important significance of the wheelset flexibility when compared to those obtained for the widely-used rigid wheelset models. Furthermore, the validity of the model was demonstrated on the basis of the available measured data.

- The coupled vehicle/track model was used to study the effects of high-order wheel polygonalization on dynamic responses of a high-speed railway car in terms of wheel/rail contact forces, axle box acceleration, dynamic stress developed in the axle shaft. On the basis of a review of studies reporting measured wheels' profiles, it was established that wheel wear in high speed operations may be characterized in terms of polygonal radial deviations with harmonic orders as high as 24. The effects of radial deviation and its harmonic order on the wheel-rail contact force and axle box acceleration are presented considering different operating speeds.

- A long-term field test program involving measurements of wheel surface irregularities and axle box acceleration was undertaken for an accurate characterization of polygonal wear of

the wheels. The study also provided essential data to quantify the growth rate of wheel polygonalization and its correlation with the service mileage and axle box acceleration. The results of the study established rapid growth of wheel polygonalization in high-speed operations.

- A long-term wear iteration scheme comprising the coupled vehicle/track dynamic model with flexible wheelset and track and the Archard sliding wear model was developed to study accumulation of wheel wear over the service period and evolution of high-order wheel polygonalization. The key contribution of this study is identification of a possible mechanism leading to growth in high-order wheel polygonalization, which further provided guidance towards mitigation of the growth rate.

6.2 Major conclusions

The major conclusions drawn from the analytical and experimental studies are summarized below:

- The bending mode of the axle shaft, and out-of-phase motions of the right- and left-side wheels contributed considerably to the dynamic wheel/rail interactions, the axle box acceleration, and the dynamic stress in the wheelset axle shaft.

- The wheelset flexibility contributed to slightly lower magnitudes of peak wheel/rail contact force compared to the rigid wheelsets, while the wheelset deformation modes resulted in substantially higher peak wheel/rail creepage, peak axle box acceleration and dynamic stress developed in the wheelset axle shaft.

- The high-order wheel polygonalization in high-speed operations resulted in high magnitudes of wheel-rail contact force in the high frequency range. These could lead to wheel-rail separation at relatively lower speeds in the vicinity of the coupled wheel/rail vertical mode frequency. The dynamic wheel-rail contact force caused by a defective wheel also contributed to higher contact forces of the adjacent wheels, which further resulted in rapid growth in polygonal wear of the adjacent wheels.

- The wheel/rail separation-induced impacts together with elastic deformations of the wheelset and the flexible slab track contributed to high magnitudes of high-frequency axle box acceleration and bending stress in the wheelset axle, which would adversely affect the service life of the wheelset.

- The wheel/rail contact forces considering different vehicle speeds and harmonic orders revealed dominant wheel-rail contact force in the vicinity of the wheel passing frequency of about 580 *Hz,* irrespective of the harmonic order of polygonal wear and the vehicle speed. This was further correlated to bending mode of the rail segment between the two wheelsets.

- From the analyses of data acquired from field measurements, it was shown that the wheel surface roughness could be characterized by a combination of the 1st and either 18th or 19th harmonic orders. The 18th order roughness magnitude increased considerably with the service mileage compared to those corresponding to the other harmonic orders.

- The analyses of wheel profiles following the re-profiling revealed OOR, which could be characterized by low-order harmonics, ranging from 1 to 5. Greater standard deviation of the roughness magnitude corresponding to the 1st harmonic order was observed, which was attributed to the re-profiling process.

- The measured axle box acceleration at the end of the first re-profiling cycle revealed dominant peaks near 540.2, 571.8 and 603.5 *Hz,* as well as the second and third multiples of the dominant frequencies. These dominant frequencies correspond to wheel roughness in the 17th to 19th harmonic orders, and bending mode of the rail. The acceleration response of the axle box decreased substantially after the wheel re-profiling.

- A very good correlation was observed between the peak *rms* acceleration of the axle box and peak roughness magnitude of the dominant harmonic order. This suggested that the axle box acceleration could serve as a good measure for detecting wheel polygonalization defect and thereby the wheel removal criterion.

- The "three half wavelength" rail bending vibration mode within the wheelbase (near 650 *Hz*) was identified as the primary contributor to high magnitude wheel/rail contact forces in the $500 \sim 700$ *Hz* frequency range, and the high order wheel polygonalization.

- The deformations of the flexible wheelset contributed to higher rate of the growth of wheel polygonalization of lower harmonic orders.

- Increasing the rail pad support stiffness intensified the wheel/rail coupled vibration leading to formation of lower order wheel polygonalization, while a higher rail pad damping effectively suppressed the high frequency components of the contact force and thereby the growth of high order wheel polygonalization.

- Eliminating the initial wheel irregularities and frequent variations in the operating speed could mitigate the formation of high-order wheel polygonalization.

6.3 Recommendations for future studies

The proposed vehicle/track dynamic model considering of flexibility of the wheelset, the axle box, and the slab track can serve as an effective tool for analyzing the dynamic responses of a rail vehicle due to wheel defects of discrete as well as continues nature. Moreover, the long-term wear iteration scheme proposed in the study could be employed to investigate the formation of wheel out-of-round (OOR) defects over the service periods. The models presented in the study, however, assumed linear properties of the primary and secondary suspensions, and the rail pad supports. These components are known to exhibit strongly nonlinear stiffness and damping characteristics, which may strong affect wheel-rail interactions, and the resulting dynamic responses and evolution of wheel/rail wear. Moreover, mitigation of wheel polygonalization involves further challenges considering tuning of the vehicle and track system parameters, suspension properties, and optimizing the train operating and maintenance routines. Particular topics of future work may include the following:

- Under the high magnitude and high-frequency loading condition at the wheel/rail interface, the nonlinearities in the rail pads and primary suspension (hydraulic damper, coil spring and rubber pad) may impose significant influences on the wheel/rail contact forces and dynamic responses of the vehicle and track system. Further efforts are thus needed in developments in reliable nonlinear component models and their integration to the vehicle model.

- The wheel polygonalization shows substantial influence on dynamic stress in the wheelset axle shaft, which may have adverse effect on the service life of the wheelset in the presence of a pre-existing defect such as a crack. Further efforts would thus be desirable to study the effects of high order wheel polygonalization on the fatigue lives of components in the presence of a pre-existing defect.

- The "three half wavelength" rail bending vibration mode has been identified as the primary causal factor leading to high order wheel polygonalization through the simulation of the proposed vehicle/track dynamic model and the long-term wear model. A long-term field or

laboratory study is needed to examine validity of the iterative wear prediction scheme and identification of more reliable wear model coefficients.

- The wear rate coefficient used in the Archard sliding wear model needs to be further refined to account for the effects of the wheel/rail work hardening on the wear rate. This could also provide importance guidance on scheduling of the wheel re-profiling cycles.

- Considering the important contributions of high-frequency deflections of the rail, damping materials for damping treatment of the track should be explored to suppress the high frequency wheel-rail contact force and creepage, and thereby mitigate the formation of high-order wheel polygonalization.

- High magnitude and high frequency impact loads induced by the wheel polygonalization may also pose significant influences on the railway bridge. The analytical and experimental investigations on the dynamic responses of bridge are thus suggested in the presence of wheel polygonalization.

REFERENCES

1   Nielsen, J. C., Johansson, A. (2000) Out-of-round railway wheels-a literature survey. Journal of Rail and Rapid Transit, 214(2), 79-91.

2   Wu, T. X., Thompson, D. J. (2004) The effects of track non-linearity on wheel/rail impact. Journal of Rail and Rapid Transit, 218(1), 1-15.

3   Thompson, D. J., Wu, T. X., Armstrong, T. (2003) Wheel/rail rolling noise-The effects of nonlinearities in the contact zone. Proceedings of the 10th International Congress on Sound and Vibration, Stockholm, Sweden, July 7-10, pp. 1-20.

4   Jergéus, J. (1998) Full-scale railway wheel flat experiments. Journal of Rail and Rapid Transit, 213(1), 1-13.

5   Kumagai, N., Ishikawa, H., Haga, K., Kigawa, T., Nagase, K. (1991) Factors of wheel flats occurrence and preventive measures. Wear, 144(1-2), 277-287.

6   Jergéus, J. (1998) Martensite formation and residual stresses around railway wheel flats. Journal of Mechanical Engineering Science, 212(1), 69-79.

7   Snyder, T., Stone, D. H., Kristan, J. (2003) Wheel flat and out-of round formation and growth. Proceedings of the 2003 IEEE/ASME Joint, Chicago, USA, April 22-24, pp. 143-148.

8   Stone, D. H., Moyar, G. J. (1989) Wheel shelling and spalling–an interpretive review. Rail Transportation, 5(1), 9-30.

9   Sun, J., Sawley, K. J., Stone, D. H., Teter, D. F. (1998) Progress in the reduction of wheel spalling. Proceedings of the 12th International Wheelset Congress. Qingdao, China, September, 21-25, pp. 18-29.

10   Makino, T., Yamamoto, M., Fujimura, T. (2002) Effect of material on spalling properties of railroad wheels. Wear, 253(1), 284-290.

11   Moyar, G. J., Stone, D. H. (1991) An analysis of the thermal contributions to railway wheel shelling. Wear, 144(1), 117-138.

12   Kumagai, N., Ishikawa, H., Haga, K., Kigawa, T., Nagase, K. (1991) Factors of wheel flats occurrence and preventive measures. Wear, 144(1), 277-287.

13   Kaper, H. P. (1988) Wheel corrugation on Netherlands railways (NS): Origin and effects of "polygonization" in particular. Journal of Sound and Vibration, 120(2), 267-274.

14   Vernersson, T. (1999) Thermally induced roughness of tread-braked railway wheels: Part 1: brake rig experiments. Wear, 236(1), 96-105.

15   Vernersson, T. (1999) Thermally induced roughness of tread braked railway wheels: Part 2: modelling and field measurements. Wear, 236(1), 106-116.

16   Nielsen, J.C.O., Lundén, R., Johansson, A., Vernersson, T. (2010) Train-track interaction and mechanisms of irregular wear on wheel and rail surfaces. Vehicle System Dynamics, 40(1-3), 3-54.

17   Barber, J. R. (1999) Thermoelasticity and contact. Journal of Thermal Stresses, 22(4), 513-525.

18   Barber, J.R., Ciavarella, M. (2000) Contact mechanics. International Journal of Solids and Structures, 37(1), 29-43.

19   Geijselaers, H. J., Koning, A. J. (2000) Finite element analysis of thermoelastic instability with intermittent contact. Journal of Tribology, 122(1), 42-46.

20   Pallgen, G. (1998) Unrunde Rader an Eisenbahnfahrzeugen. Eisenbahningenieur, 49 (1), 56-60.

21   Rode, W., Miiller, D., Vitman, J. (1997) Results of DB AG investigations "Out-of-Round Wheels". Proceedings of the Corrugation Symposium-Extended Abstracts, IFV Bahntechnik; Technische Universitäat Berlin, Germany.

22   Johansson, A. (2006) Out-of-round railway wheels-assessment of wheel tread irregularities in train traffic. Journal of Sound and Vibration, 293(3), 795-806.

23   Brommundt, E. (1997) A simple mechanism for the polygonalization of railway wheels by wear. Mechanics Research Communications, 24(4), 435-442.

24   Meinke, P., Meinke, S. (1999) Polygonalization of wheel treads caused by static and dynamic imbalances. Journal of Sound and Vibration, 227(5), 979-986.

25   Morys, B. (1998) Enlargement of out-of-round wheel profiles on high speed trains. Journal of Sound and Vibration, 227(5), 965-978.

26   Meywerk, M. (1999) Polygonalization of railway wheels. Archive of Applied Mechanics, 69(2), 105-120.

27   Johansson, A., Andersson, C. (2005) Out-of-round railway wheels-a study of wheel polygonalization through simulation of three-dimensional wheel-rail interaction and wear. Vehicle System Dynamics, 43(8), 539-559.

28   Luo, R., Zeng, J., Wu, P.B., Dai, H.Y. (2010) Simulation and analysis of wheel out-of-roundness wear of high-speed train. Journal of the China Railway Society, 32(5), 30-35.

29   Wu, X. W, Rakheja, S., Ahmed, A. K. W., Chi, M. R. (2017) Influence of a flexible wheelset on the dynamic responses of a high-speed railway car due to a wheel flat. Journal of Rail and Rapid Transit, DOI: 0954409717708895.

30   Jin. X. S., Wu, L., Fang, J., Ling, L. (2012) An investigation into the mechanism of the polygonal wear of metro train wheels and its effect on the dynamic behaviour of a wheel/rail system. Vehicle System Dynamics, 50(12), 1817-1834.

31   Chen, G.X., Jin, X. S., Wu, P.B., Dai, H.Y., Zhou, Z.R. (2011) Finite element study on the generation mechanism of polygonal wear of rail wheels. Journal of the China Railway Society, 33(1), 14-18.

32   Zhang, J., Han, G. X., Xiao, X. B., Wang, R. Q., Zhao, Y., Jin, X. S. (2014) Influence of wheel polygonal wear on interior noise of high-speed trains. Journal of Zhejiang University-SCIENCE A, 15(12), 1002-1018.

33   Wu, X.W., Chi, M.R., Wu, P.B. (2015) Influence of polygonal wear of railway wheels on the wheel set axle stress. Vehicle System Dynamics, 53(11), 1535-1554.

34   Wu, Y., Du, X., Zhang, H. J., Wen, Z. F., Jin, X. S. (2017) Experimental analysis of the mechanism of high-order polygonal wear of wheels of a high-speed train. Journal of Zhejiang University-SCIENCE A, 18(8), 579-592.

35   Hou, K., Kalousek, J., Dong, R. (2003) A dynamic model for an asymmetrical vehicle/track system. Journal of Sound and Vibration, 267(3), 591-604.

36   Dong, R. (1994) Vertical dynamics of railway vehicle-track system. Doctoral dissertation, Concordia University, Montreal, Canada.

37   Lyon, D. (1972) The calculation of track forces due to dipped rail joints, wheel flats and rail welds. ORE Colloquia: Report on the Second Colloquium "Technical Computer Programs", Derby, England, May.

38   Nielsen, J.C.O., Igeland, A. (1995) Vertical dynamic interaction between train and track influence of wheel and track imperfections. Journal of Sound and Vibration, 187(5), 825-839.

39   Newton, S. G., Clark, R.A. (1979) An investigation into the dynamic effects on the track of wheel flats on railway vehicles. Journal of Mechanical Engineering Science, 21(4), 287-297.

40   Dong, R.G., Sankar, S. (1994) A finite element model of railway track and its application to the wheel flat problem. Journal of Rail and Rapid Transit, 208, 61-72.

41   Bian, J., Gu, Y., Murray, M. H. (2013) A dynamic wheel-rail impact analysis of railway track under wheel flat by finite element analysis. Vehicle System Dynamics, 51(6), 784-797.

42   Dukkipati, R. V., Dong, R. (1999) Impact loads due to wheel flats and shells. Vehicle System Dynamics, 31(1), 1-22.

43   Sackfield, A., Dini, D., Hills, D. A. (2007) Contact of a rotating wheel with a flat. International Journal of Solids and Structures, 44(10), 3304-3316.

44   Johansson, A., Nielsen, J. C. (2003) Out-of-round railway wheels-wheel-rail contact forces and track response derived from field tests and numerical simulations. Journal of Rail and Rapid Transit, 217(2), 135-146.

45   Grassie, S. L., Gregory, R. W., Harrison, D., Johnson, K. L. (1982) The dynamic response of railway track to high frequency vertical excitation. Journal of Mechanical Engineering Science, 24(2), 77-90.

46   Dukkipati, R.V., Dong, R. (1999) Impact loads due to wheel flats and shells. Vehicle System Dynamics, 31(1), 1-22.

47   Zhai, W. M. (2001) Dynamic effects of vehicles on tracks in the case of raising train speeds. Journal of Rail and Rapid Transit, 215(2), 125-135.

48   Sun, Y. Q., Dhanasekar, M. (2002) A dynamic model for the vertical interaction of the rail track and wagon system. International Journal of Solids and Structures, 5(39), 1337-1359.

49   Fermér, M., Nielsen, J. (1995) Vertical interaction between train and track with soft and stiff railpads-full-scale experiments and theory. Journal of Rail and Rapid Transit, 209(1), 39-47.

50   Wu, T. X., Thompson, D. J. (2003) On the impact noise generation due to a wheel passing over rail joints. Journal of Sound and Vibration, 267(3), 485-496.

51   Wu, T. X., Thompson, D. J. (2002) A hybrid model for the noise generation due to railway wheel flats. Journal of Sound and Vibration, 251(1), 115-139.

52   Wu, T. X., Thompson, D. J. (2004) On the parametric excitation of the wheel/track system. Journal of Sound and Vibration, 278(4-5), 725-747.

53   Nielsen, J.C., Ekberg, A., Lundén, R. (2005) Influence of short-pitch wheel/rail corrugation on rolling contact fatigue of railway wheels. Journal of Rail and Rapid Transit, 219(3), 177-187.

54   Popp, K., Kaiser, I. and Kruse, H. (2003) System dynamics of railway vehicles and track. Archive of Applied Mechanics, 72(11-12), 949-961.

55   Baeza, L., Fayos, J., Roda, A., Insa, R. (2008) High frequency railway vehicle-track dynamics through flexible rotating wheelsets. Vehicle System Dynamics, 46(7), 647-659.

56   Baeza, L., Vila, P., Xie, G., Iwnicki, S.D. (2011) Prediction of rail corrugation using a rotating flexible wheelset coupled with a flexible track model and a non-Hertzian/non-steady contact model. Journal of Sound and Vibration, 330(18-19), 4493-4507.

57   Vila, P., Fayos, J., Baeza, L. (2011) Simulation of the evolution of rail corrugation using a rotating flexible wheelset model. Vehicle System Dynamics, 49(11), 1749-1769.

58   Torstensson, P. T., Nielsen, J. C., Baeza, L. (2011) Dynamic train-track interaction at high vehicle speeds-Modelling of wheelset dynamics and wheel rotation. Journal of Sound and Vibration, 330(22), 5309-5321.

59   Martínez-Casas, J., Di Gialleonardo, E., Bruni, S., Baeza, L. (2014) A comprehensive model of the railway wheelset–track interaction in curves. Journal of Sound and Vibration, 18(333), 4152-4169.

60   Fermér, M., Nielsen, J.C.O. (1994) Wheel/rail contact forces for flexible versus solid wheels due to tread irregularities. Vehicle System Dynamics, 23(S1), 142-157.

61   Barke, D. W., Chiu, W. K. (2005) A review of the effects of out-of-round wheels on track and vehicle components. Journal of Rail and Rapid Transit, 219(3), 151-175.

62   Wu, X., Chi, M., Gao, H. (2016) Damage tolerances of a railway axle in the presence of wheel polygonalizations. Engineering Failure Analysis, 66, 44-59.

63   Li, L., Xiao, X., Jin, X. (2011) Interaction of subway LIM vehicle with ballasted track in polygonal wheel wear development. Acta Mechanica Sinica, 27(2), 297-307.

64   Liu, X., Zhai, W. (2014) Analysis of vertical dynamic wheel/rail interaction caused by polygonal wheels on high-speed trains. Wear, 314(1), 282-290.

65   Zhang, J., Han, G. X., Xiao, X. B., Wang, R. Q., Zhao, Y., Jin, X. S. (2014) Influence of wheel polygonal wear on interior noise of high-speed trains. Journal of Zhejiang University Science A, 15(12), 1002-1018.

66   Wu, L., Zhong, S.Q., Jin, X. S., L, L. (2011) Influence of polygonal wheel on running safety of vehicle. Journal of Traffic and Transportation Engineering, 11(3), 47-54.

67   Wang, Y. J., Zeng, J., Luo, R., Gao, H. (2013) Effect of polygonal wheel on vehicle dynamic performance. Journal of Sichuan University (Engineering Science Edition), 45(3), 176-182.

68   Chen, W. (2011) Research on wheel polygonalization of High speed train. Master dissertation, Southwest Jiaotong University, Cheng Du.

69   Pan, R., Zhao, X., Liu, P., Ren, R. (2017) Micro-mechanism of polygonalization wear on railroad wheels. Wear, 393, 213-220.

70   UIC B169/DT 405: Schadkatalog Räder/Radsatzwellen/Radsätze, Teil 1: Einleitung, Terminologie, Klassierung der Fehler, Fehlerarten am Radsatz.

71   Song, C. Y., Shen, W. L., Li, X. F, Cui, L. T. (2016) Investigation on the effects of polygonal wheel on the vehicle system and the countermeasure strategies. Symposium on Improving Passenger Comfort, Changchun, China.

72   BS EN 15313:2010. Railway applications: In-service wheelset operation requirements. In-service and off-vehicle wheelset maintenance.

73   Zuo, J., Ren, L., Wu, M. (2010) Simulation and experimental research on anti-sliding control of railway vehicle braking. Journal of Tongji University. Natural Science, 38(6), 912-916.

74   Luo. R., Zeng. J. (2008) Anti-sliding control simulation of railway vehicle braking. Chinese Journal of Mechanical Engineering, 3, 007.

75   Zuo, J., Wu, M. (2010) Research on anti-sliding control of railway brake system based on adhesion-creep theory. Proceedings of International Conference on Mechatronics and Automation (ICMA), Xian, China, August 4-7, pp. 1690-1694.

76   Nielsen, J. C. O., Mirza, A., Cervello, S., Frid, A., Müller, R., Nelain, B., Ruest, P. (2010) Train induced ground vibration-Optimised rolling stock mitigation measures and their parameters. RIVAS, SCP0-GA-2010-265754.

77   Galvín, P., Romero, A., Domínguez, J. (2010) Vibrations induced by HST passage on ballast and non-ballast tracks. Soil Dynamics and Earthquake Engineering, 9(30), 862-873.

78   Galvín, P., Romero, A., Domínguez, J. (2010) Fully three-dimensional analysis of high-speed train–track–soil-structure dynamic interaction. Journal of Sound and Vibration, 24(329), 5147-5163.

79   Jenkins, H. H., Stephenson, J. E., Clayton, G. A., Morland, G. W., Lyon, D. (1974) The effect of track and vehicle parameters on wheel/rail vertical dynamic forces. Railway Engineering Journal, 3(1), 2-16.

80 Knothe, K., Grassie, S. L. (1993) Modelling of railway track and vehicle/track interaction at high frequencies. Vehicle System Dynamics, 22(3-4), 209-262.

81 Thompson, D. J. (1991) Theoretical modelling of wheel-rail noise generation. Journal of Rail and Rapid Transit, 205(2), 137149.

82 Knothe, K. L., Strzyzakowski, Z., Willner, K. (1994) Rail vibrations in the high frequency range. Journal of Sound and Vibration, 169(1), 111-123.

83 Fenander, A. (1997) Frequency dependent stiffness and damping of railpads. Journal of Rail and Rapid Transit, 211(1), 51-62.

84 Remennikov, A., Kaewunruen, S., Ikaunieks, K. (2006) Deterioration of dynamic rail pad characteristics. Proceedings of the Conference on Railway Engineering, Melbourne, Australia, May 1-3, pp. 174-179.

85 Ilias, H. (1999). The influence of railpad stiffness on wheelset/track interaction and corrugation growth. Journal of Sound and Vibration, 227(5), 935-948.

86 Xiao, X., Jin, X., Wen, Z., Zhu, M., Zhang, W. (2011).Effect of tangent track buckle on vehicle derailment. Multibody System Dynamics, 25(1), 1-41.

87 Ling, L., Xiao, X., Jin, X. (2013) Study on derailment mechanism and safety operation area of high-speed trains under earthquake. Journal of Computational and Nonlinear Dynamics, 7(4), 41001.

88 Xiao, X., Jin, X., Deng, Y., Zhou, Z. (2008) Effect of curved track support failure on vehicle derailment. Vehicle System Dynamics, 46(11), 1029-1059.

89 Rücker, W. (1982) Dynamic interaction of a railroad-bed with the subsoil. Soil dynamics & Earthquake Engineering conference, 2, 435-448.

90 Sato, Y., Odaka, T., Takai, H. (1988) Theoretical analyses on vibration of ballasted track. Railway Technical Research Institute, Quarterly Reports, 29(1), 30-32.

91 Zhai, W. M., Cai, C. B., Guo, S. Z. (1996) Coupling model of vertical and lateral vehicle/track interactions. Vehicle System Dynamics, 26(1), 61-79.

92 Zhai, W. M., Cai, Z. (1997) Dynamic interaction between a lumped mass vehicle and a discretely supported continuous rail track. Computers & Structures, 63(5), 987-997.

93 Esveld, C. (2003). Recent developments in slab track. European Railway Review, 9(2), 81-85.

94   Blanco-Lorenzo, J., Santamaria, J., Vadillo, E. G., Oyarzabal, O. (2011) Dynamic comparison of different types of slab track and ballasted track using a flexible track model. Journal of Rail and Rapid Transit, 225(6), 574-592.

95   Popp, K., Kruse, H., Kaiser, I. (1999) Vehicle-track dynamics in the mid-frequency range. Vehicle System Dynamics, 31(5-6), 423-464.

96   Grassie, S. L. (1996) Models of railway track and vehicle/track interaction at high frequencies: Results of benchmark test. Vehicle System Dynamics, 25(S1), 243-262.

97   Claus, H., Schiehlen, W. (1998) Modeling and simulation of railway bogie structural vibrations. Vehicle System Dynamics, 29(S1), 538-552.

98   Carlbom, P. F. (2001) Combining MBS with FEM for rail vehicle dynamics analysis. Multibody System Dynamics, 6(3), 291-300.

99   Stribersky, A., Moser, F., Rulka, W. (2002) Structural dynamics and ride comfort of a rail vehicle system. Advances in Engineering Software, 33(7-10), 541-552.

100   Dietz, S., Netter, H., Sachau, D. (1998) Fatigue life prediction of a railway bogie under dynamic loads through simulation. Vehicle System Dynamics, 29(6), 385-402.

101   Baeza, L., Vila, P., Xie, G., Iwnicki, S. D. (2011) Prediction of rail corrugation using a rotating flexible wheelset coupled with a flexible track model and a non-Hertzian/non-steady contact model. Journal of Sound and Vibration, 330(18-19), 4493-4507.

102   Baeza, L., Fayos, J., Roda, A., Insa, R. (2008) High frequency railway vehicle-track dynamics through flexible rotating wheelsets. Vehicle System Dynamics, 46(7), 647-659.

103   Lieh, J., Yin, J. (1998) Stability of a flexible wheelset for high speed rail vehicles with constant and varying parameters. Journal of Vibration and Acoustics, 120(4), 997-1002.

104   Vila, P., Fayos, J., Baeza, L. (2011) Simulation of the evolution of rail corrugation using a rotating flexible wheelset model. Vehicle System Dynamics, 49(11), 1749-1769.

105   Thomas, D. L., Wilson, J. M., Wilson, R. R. (1973) Timoshenko beam finite elements. Journal of Sound and Vibration, 31(3), 315-330.

106   Koro, K., Abe, K., Ishida, M., Suzuki, T. (2004) Timoshenko beam finite element for vehicle-track vibration analysis and its application to jointed railway track. Journal of Rail and Rapid Transit, 218(2), 159-172.

107   Dahlberg, T. (1995) Vertical dynamic train/track interaction- verifying a theoretical model by full-scale experiments. Vehicle System Dynamics, 24(S1), 45-57.

108   Jaschinski, A. (1995) Multibody simulation of flexible vehicles in interaction with flexible guideways. Vehicle System Dynamics, 24(S1), 31-44.

109   Chudzikiewicz, A. (2000) Simulation of rail vehicle dynamics in MATLAB environment. Vehicle System Dynamics, 33(2), 107-119.

110   Zhai, W., Sun, X. (1994) A detailed model for investigating vertical interaction between railway vehicle and track. Vehicle System Dynamics, 23(S1), 603-615.

111   Pearson, J. T., Goodall, R. M., Pratt, I. (1998) Control system studies of an active anti-roll bar tilt system for railway vehicles. Journal of Rail and Rapid Transit, 212(1), 43-60.

112   Baeza, L., Roda, A., Nielsen, J. C. O. (2006) Railway vehicle/track interaction analysis using a modal substructuring approach. Journal of Sound and Vibration, 293(1-2), 112-124.

113   Nielsen, J. C. O. (2008) High-frequency vertical wheel-rail contact forces-Validation of a prediction model by field testing. Wear, 265(9-10), 1465-1471.

114   Huang, C., Zeng, J., Liang, S. (2013) Carbody hunting investigation of a high speed passenger car. Journal of Mechanical Science and Technology, 27(8), 2283-2292.

115   Zeng, J., Wu, P. (2004) Stability analysis of high speed railway vehicles. JSME International Journal Series C Mechanical Systems, Machine Elements and Manufacturing, 47(2), 464-470.

116   Cheng, Y. C., Lee, S. Y., Chen, H. H. (2009) Modeling and nonlinear hunting stability analysis of high-speed railway vehicle moving on curved tracks. Journal of Sound and Vibration, 324(1), 139-160.

117   Lee, S. Y., Cheng, Y. C. (2003) Nonlinear hunting stability analysis of high-speed railway vehicles on curved tracks. International Journal of Heavy Vehicle Systems, 10(4), 344-361.

118   Kalker, J. J. (1979) Survey of wheel-rail rolling contact theory. Vehicle System Dynamics, 8(4), 317-358.

119   Kalker, J. J. (1991) Wheel-rail rolling contact theory. Wear, 144, 243-261.

120   Carter, F. W. (1926) On the action of a locomotive driving wheel. Proceedings of the Royal Society of London A: Mathematical, Physical and Engineering Sciences, 112(760), 151-157.

121   Wu, X., Chi, M. (2015) Parameters study of Hopf bifurcation in railway vehicle system. Journal of Computational and Nonlinear Dynamics, 10(3), 31012.

122   True, H. (1992) Railway vehicle chaos and asymmetric hunting. Vehicle System Dynamics, 20(S1), 625-637.

123   Vermeulen, P. J., Johnson, K. L. (1964) Contact of nonspherical elastic bodies transmitting tangential forces. Journal of Applied Mechanics, 31(2), 338-340.

124   Kalker, J. J. (1983) A simplified theory for non-Hertzian contact. Vehicle System Dynamics, 12(1-3), 43-45.

125   Simpack 9.7 help document. Available at http://www.simpack.com/.

126   Universal Mechanism 7.0 help document. Available at http://www.universalmechanism.com/.

127   ADAMS-Rail 2005 help document. Available at http://www.mscsoftware.com/.

128   NUCARS 2015 help document. Available at http://nucars.aar.com/.

129   Clark, R. A., Dean, P. A., Elkins, J. A., Newton, S. G. (1982) An investigation into the dynamic effects of railway vehicles running on corrugated rails. Journal of Mechanical Engineering Science, 24, 65-76.

130   Sato, Y. (1977) Study on high-frequency vibrations in track operated with high-speed trains. Railway Technical Research Institute, Quarterly Reports, 18, 109-114.

131   Baeza, L., Roda, A., Carballeira, J., Giner, E. (2006) Railway train-track dynamics for wheelflats with improved contact models. Nonlinear Dynamics, 45(3-4), 385-397.

132   Pieringer, A., Kropp, W., Nielsen, J. C. O. (2014) The influence of contact modelling on simulated wheel/rail interaction due to wheel flats. Wear, 314(1-2), 273-281.

133   Pieringer, A., Kropp, W., Thompson, D. J. (2011) Investigation of the dynamic contact filter effect in vertical wheel/rail interaction using a 2D and a 3D non-Hertzian contact model. Wear, 271(1-2), 328-338.

134   Zhu, J. J. (2006) Development of an adaptive contact model for analysis of wheel-rail impact load due to wheel flats. Master dissertation, Concordia University, Montreal, Canada.

135   Tunna, J., Sinclair, J., Perez, J. (2007) A review of wheel wear and rolling contact fatigue. Journal of Rail and Rapid Transit, 221(2), 271-289.

136   Bayer, R. G. (2002) Wear analysis for engineers. HNB Publishing, New York, USA, pp. 360.

137   Bolton, P.J., Clayton, P. (1984) Rolling-sliding wear damage in rail and tyre steels. Wear, 93(2), 145-165.

138   Lewis, R., Dwyer-Joyce, R.S., Olofsson, U., Hallam, R.I. (2004) Wheel material wear mechanisms and transitions. Proceedings of the 14th International Wheelset Congress, Orlando, FL, USA, October 17-21, pp.1-13.

139   Meng, H. C., Ludema, K. C. (1995) Wear models and predictive equations: their form and content. Wear, 181, 443-457.

140   Enblom, R., Berg, M. (2005) Emerging engineering models for wheel/rail wear simulation. Proceedings of the 8th International Conference Railway Engineering, London, June 29-30, 2005.

141   Johansson, A. (2005) Out-of-round railway wheels- Causes and consequences, Doctoral dissertation, Chalmers University of Technology, Sweden.

142   Sato, Y., Matsumoto, A., Knothe, K. (2002) Review on rail corrugation studies. Wear, 253(1), 130-139.

143   Jendel, T. (2002) Prediction of wheel profile wear-comparisons with field measurements. Wear, 253(1), 89-99.

144   Ding, J., Li, F., Huang, Y., Sun, S., Zhang, L. (2014) Application of the semi-Hertzian method to the prediction of wheel wear in heavy haul freight car. Wear, 314(1), 104-110.

145   Dirks, B., Enblom, R., Berg, M. (2016) Prediction of wheel profile wear and crack growth– comparisons with measurements. Wear, 366, 84-94.

146   Enblom, R., Berg, M. (2008) Impact of non-elliptic contact modelling in wheel wear simulation. Wear, 265(9), 1532-1541.

147   Ignesti, M., Malvezzi, M., Marini, L., Meli, E., Rindi, A. (2012) Development of a wear model for the prediction of wheel and rail profile evolution in railway systems. Wear, 284, 1-17.

148   Zobory, I. (1997) Prediction of wheel/rail profile wear. Vehicle System Dynamics, 28(2-3), 221-259.

149   Chongyi, C., Chengguo, W., Ying, J. (2010) Study on numerical method to predict wheel/rail profile evolution due to wear. Wear, 269(3), 167-173.

150   Hempelmann, K., Knothe, K. (1996) An extended linear model for the prediction of short pitch corrugation. Wear, 191(1), 161-169.

151   Neilsen, J. B. (1999) Evolution of rail corrugation predicted with a non-linear wear model. Journal of Sound and Vibration, 227(5), 915-933.

152   Andersson, C., Johansson, A. (2004) Prediction of rail corrugation generated by three-dimensional wheel-rail interaction. Wear, 257(3), 423-434.

153   Fermér, M., Nielsen, J.C.O. (1994) Wheel/rail contact forces for flexible versus solid wheels due to tread irregularities. Vehicle System Dynamics. 23(S1), 142-157.

154   Craig, R.R., Kurdila, A.J. (2006) Fundamentals of structural dynamics. John Wiley & Sons, New Jersey.

155   Arczewski, K., Frączek, J. (2005) Friction models and stress recovery methods in vehicle dynamics modelling. Multibody System Dynamics, 14(3-4), 205-224.

156   Timoshenko, S. (1926) Method of analysis of statical and dynamical stresses in rail. Proceeding of the International Congress of Applied Mechanics, Zurich, Switzerland, pp. 407-418.

157   Kalker, J.J. (1990) Three-dimensional elastic bodies in rolling contact. Springer Science & Business Media, Netherlands.

158   Uzzal R.U., Stiharu I., Ahmed W. (2009) Design and analysis of MEMS based accelerometer for automatic detection of railway wheel flat. World Academy of Science, Engineering and Technology, 53, 941-949.

159   Rao, S. S., Yap, F. F. (2011) Mechanical vibrations (Vol. 4). McGraw-Hill, New York.

160   Kalker, J. J. (1991) Wheel-rail rolling contact theory. Wear, 144(1-2), 243-261.

161   Wu, X., Cai, W., Chi, M., Wei, L., Shi, H., Zhu, M. (2015) Investigation of the effects of sleeper-passing impacts on the high-speed train. Vehicle System Dynamics, 53(12), 1902-1917.

162   Nielsen, J. C. (2008) High-frequency vertical wheel-rail contact forces-Validation of a prediction model by field testing. Wear, 265(9), 1465-1471.

163   Wu, T. X., Thompson, D. J. (2005) An investigation into rail corrugation due to micro-slip under multiple wheel/rail interactions. Wear, 258(7), 1115-1125.

164   Igeland, A. (1996) Railhead corrugation growth explained by dynamic interaction between track and bogie wheelsets. Journal of Rail and Rapid Transit, 210(1), 11-20.

165   Johansson, A., Nielsen, J. C. O. (2007) Rail corrugation growth-influence of powered wheelsets with wheel tread irregularities. Wear, 262(11), 1296-1307.

166 Jin, X. S., Wen, Z. F., Wang, K. Y., Zhou, Z. R., Liu, Q. Y., Li, C. H. (2006) Three-dimensional train-track model for study of rail corrugation. Journal of Sound and Vibration, 293(3), 830-855.

167 Gan, F., Dai, H., Gao, H., Chi, M. (2015) Wheel-rail wear progression of high speed train with type S1002CN wheel treads. Wear, 328, 569-581.

168 Quost, X., Sebes, M., Eddhahak, A., Ayasse, J. B., Chollet, H., Gautier, P. E., Thouverez, F. (2006) Assessment of a semi-Hertzian method for determination of wheel-rail contact patch. Vehicle System Dynamics, 44(10), 789-814.

169 Lundberg, G., Sjövall, H. (1958) Stress and deformation in elastic contacts. Chalmers University of technology, Sweden, p.58.

170 Polach, O. (2000) A fast wheel-rail forces calculation computer code. Vehicle System Dynamics, 33, 728-739.

171 Magel, E., Kalousek, J., Caldwell, R. (2005). A numerical simulation of wheel wear. Wear, 258(7), 1245-1254.

172 Wu, H., Cui, T., Huo, W. (2017) Experimental investigations on the wheel polygonalization. Proceedings of the 25th International Symposium on Dynamics of Vehicles on Roads and Tracks (IAVSD), Queensland, Australia, August 14-18.

173 Wu, X., Rakheja, S., Wu, H., Qu, S., Wu, P., Dai, H., Zeng, J., Ahmed, A.K.W. (2017) A study of polygonal wheel wear through a field test program. Vehicle Systems Dynamics (submitted).

174 Tao, G., Wang, L., Wen, Z., Guan, Q., Jin, X. (2016) Measurement and assessment of out-of-round electric locomotive wheels. Journal of Rail and Rapid Transit, DOI: 0954409716668210.